ESTIMATING DEEP PERCOLATION IN THE MOUNTAIN RAIN-SNOW TRANSITION ZONE

by

Patrick Richard Kormos

A dissertation

submitted in partial fulfillment

of the requirements for the degree of

Doctor of Philosophy in Geosciences

Boise State University

December 2013

BOISE STATE UNIVERSITY GRADUATE COLLEGE

DEFENSE COMMITTEE AND FINAL READING APPROVALS

of the dissertation submitted by

Patrick Richard Kormos

Dissertation Title: Estimating Deep Percolation in the Mountain Rain-Snow Transition Zone

Date of Final Oral Examination: 01 November 2013

The following individuals read and discussed the dissertation submitted by student Patrick Richard Kormos, and they evaluated his presentation and response to questions during the final oral examination. They found that the student passed the final oral examination.

James P. McNamara, Ph.D.	Chair, Supervisory Committee
Hans Peter Marshall, Ph.D.	Member, Supervisory Committee
Danny Marks, Ph.D.	Member, Supervisory Committee
Alejandro Flores, Ph.D.	Member, Supervisory Committee
Martyn P. Clark, Ph.D.	External Examiner

The final reading approval of the dissertation was granted by James P. McNamara, Ph.D., Chair of the Supervisory Committee. The dissertation was approved for the Graduate College by John R. Pelton, Ph.D., Dean of the Graduate College.

DEDICATION

This dissertation is dedicated to my wife, Sara Kormos, and my son, Alexander Kormos. Hopefully it will help provide Alex the opportunity to choose a life of fun and happiness, and allow his parents to retire early. Thanks for all of your support.

I also recognize that I'm Jim's first Ph.D. graduate. I hope that it was a fulfilling experience and we can continue to collaborate in the future. Thanks for all of your help.

I finally recognize my greater family, almost wholly on the other side of the Mississippi from us. Thanks for dealing with being away from Alex for so long.

ACKNOWLEDGEMENTS

I thank the students, faculty, and administration of the Department of Geosciences at Boise State University for supporting this work. I also acknowledge the Northwest Watershed Research Center for resources and support.

I specifically thank the following people who contributed to manuscripts and provided intellectual support: Mark Seyfried and Adam Winstral at the Northwest Watershed Research Center, Lucas Spaete at Boise Center Aerospace Laboratory, Justin Huntington at the Reno Desert Research Institute, Erik Boe and Pam Aishlin at (or formerly at) Boise State University, and Molly Gribb at the South Dakota School of Mines and Technology.

The Boise State University Student Research Initiative and Graduate College provided funding and travel support for this dissertation. NASA EPSCoR and INRA provided funding for this project. The collection and processing of the data presented in this paper were funded in part by NSF-CBET (0854553, 08522), USDA-ARS CRIS Snow and Hydrologic Processes in the Intermountain West (5362-13610-008-00D), USDA-NRCS Water and Climate Center-Portland, Oregon (5362-13610-008-03R), NSF-EPS (0919514), and NOAA (NA08NWS4620047). Any reference to specific equipment types or manufacturers is for information purposes and does not represent a product endorsement or recommendation. Boise State University and the USDA ARS are equal opportunity employers.

ABSTRACT

Deep percolation (DP) is estimated from a small study catchment in the semi arid rain-snow transition zone in the foothills north of Boise, ID. A water balance is performed at the catchment soil bedrock interface, where soil drainage is assumed to be partitioned into DP and streamflow. While stream flow is measured, soil drainage must be estimated. We model the snow dynamics and surface water inputs (SWI) to the soil (Chapter 3), and the soil dynamics and soil drainage to the soil-bedrock interface (Chapter 4). The high spatiotemporal dataset used in this modeling effort is presented for the 2011 water year, which includes weather, topographic, vegetation, and soils data (Chapter 1).

The image SNOw and mass BALance model is used to predict the distributed surface water inputs at a 2.5 m^2 resolution. Southwest facing slopes receive smaller and more frequent SWI from mid winter snowmelt, while the northeast slope receives more SWI during the spring. Rain on snow events produce similar SWI between slopes. Turbulent fluxes dominated the snowpack energetics in four of the five rain-on-snow events. Advective fluxes are greater than 17% during the 2 rain-on-snow events in December and January. Net radiation fluxes dominate spring melt events. Variations in the method used to distribute precipitation may result in large differences in total precipitation to the basin.

The Soil Ecohydraulic Model is used to predict soil drainage at 57 points across the catchment. Soils on the southwest facing slope drain more often throughout the water year, but the northeast facing slope contributes a greater total magnitude of soil drainage. Peaks in catchment soil drainage and deep percolation coincide with rain on snow events. Deep percolation is estimated to be 272 mm ± 34 mm for the 2011 water year, which is 29% ±4% of the precipitation.

In summary, we provide a high temporal and spatial data set from a catchment in the rain snow transition zone in Chapter 2. This dataset provides a) soil, vegetation, and weather data to parameterize and drive hydrologic models, and b) snow and hydrologic response data to validate hydrologic models. The data is used to run a physically based snow accumulation and melt model, from which we obtain a high spatial and temporal resolution data set of surface water inputs to the catchment in Chapter 3. Chapter 4 estimates deep percolation from the catchment using the surface water input time series from Chapter 3.

TABLE OF CONTENTS

LIST OF TABLES

LIST OF FIGURES

LIST OF ABBREVIATIONS

ET	Evapotranspiration
DCEW	Dry Creek Experimental Watershed
DP	Deep Percolation
Dr	soil Drainage
iSNOBAL	*i*mage SNOw and mass BALance model
Q	stream discharge
ΔQ	sum of energy balance terms (Chapter 3)
ROS	Rain On Snow
SEM	Soil Ecohydraulic Model
SWI	Surface Water Input
TL	Treeline Experimental Catchment

CHAPTER ONE: INTRODUCTION

Deep percolation (DP) from mountain catchments, defined as water that leaves the catchment boundaries through subsurface drainage, can be an important component of the catchment water balance (Flerchinger and Cooley, 2000; Bayard *et al.*, 2005; Graham *et al.*, 2010; Kelleners *et al.*, 2010; Makurira *et al.*, 2010; Selle *et al.*, 2011; Han *et al.*, 2012), and an important source of mountain block recharge (Aishlin and McNamara, 2011; Hogan *et al.*, 2004; Thoma *et al.*, 2011). For example, the Great Basin Region receives most of the groundwater recharge from mountainous divides between basins (Hevesi *et al.*, 2003; Flint *et al.*, 2004; Scanlon *et al.*, 2006). The estimation of this flux is therefore a necessary step in performing catchment mass balance studies or ground water recharge studies where deep percolation is significant. This study quantifies DP from the climatically sensitive rain snow transition zone through a coupled field and modeling approach.

Numerous studies have estimated DP from various environments using a variety of methods. DP has been measured directly from small areas from caves (Taucer *et al.*, 2008; Sheffer *et al.*, 2011). However, it is extremely difficult to measure whole catchment DP directly because of the diffuse and often inaccessible location of occurrence. Practical methods of quantifying DP (*see* Sammis *et al.*, 1982) are therefore limited to detailed mass balance studies of water or conservative solutes (Graham *et al.*, 2010), numerical modeling at a lower soil boundary (Kelleners *et al.*, 2009; Guan *et al.*,

2010; Kelleners *et al.*, 2010; Dijksma *et al.*, 2011; Wang *et al.*, 2011), or storage-discharge relationships (e.g Brutsaert and Nieber, 1977; Kirchner, 2009; Ajami *et al.*, 2011). Solute balance approaches require multiple years of data to overcome inherent assumptions, and even then may only be correct when averaging over the period of record (Wood, 1999; Aishlin and McNamara, 2011). Physically based hydrologic modeling of DP is hindered by a general lack of knowledge of the transmissive properties of underlying bedrock, which makes model parameterization challenging. The application of storage-discharge methods assumes that streamflow incorporates all drainage from catchment storage, which is not valid in "leaky" catchments where streamflow does not represent all drainage.

Few studies attempt to account for the complex water inputs associated with the rain-snow transition zone, and few attempts have been made to describe the timing of DP events. The rain snow transition is an important area for research because the phase of precipitation and the snowpack itself are susceptible to climate warming effects. Winter precipitation here falls when the dew point temperature is close to zero. Precipitation is snow when the dewpoint temperature is below zero and is rain when it is above zero. Also, the snowpack is relatively thin and has an internal temperature close to zero for the majority of the winter season. These two characteristics lead to it having a low thermal mass. Warming air temperatures are therefore capable of producing significant snowmelt.

This study presents a mass balance approach at the soil-bedrock interface to estimate DP from the rain snow transition zone. This simple conceptual model assumes

that soil drainage (Dr) that reaches the soil-bedrock interface is either routed laterally to the stream (Q), or routed vertically to DP:

$$DP = Dr - Q \, .$$

If Q is measured at a catchment outlet, calculating DP is a matter of estimating Dr. The difficulties in directly measuring Dr are similar to measuring DP. We therefore follow a storage-centric modeling approach described by Seyfried et al. (2009) to estimate Dr. In doing so, we rely on the basic principle that if storage dynamics are modeled accurately, fluxes will likewise be accurate (McNamara et al., 2011). This approach requires estimates of surface water inputs (SWI), or the water entering the soil surface, evapotranspiration (ET), and drainage from individual soil layers. We apply this storage-centric modeling approach to the Treeline Experimental Catchment (TL) in the semi-arid foothills north of Boise, ID. DP is expected to occur in semi-arid environments where shallow soils overlie fractured bedrock, and/or the timing of SWI to a basin are offset from the evaporative demand (Seyfried *et al.*, 2005).

Two distinguishing geographic characteristics of TL are: 1) it is located on the Idaho Batholith, and 2) it is located in the rain snow transition zone. The Idaho Batholith is a fractured biotite granodiorite intrusion, which has weathered to form a shallow sandy soil. The catchment soil characteristics allow us to distribute a relatively simple, capacitance-based soil model across the watershed to estimate ET and drainage from individual soil layers. The benefit to using a model of this type is the relatively low data demands.

The catchment location within the rain snow transition zone leads to a complex spatiotemporal pattern of SWI to the catchment, ultimately leading to the aforementioned

offset between SWI and evaporative demand. The complicated precipitation and snow dynamics associated with this zone requires the use of a fully distributed physically-based snow accumulation and melt model to obtain catchment SWI. Models of this sort have the benefit of being able to estimate the spatial distribution of the snow accumulation and melt at fine spatial and temporal resolutions. These models also come with large data requirement.

TL has an extensive network of measurement locations, which produce an abundance of weather and hydrologic response data. The data collected at TL is adequate for the modeling design proposed in this dissertation. In addition to permanent measurement locations, a series of snow surveys were performed during this study for enhanced model validation.

This dissertation consists of three articles, each a necessary step in estimating DP from semi-arid regions in the rain-snow transition zone. The first paper publishes the 2011 water year data used in modeling work performed at TL. It describes the data, processing and gap filling techniques, and the data availability. The data consists of time series vectors of weather, soil moisture, snow depth, and streamflow data. It also contains soil texture, soil depth, vegetation height, and snow data from 10 surveys. This data is freely available to anyone and is expected to be useful to anyone who is developing hydrological models, studying soil storage dynamic, or testing streamflow initiation hypothesis.

The second paper describes the spatial and temporal distribution of SWI to catchments in the rain snow transition zone. This paper applies the iSNOBAL model to TL and accounts for wind redistribution of snow as well as topography influences on the

distribution of radiation. This paper is an important advancement in the understanding of the complex snow dynamics that take place in the rain snow transition zone. The fine spatial and temporal resolution of the snowpack and SWI distributions will have an impact on the global energy balance, soil nutrient cycling, and water resource management studies.

The third paper estimates DP from TL using SWI from the second paper. This paper quantifies the annual magnitude and uncertainty of DP from TL. We also qualitatively describe the timing of DP and the relative importance of rain on snow events and spring melt events. We expect this paper to be influential in local and regional water resource studies as well as soil water dynamics studies.

In summary, we estimate that DP from TL is 272 mm ± 42 mm. This DP estimate is a result of careful modeling methods that focus on catchment storage. Chapter 2 presents a data set that includes weather, soil, vegetation, snow, and hydrologic response, which can be used to parameterize, drive, and validate hydrologic models. This data is used to obtain distributed SWI time series from a physically based snow accumulation and melt model in Chapter 3. Chapter 4 estimates whole catchment DP by utilizing the SWI time series from Chapter 3.

References

Aishlin P, McNamara J. 2011. Bedrock infiltration and mountain block recharge accounting using chloride mass balance. Hydrological Processes, 25: 1934-1948. DOI: DOI 10.1002/hyp.7950.

Ajami H, Troch PA, Maddock T, Meixner T, Eastoe C. 2011. Quantifying mountain block recharge by means of catchment-scale storage-discharge relationships. Water Resources Research, 47. DOI: W04504 10.1029/2010wr009598.

Bayard D, Stahli M, Parriaux A, Fluhler H. 2005. The influence of seasonally frozen soil on the snowmelt runoff at two Alpine sites in southern Switzerland. Journal of Hydrology, 309: 66-84. DOI: 10.1016/j.jhydrol.2004.11.012.

Brutsaert W, Nieber JL. 1977. Regionalized drought flow hydrographs from a mature glaciated plateau. Water Resources Research, 13: 637-644. DOI: 10.1029/WR013i003p00637.

Dijksma R, Brooks ES, Boll J. 2011. Groundwater recharge in Pleistocene sediments overlying basalt aquifers in the Palouse Basin, USA: modeling of distributed recharge potential and identification of water pathways. Hydrogeology Journal, 19: 489-500. DOI: 10.1007/s10040-010-0695-9.

Flerchinger GN, Cooley KR. 2000. A ten-year water balance of a mountainous semi-arid watershed. Journal of Hydrology, 237: 86-99. DOI: 10.1016/s0022-1694(00)00299-7.

Flint AL, Flint LE, Hevesi JA, Blainey JB. 2004. Fundamental concepts of recharge in the Desert Southwest: a regional modeling perspective. In: Groundwater Recharge in a Desert Environment: The Southwestern United States, Hogan JF, Phillips FM, Scanlon BR (eds.) AGU, pp: 159-184.

Graham C, van Verseveld W, Barnard H, McDonnell J. 2010. Estimating the deep seepage component of the hillslope and catchment water balance within a measurement uncertainty framework. Hydrological Processes, 24: 3631-3647. DOI: 10.1002/hyp.7788|10.1002/hyp.7788.

Guan H, Simunek J, Newman BD, Wilson JL. 2010. Modelling investigation of water partitioning at a semiarid ponderosa pine hillslope. Hydrological Processes, 24: 1095-1105. DOI: 10.1002/hyp.7571.

Han SM, Yang YH, Fan T, Xiao DP, Moiwo JP. 2012. Precipitation-runoff processes in Shimen hillslope micro-catchment of Taihang Mountain, north China. Hydrological Processes, 26: 1332-1341. DOI: 10.1002/hyp.8233.

Hevesi JA, Flint AL, Flint LE. 2003. Simulation of net infiltration and potential recharge using a distributed-parameter watershed model of thedeath valley region, Nevada and California. In: Water-Resources Investigations Report, US Geological Survey, pp: 171.

Hogan JF, Phillips FM, Scanlon BR. 2004. Preface to Groundwater Recharge in a Desert Environment: The Southwestern United States. In: Groundwater Recharge in a Desert Environment: The Southwestern United States, Hogan JF, Phillips FM, Scanlon BR (eds.) American Geophysical Union, pp: vii.

Kelleners TJ, Chandler DG, McNamara JP, Gribb MM, Seyfried MS. 2009. Modeling the Water and Energy Balance of Vegetated Areas with Snow Accumulation. Vadose Zone Journal, 8: 1013-1030. DOI: 10.2136/vzj2008.0183.

Kelleners TJ, Chandler DG, McNamara JP, Gribb MM, Seyfried MS. 2010. Modeling Runoff Generation on in a Small Snow-Dominated Mountainous Catchment. Vadose Zone Journal, 9: 517-527. DOI: 10.2136/vzj2009.0033.

Kirchner JW. 2009. Catchments as simple dynamical systems: Catchment characterization, rainfall-runoff modeling, and doing hydrology backward. Water Resources Research, 45. DOI: W02429 10.1029/2008wr006912.

Makurira H, Savenije HHG, Uhlenbrook S. 2010. Modelling field scale water partitioning using on-site observations in sub-Saharan rainfed agriculture. Hydrology and Earth System Sciences, 14: 627-638.

McNamara JP, Tetzlaff D, Bishop K, Soulsby C, Seyfried M, Peters NE, Aulenbach BT, Hooper R. 2011. Storage as a Metric of Catchment Comparison. Hydrological Processes: n/a-n/a. DOI: 10.1002/hyp.8113.

Sammis TW, Evans DD, Warrick AW. 1982. Comparison of methods to estimate deep-percolation rates. Water Resources Bulletin, 18: 465-470.

Scanlon BR, Keese KE, Flint AL, Flint LE, Gaye CB, Edmunds WM, Simmers I. 2006. Global synthesis of groundwater recharge in semiarid and arid regions. Hydrological Processes, 20: 3335-3370. DOI: 10.1002/hyp.6335.

Selle B, Minasny B, Bethune M, Thayalakumaran T, Chandra S. 2011. Applicability of Richards' equation models to predict deep percolation under surface irrigation. Geoderma, 160: 569-578. DOI: 10.1016/j.geoderma.2010.11.005.

Seyfried MS, Grant LE, Marks D, Winstral A, McNamara J. 2009. Simulated soil water storage effects on streamflow generation in a mountainous snowmelt environment, Idaho, USA. Hydrological Processes, 23: 858-873. DOI: 10.1002/hyp.7211.

Seyfried MS, Schwinning S, Walvoord MA, Pockman WT, Newman BD, Jackson RB, Phillips EM. 2005. Ecohydrological control of deep drainage in arid and semiarid regions. Ecology, 86: 277-287. DOI: 10.1890/03-0568.

Sheffer NA, Cohen M, Morin E, Grodek T, Gimburg A, Magal E, Gvirtzman H, Nied M, Isele D, Frumkin A. 2011. Integrated cave drip monitoring for epikarst recharge estimation in a dry Mediterranean area, Sif Cave, Israel. Hydrological Processes, 25: 2837-2845. DOI: 10.1002/hyp.8046.

Taucer PI, Munster CL, Wilcox BP, Owens MK, Mohanty BP. 2008. Large-scale rainfall simulation experiments on juniper rangelands. Transactions of the Asabe, 51: 1951-1961.

Thoma MJ, McNamara JP, Gribb MM, Benner SG. 2011. Seasonal recharge components in an urban/agricultural mountain front aquifer system using noble gas thermometry. Journal of Hydrology, 409: 118-127. DOI: 10.1016/j.jhydrol.2011.08.003.

Wang L, Wei SP, Horton R, Shao MA. 2011. Effects of vegetation and slope aspect on water budget in the hill and gully region of the Loess Plateau of China. Catena, 87: 90-100. DOI: 10.1016/j.catena.2011.05.010.

Wood WW. 1999. Use and misuse of the chloride-mass balance method in estimating ground water recharge. Ground Water, 37: 2-3. DOI: 10.1111/j.1745-6584.1999.tb00949.x.

CHAPTER TWO: SOIL, SNOW, WEATHER, AND SUB-SURFACE STORAGE DATA FROM A MOUNTAIN CATCHMENT IN THE RAIN-SNOW TRANSITION ZONE

Authors

Patrick R. Kormos[1]

Danny Marks[2]

James P. McNamara[1]

C.J. Williams[2]

H.P. Marshall[1]

Pam Aishlin[1]

David G. Chandler[3]

1. Boise State University, Department of Geosciences, 1910 University Dr., Boise, ID 83725
2. Agricultural Research Service, Northwest Watershed Research Center, 800 Park Blvd., Plaza IV, Suite 105 Boise, ID 83712
3. Syracuse University, L.C. Smith College of Engineering and Computer Science, 151 Link Hall, 900 South Crouse Ave., Syracuse, NY 13244

Abstract

A comprehensive hydroclimatic data set is presented for the 2011 water year to improve understanding of hydrologic processes in the rain-snow transition zone. This type of dataset is extremely rare in scientific literature because of the quality and quantity of soil depth, soil texture, soil moisture, and soil temperature data. Standard meteorological and snow cover data for the entire 2011 water year are included, which include several rain-on-snow events. Surface soil textures and soil depths from 57 points are presented as well as soil texture profiles from 14 points. Meteorological data include continuous hourly shielded, unshielded, and wind corrected precipitation, wind speed, air temperature, relative humidity, dew point temperature, and incoming solar and thermal radiation data. Sub-surface data included are hourly soil moisture data from multiple depths from 7 soil profiles within the catchment, and soil temperatures from multiple depths from 2 soil profiles. Hydrologic response data include hourly stream discharge from the catchment outlet weir, continuous snow depths from one location, intermittent snow depths from 5 locations, and snow depth and density data from ten weekly snow surveys. Though it represents only a single water year, the presentation of both above and below ground hydrologic condition makes it one of the most detailed and complete hydro-climatic datasets from the climatically sensitive rain-snow transition zone for a wide range of modeling and descriptive studies.

Introduction

Detailed weather, soils, and hydrologic response data are presented that provide a whole-catchment view of the dynamic hydrology that occurs in the mountain rain-snow transition zone. The rain-snow transition zone is the elevation band in temperate

mountains where winter precipitation is predominately rain below and snow above this zone. Rain or snow can fall anywhere within this zone. Precipitation can transition between phases during storms, but the snowline exists within the rain-snow transition zone. It may approach sea level at high latitudes [*Feiccabrino et al.*, 2012], but can frequently extend above 2000 m at lower latitudes [*Cayan et al.*, 2001]. In the interior Pacific Northwestern US, where this data collection effort was conducted, the rain-snow transition typically occurs in mid-elevations ranging from 1500 – 1800 m [*Nayak et al.*, 2010]. Nolin and Daly [2006] estimated that currently the rain-snow transition zone covers approximately 9200 km^2 in the Pacific Northwest. This is a region where warming trends are expected to shift the current precipitation regime toward being rain-dominated and move the rain-snow transition to higher elevations.

The mountain rain-snow transition zone is an important area for study because it is sensitive to warming trend effects on the snow cover [*Mote*, 2003] and ecosystems [*Cayan et al.*, 2001; *Cuo et al.* 2011]. The snow cover in this zone is sensitive to climate warming trends because it is generally warm and ephemeral. The presence or absence of snow impacts the energy and mass balance because it dictates whether incoming solar radiation is reflected or absorbed. Since precipitation can be deposited as either rain that is rapidly transmitted to the soil, or snow that delays the delivery of liquid water to the soil, changes in the precipitation phase translate directly to changes in the timing of water inputs to catchment soils. Weather and soil data sets have been published from rain-dominated [*Western and Grayson*, 1998] and snow-dominated areas [*Morin et al.*, 2012; *Reba et al.*, 2012; *Seyfried et al.*, 2001a; *Seyfried et al.*, 2001b], but there is a general lack of data from the rain-snow transition zone.

Seven significant ROS events, which are known to create large amounts of runoff from the combined volume of rain and rapid melt, were recorded in the data presented in this paper. These events often contribute to record floods [*Harr*, 1986; *Kattelmann*, 1996; *Marks et al.*, 1998; *McCabe et al.*, 2007; *Sui and Koehler*, 2001; *Surfleet and Tullos*, 2013] and can cause major avalanche cycles [e.g., *Conway and Raymond*, 1993]. One of the ROS events presented here caused the peak measured stream discharge (1998 – 2013) for this study catchment. ROS events in this region are common, but having them occur over a specific site under optimal measurement conditions is a matter of timing and luck. For example, Marks *et al*. [2013] established a transect of measurement sites every 50 m across 380 m of elevation (1488 – 1868 m) to monitor the transition between rain and snow. Though there were many precipitation occurrences, only a few significant mixed phase events were directly measured during the ten years that the transect was operated (2004 – 2013).

Catchment data are presented for the Treeline (TL) experimental catchment for the 2011 water year (WY2011: Oct. 1, 2010 – Sept. 30, 2011) (Figure 2.1). The study area is unique because it is located at both a climatic transition between rain and snow, and a vegetation transition between shrub lands and forests. The catchment is instrumented specifically to quantify the distribution of precipitation, snow cover, and soil moisture. Table 2.1 summarizes the hydro-meteorological parameters presented and Figure 2.1 locates catchment instrumentation. Table 2.2 summarizes the distributed watershed data presented. The dataset provides a high-resolution, fine-scale set of observations that offer a broad spectrum of researchers an opportunity to study a host of topics associated with water storage and flux in a small catchment. Model developers

can use distributed soil and topographic data to obtain state variables, weather data to drive, and snow, soil moisture, and streamflow data to evaluate the model performance. Detailed topographic data combined with soil moisture measurements can be used to evaluate topographic indices common to many empirical streamflow modeling approaches. Soil moisture redistribution algorithms that account for diffuse and preferential flow can be tested to evaluate the timing of soil moisture responses at depths. Traditional watershed hydrology methods, such as annual water balances and Budyko curves, can be used to make generalizations on geographic regions and watershed classifications.

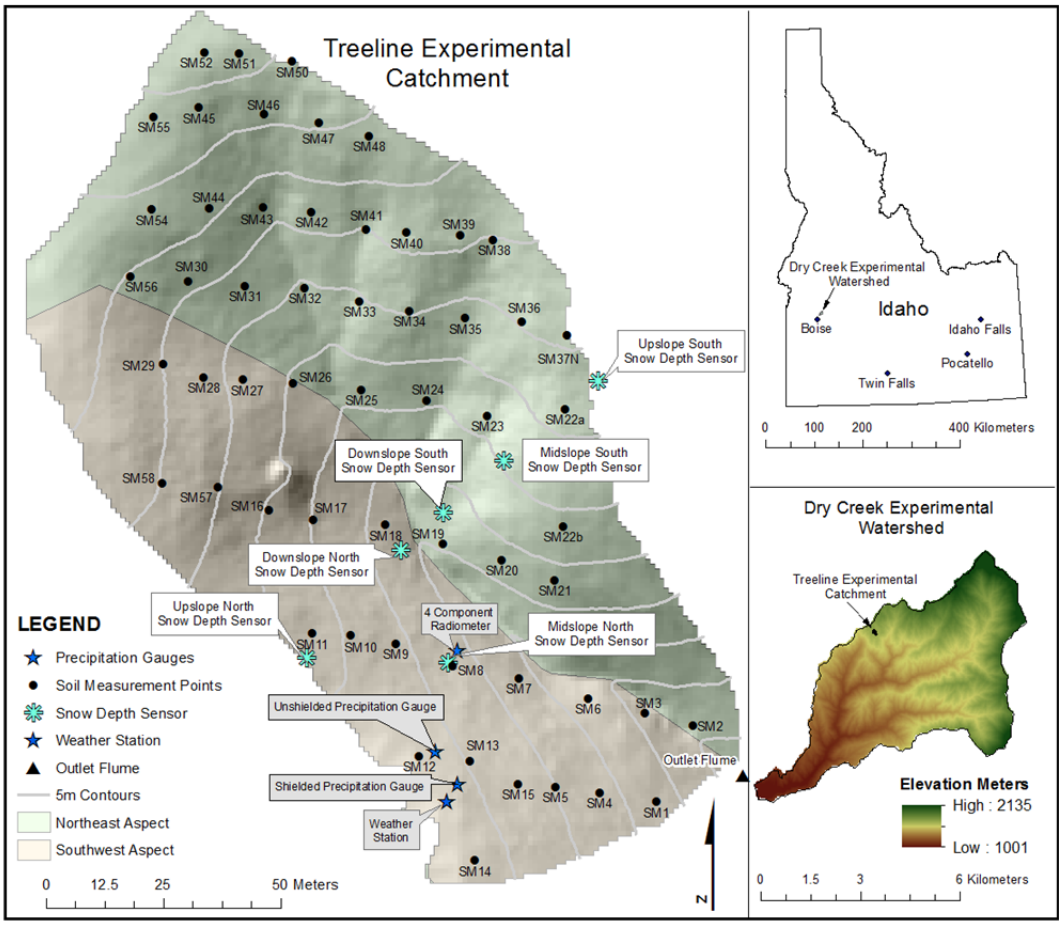

Figure 2.1 Location map of the Treeline experimental catchment in the Dry Creek

Table 2.1 Hydro-meteorological parameters, type of instruments, and instrument heights from the Treeline experimental catchment in WY2011. Locations are denoted by WS – weather station, 4CR – four component radiometer, Npit3 – north soil pit 3, OF – outlet flume.

hydro-meteorological parameter	method / instrument	sensor height (m)
shielded precipitation (WS)	8 inch Belfort-type gauge with Alter Shield	2
unshielded precipitation (WS)	8 inch Belfort-type gauge	2
wind corrected precipitation	(Hanson, 2004)	2
wind speed (WS)	Met One WS 013	2
wind direction (WS)	Met One WD 023	2
air temperature (WS)	Vaisala HMP45AC	2
Humidity (WS)	Vaisala HMP45AC	2
incoming solar (WS)	Matrix Mk 1-G	2
incoming & outgoing solar (4CR)	Hukseflux NR01	2
incoming & outgoing thermal (4CR)	Hukseflux NR01	2
soil temperature (Npit3)	CS 107 thermistor	-0.05
stream discharge (OF)	Druck PDCR1830 in v-notch flume	na

Table 2.2 Distributed watershed data, number of sensors, type of instruments, and instrument heights from the Treeline experimental catchment for WY2011.

number	variable	measurement method	heights (m)
2 profiles	soil temperature	CS 107 thermistor	-0.05 to -1.00
2 profiles	soil moisture	CS 615 soil moisture probe	-0.05 to -1.00
5 profiles	soil moisture	CS TDR100 soil moisture probe	-0.09 to -1.01
1 sensor	snow depth	Judd depth sensor	2
5 sensors	snow depth	MaxBotix XL-MaxSonar EZ2 (self-made)	2
10 surveys	snow depth	various	na
10 surveys	snow density	various	na
57 points	soil depth	steel rod pounded to refusal	-0.24 to -1.25
57 points	soil texture	sieve and hydromoter	0.00 to -0.30
14 profiles	soil texture	sieve and hydromoter	0.00 to -0.81

Catchment Description

TL is a 1.5 hectare catchment of the Dry Creek Experimental Watershed (DCEW) established in 1999 to study hydrologic processes in semiarid mountains. The extent of TL is defined by the location of a v-notch weir where catchment streamflow is measured (Figure 2.1). The elevation ranges from 1600 to 1645 masl and the mean slope is 21 degrees. Vegetation is typical of a transition between lower elevation grasslands and higher elevation forests, with steep slopes and stark differences between aspects shrubs, prunus ssp., forbs, and grasses with a mean canopy height of 0.7 m. Southwest facing slopes have similar but sparser vegetation with a mean height of 0.3 m. There are 8 mature conifer trees in the catchment. Soils are thin (20 – 125 cm), range from loam to sandy-loam, and overlie fractured granitic bedrock [*Gribb et al.*, 2009; *Yenko*, 2003, Miller et al., 2008]. Basins with ephemeral streams such as TL are important sources of groundwater recharge [Aishlin and McNamara, 2011]. Several studies have shown aspect differences on soil properties [*Geroy et al.*, 2011; *Smith et al.*, 2011; *Tesfa et al.*, 2009].

Weather Data

Weather data represent typical hydrological model forcing data, and include precipitation, solar and thermal radiation, air temperature and humidity, wind speed and direction, and soil temperature. Weather data are hourly and serially complete for the entire WY2011. Data gaps have been filled using the most appropriate of either linear interpolation, or linear regression to nearby measurements of the same variable.

Precipitation

Shielded and unshielded precipitation were measured at TL using Belfort-type gauges [Hanson, et al., 2001], filtered following Nayak et al. [2008], and wind corrected using the protocol of Hanson et al. [2004]. Precipitation and the stream hydrograph from the outlet weir are shown in Figure 2.2a. The phase of cumulative wind-corrected precipitation based on dew point temperatures is shown in Figure 2.2b [Marks et al. 2013].

Incoming Radiation

Solar radiation was measured by two pyranometers at the TL weather station. A continuous hourly data record was generated using data from the two instruments, but favoring the more recently calibrated Huxeflux NR01 (Table 2.1). Incoming thermal radiation was measured by the four-component radiometer. Gaps in the measured thermal radiation record were substantial (48%) and were filled using data from a pyrgeometer at 1720 masl 3.8 km away within DCEW. Figure 2.3a presents the water year time-series of incoming solar and thermal irradiance.

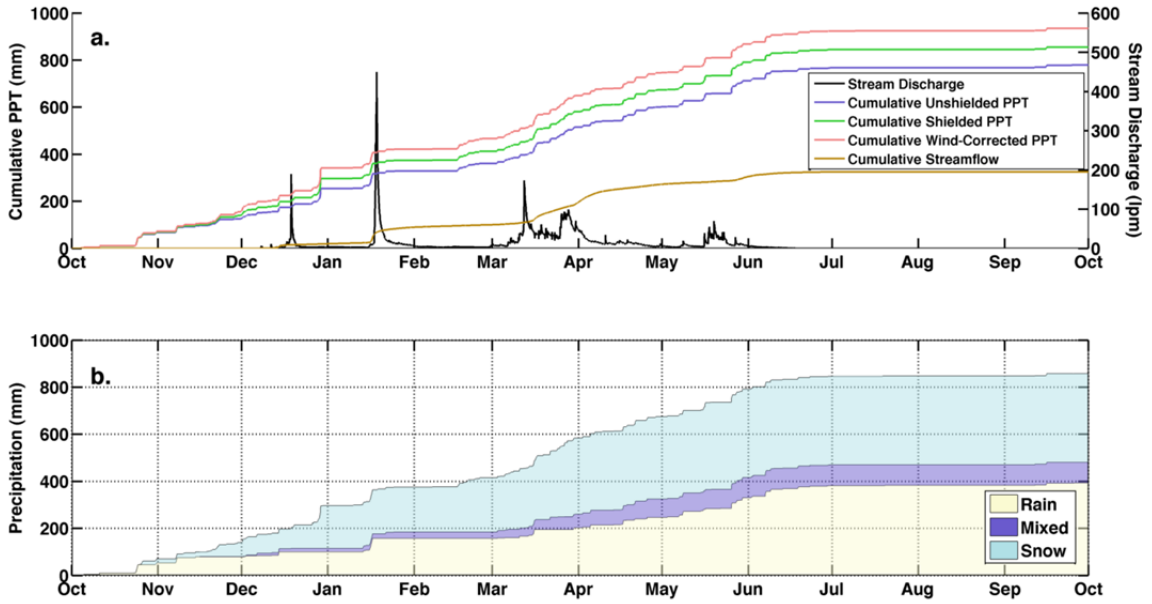

Figure 2.2 Precipitation and streamflow from the Treeline experimental catchment for WY2011. Cumulative shielded, unshielded, and wind-corrected precipitation with cumulative streamflow and the hydrograph (a). The phase of cumulative wind-corrected precipitation is based on dew point temperature (b).

Air Temperature and Humidity

Air temperature (T_a) and relative humidity (RH) were measured at the TL weather station. T_a and RH were converted to dew point temperature (T_d) using methods developed by Marks et al. [1999], as applied and described by Reba et al. [2011]. Figure 2.3b presents weekly minimum, maximum, and mean T_a and T_d for WY2011, which was a cooler year than average. The mean T_a was 7.9°C compared to the period of record mean, which was 9.3°C. The maximum T_a of 31.8°C was reached in late August while the minimum air T_a of -18.1°C was reached in late November. WY2011 was wetter than average with a mean T_d of -1.67°C compared to the period of record mean of -2.24°C. The maximum T_d of 14.1°C was reached in July, while the minimum T_d of -23.8°C was reached in November. The dew point temperature was close to zero for much of the

winter, demonstrating the sensitivity of the precipitation phase at this study location to changes in humidity and temperature.

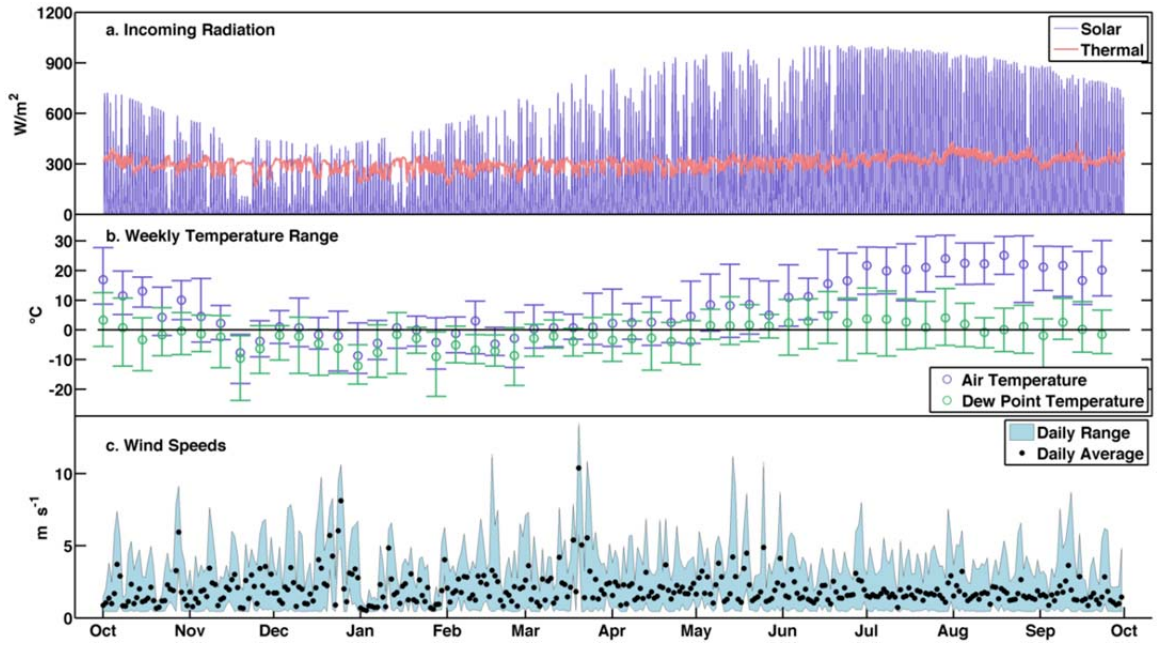

Figure 2.3 Meteorological forcings measured at the Treeline experimental catchment for WY2011 including incoming measured and gap-filled solar and thermal radiation (a), weekly average, minimum, and maximum air and dew point temperatures (b), and measured daily average, minimum, and maximum wind speeds (c).

Wind Speed and Direction

Wind speed (u) and direction (v) were measured at the TL weather station. Hourly u and v data are serially complete for WY2011. u ranges from 0 to 13.5 m s^{-1}. Figure 2.3c presents daily u_{max}, u_{min}, and u_{avg} for WY2011. Wind speeds for WY2011 do not show a pronounced difference between storm and non-storm time periods. Both have median values of approximately 1.5 m s^{-1}. Storm v is typically out of the southwest and

ranges from 175° to 250° during winter storms, which agrees with work in nearby areas [Winstral *et al*., 2013].

Soil Temperature

Soil temperature profiles are measured at all profile depths from Pit_3 and Pit_4 (Figure 2.1, Table 2.3). Figure 2.4 present mean daily soil temperature profile data from Pit_3 and mean daily snow depth.

Table 2.3 Soil profile names, aspects, and sensor depths

Profile Name	Aspect	Sensor Depths (cm)
Pit_3	E	5, 15, 60, 100
Pit_4	E	5, 15, 30, 45, 65
SD5	E	15, 101
SU5	E	9, 27
SU10	E	15, 52
SU20	E	12, 34
SU30	E	18, 70

Spatial Characterization Data

Characterization data are used to define the structure, composition, land cover, soil structure and hydrologic properties of the TL catchment. These data provide the fine-scale detail required for modeling and hydrologic assessment.

Soil Data

Soil depth and soil texture from the top 30 cm were obtained at 57 points across TL, representing the full range of exposures, slopes, and elevations in the catchment. Soil depths were measured by pounding a steel rod to refusal and soil texture was acquired by sieving core samples (mean sample size of 4.7 g) as described by Williams *et al*. [2009]. In addition, soil texture data from several depths at 14 locations are presented. Soil moisture data is presented that is collocated with texture profiles at locations SD5, SU5, SU10, SU20, and SU30 as described in the hydrologic response section of this paper.

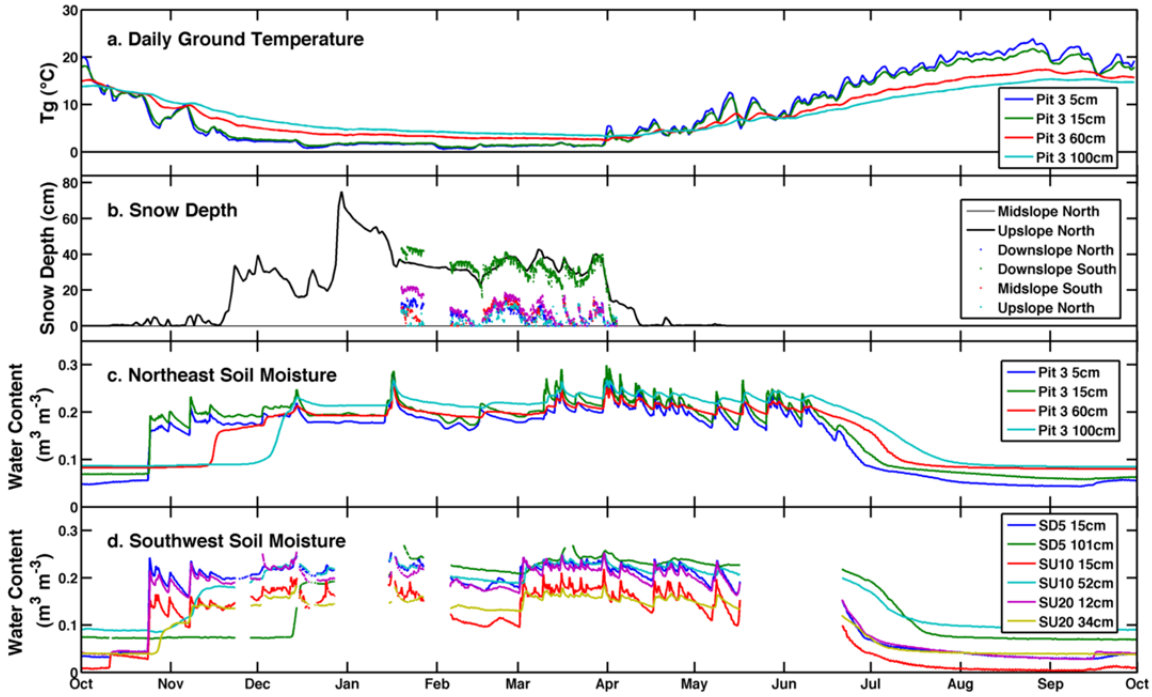

Figure 2.4 Soil and snow data from the Treeline experimental catchment for WY2011. Daily average soil temperature (a.) and moisture (c.) from pit 3 on the northeast facing slope, and soil moisture from several pits from the southwest facing slope (d.) are presented. Snow depths from six locations are presented in 2.4b.

GIS Data

Terrain elevation and structure are derived from an aerial LiDAR dataset acquired in 2009 and processed using Idaho State University's publicly available LiDAR processing tools (http://bcal.geology.isu.edu/tools/lidar) as described in Streutker and Glen [2006]. The processed TL GIS data includes four components: 1) a 2.5 m bare earth digital elevation model (DEM), from which 2) the catchment boundary is derived, GIS layers of 3) vegetation height, and 4) instrument and soil measurement locations. Figure 2.5 presents a shaded relief image of the TL catchment, with overlying vegetation height.

Snow and Hydrologic Response Data

Snow Depth

Hourly snow depth was recorded by a depth sensor located midslope on the northeast facing slope (Figure 2.1). These data were processed and cleaned, and are serially complete for WY2011. Figure 2.4b presents mean daily values for these data. Five additional ultrasonic snow depth sensors are located in a transect that covers the two dominant basin aspects (Figure 2.1). Due to instrument malfunctions, only intermittent snow depth data from these 5 sensors are available from January 19, 2011 through melt-out (Figure 2.4b).

Snow Survey Data

A series of ten weekly snow surveys was completed from January 21 to March 24, 2011. Surveys were designed to capture snow depth and snow water equivalent differences within the catchment [Winstral and Marks, 2013] based on LiDAR derived depth similarity classes [Shallcross, 2012]. Between five and nine snow density samples

were collected across the two predominant aspects on each survey day and were used to convert snow depth to SWE. Density measurements were taken with a federal-type tube, density cutter, or new snow tube depending on conditions [*Conger and McClung*, 2009; *Judson and Doesken*, 2000]. Density measurements are depth-integrated values and vary greatly on days where new snow is deposited on both bare ground and on the preexisting snowpack. A minimum of 105 depths were recorded in five transects each week, and the use of a Magnaprobe (SnowHydro, www.snowhydro.com) for seven out of the ten surveys enabled the collection of an average of 250 depths. Table 2.4 presents the number and method of measurements for each survey. Snow depth is presented as gridded average data (Figure 2.6). Gridded data also include the number of depth measurements and standard deviation at each grid cell.

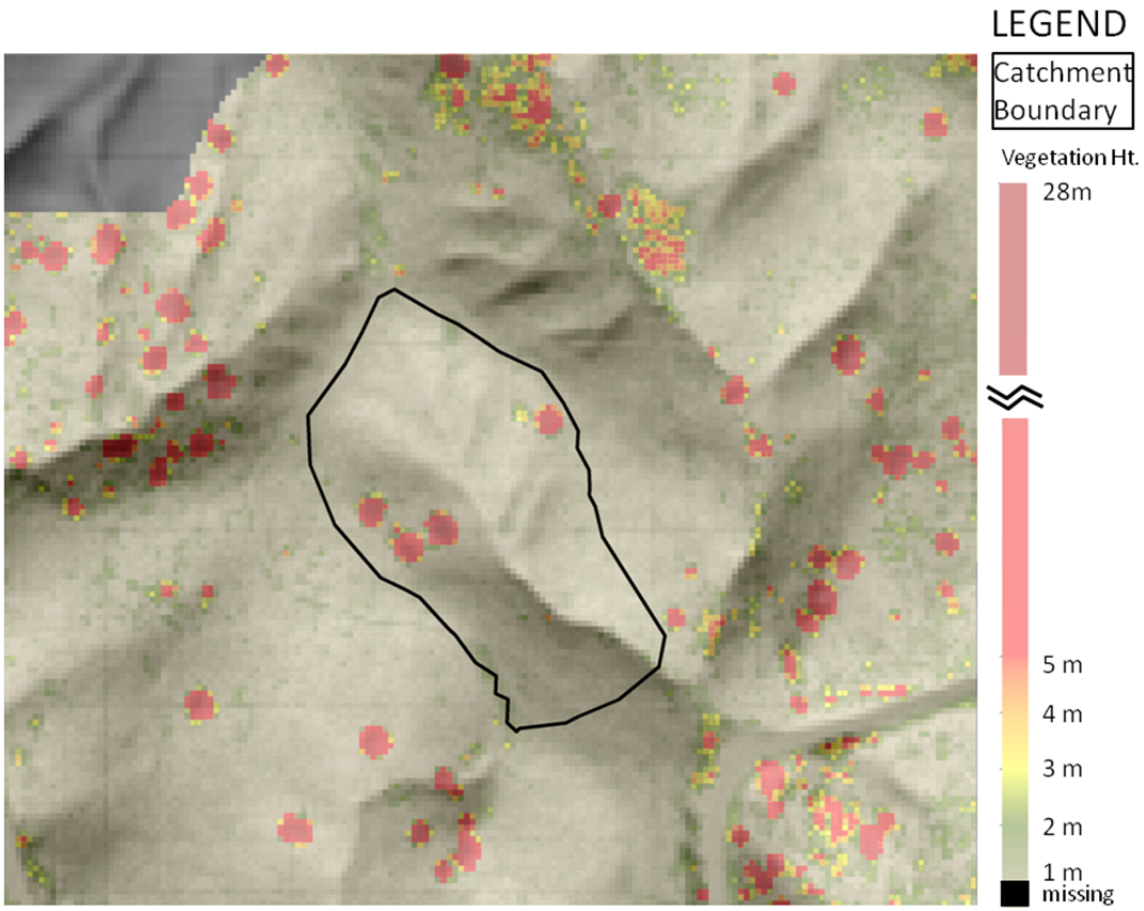

Figure 2.5 Aerial LiDAR-derived vegetation height over shaded topographic relief map.

Table 2.4 Summary of snow survey data including the date, number, and method of snow depth and density measurements.

survey date	number of snow depth measurements	depth measurement method	number of snow density measurements	density measurement method
1/21/2011	108	manual probe	7	federal tube
1/28/2011	248	magnaprobe	9	federal tube
2/4/2011	262	magnaprobe	9	federal tube / new snow tube
2/11/2011	395	magnaprobe	9	density cutter / new snow tube
2/18/2011	377	magnaprobe	9	density cutter
2/25/2011	155	magnaprobe	9	federal tube
3/4/2011	349	magnaprobe	7	federal tube
3/11/2011	105	manual probe	8	federal tube / density cutter
3/17/2011	300	magnaprobe	6	federal tube
3/24/2011	245	magnaprobe	5	federal tube

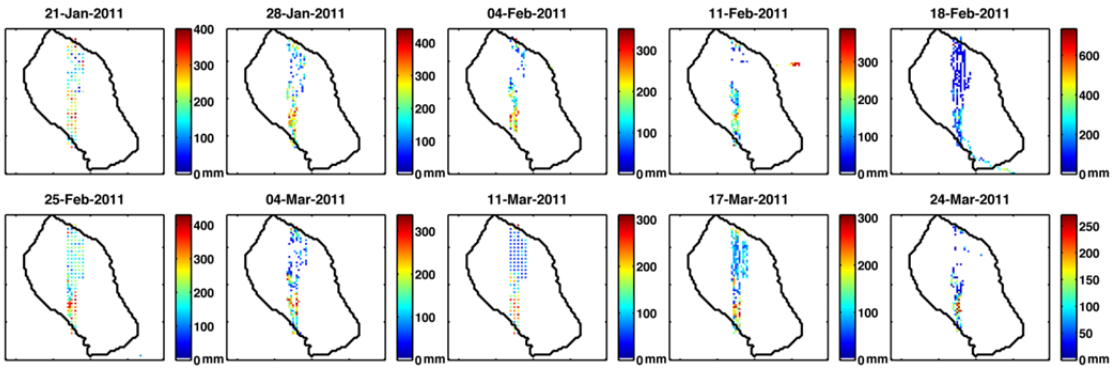

Figure 2.6 Gridded mean snow depth from 10 snow surveys.

Stream Discharge

Stream discharge is derived from stage recorded with a pressure transducer in a V-notch weir at the catchment outlet. The stream that drains TL is intermittent and initiates in the fall when snow cover is established and dries out in early to mid summer. Due to equipment malfunctions, continuous stage measurements begin on December 16th and continue through the cessation of streamflow. Discharge was estimated for the period prior to December 16 from a series of manual measurements and by developing a relationship between stage at the TL weir and data from other nearby weirs within DCEW over the ten years of record. The average WY2011 stream discharge at the TL weir is 9.3 liters per minute. The streamflow peak of record was caused by a ROS event on January 16th, 2011, which resulted in a high flow of 449.3 liters per minute. Figure 2.2a presents streamflow from the TL catchment.

Soil Moisture

Soil moisture is recorded at 2 depths at 5 southwest facing soil moisture profiles and at 4 and 5 depths at 2 northeast facing soil pits (Figure 2.1, Table 2.3). TL soil moisture dynamics is described by McNamara *et al*. [2005]. The coarse texture of TL soils leads to relatively rapid drainage when field capacity is exceeded. The semi-arid plant community draws soil moisture down quickly during spring green-up, but is slowed by spring rain events. Data from Pit_3 and Pit_4 are hourly and serially complete. Figures 2.4c and 2.4d present soil moisture data from Pit_3 on the northeast facing slope and profiles SD5, SU10, and SU20 on the southwest facing slope. Shallow probes may be influenced by evaporation from the soil surface. Deepest sensors at all profiles were placed at the soil bedrock interface, and may measure soil moisture increased due to the

collection of water at the soil-bedrock interface, or the influence of lateral flow from upslope contributing areas.

Data Availability

All data presented in this paper are available from the PANGAEA® website (http://doi.pangaea.de/10.1594/PANGAEA.819837). Included are readme files in each directory listing the data contents, a detailed description of data, and contact information for additional details.

Summary

Data presented in this paper are unique because 1) they capture complicated snow-soil-streamflow dynamics from the climatically sensitive rain-snow transition zone, and 2) they present a complete representation of the data required to characterize the hydrologic processes in this catchment. Spatial GIS data are derived from a LiDAR data set and represent the TL catchment topography and vegetation at a 2.5 m resolution. 57 surface soil texture data points and 14 soil texture profiles are presented. Hourly weather data have been gap-filled and are continuous. Snow cover data are extensive and include continuous snow depths from 6 locations and 10 detailed weekly snow surveys. Catchment response data include stream discharge at the basin outlet and soil moisture from multiple depths at seven locations in the basin.

Acknowledgements

We thank Mark Seyfried and Adam Winstral for assisting in the preparation of this manuscript, Lucas Spaete at Boise Center Aerospace Laboratory with LiDAR processing, Justin Huntington for soil profile installation, Erik Boe for snow depth data, and Molly Gribb for soil texture analysis. We thank the Northwest Watershed Research Center and Boise State University Department of Geosciences, Student Research Initiative, and Graduate College for funding and travel support, and general support. NASA EPSCoR and INRA provided funding for this project. The collection and processing of the data presented in this paper were funded in part by NSF-CBET (0854553, 08522), USDA-ARS CRIS Snow and Hydrologic Processes in the Intermountain West (5362-13610-008-00D), USDA-NRCS Water and Climate Center-Portland, Oregon (5362-13610-008-03R), NSF-EPS (0919514), and NOAA (NA08NWS4620047). Any reference to specific equipment types or manufacturers is for information purposes and does not represent a product endorsement or recommendation. Boise State University and the USDA ARS are equal opportunity employers.

References

Aishlin, P. and J.P. McNamara (2011), Bedrock infiltration and mountain block recharge accounting using chloride mass balance, *Hydrol. Process.,* 25(12), 1934-1948, doi: 10.1002/hyp.7950.

Cayan, D. R., S. A. Kammerdiener, M. D. Dettinger, J. M. Caprio, and D. H. Peterson (2001), Changes in the onset of spring in the western United States, *Bulletin of the American Meteorological Society*, 82(3), 399-415, doi: 10.1175/1520-0477(2001)082<0399:citoos>2.3.co;2.

Conger, S. M., and D. M. McClung (2009), Comparison of density cutters for snow profile observations, *J. of Glac.*, 55(189), 163-169, doi:10.3189/ 002214309788609038.

Conway, H., and C.F. Raymond (1993), Snow stability during rain, *J. of Glac.*, 39(133), 635-642, Accession Number: WOS:A1993NA69200022.

Cuo, L., T. K. Beyene, N. Voisin, F. Su, D. P. Lettenmaier, M. Alberti and J. E. Richey (2011), Effects of mid-twenty-first century climate and land cover change on the hydrology of the Puget Sound basin, Washington, *Hydrol. Process.*, 25(11), 1729–1753, doi: 10.1002/hyp.7932.

Feiccabrino, J., A. Lundberg, and D. Gustafsson (2012), Improving surface-based precipitation phase determination through air mass boundary identification, Hydrology Research, 43(3), 179-191, doi:10.2166/nh.2012.060.

Geroy, I. J., M. M. Gribb, H. P. Marshall, D. G. Chandler, S. G. Benner, and J. P. McNamara (2011), Aspect influences on soil water retention and storage, *Hydrol. Processes*, 25(25), 3836-3842, doi:10.1002/hyp.8281.

Gribb, M. M., I. Forkutsa, A. Hansen, D. G. Chandler, and J. P. McNamara (2009), The Effect of Various Soil Hydraulic Property Estimates on Soil Moisture Simulations, *Vadose Zone Journal*, 8(2), 321-331, doi: 10.2136/vzj2008.0088.

Hanson, C., M.D. Burgess, J.D. Windom and R.J. Hartzmann (2001), New Weighing Mechanism for Precipitation Gauges, *J. Hydrol. Eng.*, 6(1), 75-77, doi: 10.1061/(ASCE)1084-0699(2001)6:1(75).

Hanson, C., F. Pierson, and G. Johnson (2004), Dual-Gauge System for Measuring Precipitation: Historical Development and Use, *J. Hydrol. Eng.*, 9(5), 350–359, doi: 10.1061/(ASCE)1084-0699(2004)9:5(350).

Harr, R. D. (1986), Effects of clearcutting on rain-on-snow runoff in western Oregon – a new look at old studies, *Water Res. Res.*, 22(7), 1095-1100, doi: 10.1029/WR022i007p01095.

Judson, A., and N. Doesken (2000), Density of freshly fallen snow in the Central Rocky Mountains, *Bulletin of the American Meteorological Society*, 81(7), 1577-1587, doi: 10.1175/1520-0477(2000)081<1577:doffsi>2.3.co;2.

Kattelmann, R. (1996), Flooding from rain-on-snow events in the Sierra Nevada, *IAHS Publications-Series of Proceedings and Reports-Intern Assoc. Hydrological Sciences*, 239, 59-66, http://itia.ntua.gr/hsj/redbooks/239/iahs_239_0000.pdf#page=69.

Marks, D., J. Domingo, D. Susong, T. Link and D. Garen (1999), A spatially distributed energy balance snowmelt model for application in mountain basins, *Hydrol. Processes*, 13(12-13), 1935-1959, doi:10.1002/(SICI)1099-1085(199909)13:12/13 <1935::AID-HYP868>3.0.CO;2-C.

Marks, D., J. Kimball, D. Tingey, and T. Link (1998), The sensitivity of snowmelt processes to climate conditions and forest cover during rain-on-snow: a case study of the 1996 Pacific Northwest flood, *Hydrol. Processes*, 12(10-11), 1569-1587, doi: 10.1002/(SICI)1099-1085(199808/09)12:10/11<1569::AID-HYP682>3.0.CO;2-L.

Marks, D., A. Winstral, M. Reba, J. Pomeroy and M. Kumar (2013), An evaluation of methods for determining during-storm precipitation phase and the rain/snow transition elevation at the surface in a mountain basin, *Adv. Water Resour.*, 55, 98-110, doi:10.1016/j.advwatres.2012.11.012.

McCabe, G. J., M. P. Clark, and L. E. Hay (2007), Rain-on-snow events in the western United States, *Bulletin of the American Meteorological Society*, 88(3), 319-328, doi: 10.1175/bams-88-3-319.

McNamara, J. P., D. Chandler, M. Seyfried and S. Achet (2005), Soil moisture states, lateral flow, and streamflow generation in a semi-arid, snowmelt-driven catchment, *Hydrol. Processes*, 19(20), 4023-4038, doi:10.1002/hyp.5869.

Miller, C.R., P.S. Routh, T.R. Brosten and J.P. McNamara (2008), Application of time-lapse ERT imaging to watershed characterization, *Geophysics*, 73(3), G7-G17, doi: 10.1190 /1.2907156.

Morin, S., Y. Lejeune, B. Lesaffre, J.-M. Panel, D. Poncet, P. David, and M. Sudul (2012), A 18-yr long (1993-2011) snow and meteorological dataset from a mid-altitude mountain site (Col de Porte, France, 1325 m alt.) for driving and evaluating snowpack models., *Earth System Science Data*, 4(1), 13-21, doi: 10.5194/essdd-5-29-2012.

Mote, P.W. (2003), Trends in snow water equivalent in the Pacific Northwest and their climatic causes, *Geophysical Research Letters*, 10(12), 1601, doi:10.1029/ 2003GL017258.

Nayak, A., D. Marks, D. G. Chandler, and M. Seyfried (2010), Long-term snow, climate, and streamflow trends at the Reynolds Creek Experimental Watershed, Owyhee Mountains, Idaho, United States, Water Resources Research, 46, 15, doi:10.1029 /2008wr007525.

Nayak, A., D. G. Chandler, D. Marks, J. P. McNamara, and M. Seyfried (2008), Correction of electronic record for weighing bucket precipitation gauge measurements, *Water Resour. Res.*, 44(4), doi: 10.1029/2008wr006875.

Nolin, A.W. and C. Daly (2006), Mapping "at risk" snow in the Pacific Northwest, *Journal of Hydrometeorology*, 7(5), 1164-1171, doi: 10.1175/jhm543.1.

Reba, M. L., D. Marks, M. Seyfried, A. Winstral, M. Kumar, and G. Flerchinger (2011), A long-term data set for hydrologic modeling in a snow-dominated mountain catchment, *Water Resour. Res.*, 47(7), doi:10.1029/2010WR010030.

Reba, M. L., J. Pomeroy, D. Marks, and T. E. Link (2012), Estimating surface sublimation losses from snowpacks in a mountain catchment using eddy covariance and turbulent transfer calculations, *Hydrol. Processes*, 26(24), 3699-3711, doi: 10.1002/hyp.8372.

Seyfried, M., C. Hanson, A. Murdock, and S. Van Vactor (2001a), Long-term lysimeter database, Reynolds Creek Experimental Watershed, Idaho, United States, *Water Resour. Res.*, 37(11), 2853-2856, doi: 10.1029/2001WR000413.

Seyfried, M., G. Flerchinger, M. Murdock, C. Hanson, and S. Van Vactor (2001b), Long-term soil temperature database, Reynolds Creek Experimental Watershed, Idaho, United States, *Water Resour. Res.*, 37(11), 2843-2846, doi: 10.1029/2001WR000418.

Shallcross, A. (2012), LiDAR Investigations of Snow Distribution in Mountainous Terrain, M.S. thesis, 62 pp., Dep. of Geosci., Boise State University http://scholarworks.boisestate.edu/td/349/.

Smith, T. J., J. P. McNamara, A. N. Flores, M. M. Gribb, P. S. Aishlin, and S. G. Benner (2011), Small soil storage capacity limits benefit of winter snowpack to upland vegetation, *Hydrol. Processes*, 25(25), 3858-3865, doi: 10.1002/hyp.8340.

Streutker, D. R., and N. F. Glenn (2006), LiDAR measurement of sagebrush steppe vegetation heights, *Remote Sensing of Environment*, 102(1-2), 135-145, doi: 10.1016/j.rse.2006.02.011.

Sui, J., and G. Koehler (2001), Rain-on-snow induced flood events in Southern Germany, *J. Hydrol.*, 252(1-4), 205-220, doi: 10.1016/s0022-1694(01)00460-7.

Surfleet, C. G., and D. Tullos (2013), Variability in effect of climate change on rain-on-snow peak flow events in a temperate climate, *J. Hydrol.*, 479(0), 24-34, doi: 10.1016/j.jhydrol.2012.11.021.

Tesfa, T. K., D. G. Tarboton, D. G. Chandler, and J. P. McNamara (2009), Modeling soil depth from topographic and land cover attributes, *Water Resour. Res.*, 45(10), doi: 10.1029/2008WR007474.

Western, A. W., and R. B. Grayson (1998), The Tarrawarra data set: Soil moisture patterns, soil characteristics, and hydrological flux measurements, *Water Resour. Res.*, 34(10), 2765-2768, doi:10.1029/98wr01833.

Williams, C. J., J. P. McNamara, and D. G. Chandler (2009), Controls on the temporal and spatial variability of soil moisture in a mountainous landscape: the signature of snow and complex terrain, *Hydrology and Earth System Sciences*, 13(7), 1325-1336, doi: 10.5194/hess-13-1325-2009.

Winstral, A., D. Marks and R. Gurney (2013), Simulating wind-affected snow accumulations at catchment to basin scales, *Adv. Water Resour.*, 55, 64-79, http://dx.doi.org/10.1016/j.advwatres.2012.08.011.

Winstral, A., and D. Marks, (2013), Long-term snow distribution observations in a mountain catchment: assessing variability, self-similarity and the representativeness of an index site, *Water Resour. Res.*, in revision.

Yenko, M. (2003), Hydrometric and Geochemical Evidence of Streamflow Sources in the Upper Dry Creek Experimental Watershed, Southwestern Idaho, M.S. thesis, 116 pp., Dep. of Geosci., Boise State University, http://earth.boisestate.edu/drycreek/publications/.

CHAPTER THREE: SNOW DISTRIBUTION, MELT, AND SURFACE WATER INPUTS TO THE SOIL IN THE MOUNTAIN RAIN-SNOW TRANSITION ZONE

Authors

Patrick R. Kormos[1]

Danny Marks[2]

James P. McNamara[1]

H.P. Marshall[1]

Adam Winstral[2]

Alejandro Flores[1]

1. Boise State University, Department of Geosciences

2. Agricultural Research Service, Northwest Watershed Research Center

Abstract

The timing, magnitude, and spatial distribution of snow cover and the resulting surface water inputs (SWI) are quantified for a catchment in the rain-snow transition zone. SWI are fundamental controls on soil moisture, streamflow generation, groundwater recharge, and nutrient cycling. Although the timing of melt events is similar across the basin, southwest facing slopes receive smaller and more frequent SWI from mid winter snow melt, while the northeast facing slope receives more SWI during the spring. Three spatial patterns are observed in modeled SWI time series: 1) uniform, 2) majority of SWI on southwest facing slopes, and 3) majority of SWI on northeast facing slopes. Although any of these three spatial patterns can occur during the snow season, four emergent SWI patterns emerge through the melt season: 1) near uniform, 2) controlled by topographic differences in energy fluxes, 3) transitional, and 4) controlled by snow distribution. Differences in SWI between hill slopes were less than expected during rain-on-snow events. Turbulent fluxes dominated the snowpack energetics in four of the five rain-on-snow events. Advective fluxes are greater than 17% during the 2 rain-on-snow events in December and January. Net radiation fluxes dominate spring melt events. Variations in the method used to distribute precipitation may result in large differences in total precipitation to the basin.

Introduction

The hydrology of mountain basins is largely controlled by the distribution and timing of water delivery to the soil. Water delivered to the soil, or surface water input (SWI), in a snow environment can originate by melt draining from the snow cover or rain falling directly on the ground. The timing, magnitude, and spatial distribution of SWI to

a catchment are fundamental controls on patterns of soil moisture (Seyfried et al., 2011; Seyfried et al., 2009), streamflow generation (Krajewski et al., 1991; Moore et al., 1991), groundwater recharge (Gee and Hillel, 1988; Scanlon et al., 2006), and nutrient cycling (Austin et al., 2004; Schmidt and Lipson, 2004). When rain falls on bare ground, SWI is solely dependent on the timing, magnitude, and distribution of precipitation. However, when precipitation falls as snow, or when the ground is snow covered regardless of precipitation phase, SWI is complicated by energy, climate, and terrain factors. Snow cover temporarily stores water at the ground surface until it melts so that SWI depends on a combination of the snow energy balance and the timing, magnitude, and distribution of precipitation (Marks and Dozier, 1992; Marks and Winstral, 2001). Falling snow is susceptible to differential accumulation according to wind fields (Winstral and Marks, 2002; Winstral et al., 2009; Winstral et al., 2013). Once on the ground, melt can be heterogeneous due to terrain factors that control solar and thermal radiation (Marks et al., 2002). A time lag may exist between snow melt and when it enters the ground as SWI due to the transmission properties of snow (Colbeck, 1975). Melt water can move laterally in a sloping snowpack from the point of origin to the point where it enters a catchment (Eiriksson et al., 2013). Differential accumulation and melt by these factors can produce spatially discontinuous snow packs, which add new issues such as lateral energy transfer from bare soil to snow (Liston, 1995). Rain falling on discontinuous snow cover will further complicate the prediction of runoff from rain-on-snow (ROS) events. Several studies have documented the highly heterogeneous nature of snow water equivalent (SWE) on the ground (Anderton et al., 2004; Pomeroy et al., 2002), however

few studies have taken the next step to investigate the more hydrologically relevant problem of heterogeneous SWI.

Slope aspect, henceforth referred to simply as aspect, impacts many of the processes that affect SWE and SWI in the mountainous western U.S. For example, wind can cause more snow to accumulate on lee versus windward slopes (Elder et al., 1991; Hiemstra et al., 2002; Luce et al., 1998; Winstral and Marks, 2002), aspect-driven differential insolation can cause melt heterogeneity (Elder et al., 1991; Marks and Dozier, 1992), and vegetation differences related to aspect can impose differential interception and snow trapping across a catchment (Gutierrez-Jurado and Vivoni, 2013; Ivanov et al., 2008; Molotch et al., 2009). Consequently, many studies have documented relationships between snow cover and terrain structure; north-facing slopes tend to store more SWE than south facing slopes (Erxleben et al., 2002; Golding and Swanson, 1986; Jost et al., 2009; Jost et al., 2007; Williams et al., 2009). The impact of aspect on SWI is less clear. For example, in a mountain catchment in Colorado, U.S., it was reported that snow accumulation was consistently higher on north facing versus south facing slopes (Hinckley et al., 2012). Accumulated SWI over the year could be higher on south facing slopes depending on the distribution of precipitation.

SWI is further complicated in mid-elevation zones of the mountainous western U.S. near the margins of a continuous snowpack. This mid-elevation zone is commonly called the *rain-snow transition zone*. We define the rain-snow transition zone as the elevation band in temperate mountains where the dominant winter precipitation phase is variable, and changes from rain at lower elevations to snow at higher elevations. The elevation of this zone varies from sea level at high latitudes (Feiccabrino et al., 2012) to

over 2000 m at lower latitudes (Cayan et al., 2001). This zone typically occurs from 1500 m to 1800 m in the interior Pacific Northwestern U.S. and covers approximately 9200 km^2 (Nolin and Daly, 2006). Snow cover in this region is dynamic, sometimes accumulating significant depth in a series of cold storms that deposit snow, but often being thin and patchy.

Precipitation in the rain-snow transition zone can fall as rain or snow making the region highly susceptible to ROS events. These events often contribute to large floods (Harr, 1986; Kattelmann, 1996; Marks et al., 1998; McCabe et al., 2007; Sui and Koehler, 2001; Surfleet and Tullos, 2013) and major avalanche cycles (Conway and Raymond, 1993). While snow melt is generally enhanced during ROS events, the addition of water to the snowpack is not often the cause. Rather, the mechanism for increased snowmelt is generally recognized as an increase in turbulent energy fluxes associated with condensation during stormy weather conditions (Berris and Harr, 1987; Marks et al., 1998), although Mazurkiewicz *et al*. (2008) reported that an increase in net all-wave radiation could also be important at wind-protected sites.

Although the above mentioned complications have been overcome to varying degrees when simulating more continuous, seasonal snow packs (*see* Garen and Marks, 2005; Liston and Elder, 2006; Price and Dunne, 1976; Seyfried et al., 2009; Wigmosta et al., 1994), snow modeling is particularly difficult over an ephemeral snow cover in the rain-snow transition zone. In a mountain basin, the rain-snow transition zone typically occurs at the boundary between the snow- and rain-dominated regions. Snow simulation models, such as those cited above, have been optimized for the snow zone and, in general, are less effective over shallow ephemeral snow. Small variations in forcing data

and estimated precipitation distribution can result in large uncertainties over the shallow, ephemeral snow cover that "comes and goes" in the rain-snow transition zone. These uncertainties would have a negligible effect over a better developed, deeper, and more substantial snow cover. Small variations in energy fluxes are capable of causing significant variations in snow temperature and/or melt because of the low thermal mass of a thin snow cover (Pomeroy et al., 2003; Williams et al., 2009). Ground heat is more important to the energetics of a thin snowpack. Shallow snow is further warmed by incoming solar radiation penetrating the snowpack and being absorbed and reemitted by low-lying vegetation and the ground surface (Knox et al., 2012).

The goal of this study is to understand the complex nature of the distribution of SWI to catchments in the rain-snow transition zone where the ephemeral snowpack is developed and ablated several times during the season. SWI is difficult to measure directly (sampling methods dramatically alter the surface energetics). Conventional melt lysimeters inhibit ground snow energy exchanges, which are more important for shallow, developing snow than for a deep, well-developed snowpack. Though it will be a challenge, we have elected to use a distributed, physically based snow accumulation and melt model in coordination with field observations to investigate SWI in a highly instrumented micro-catchment in the rain-snow transition zone of the Dry Creek Experimental Watershed (DCEW) in southwest Idaho. Although simpler temperature index models have been applied over glaciers (Hock, 1999; Pellicciotti et al., 2005), they are not appropriate over mountain basins, as show by Walter *et al.* (2005) and more definatively by Kumar *et al.* (2013), where precipitation and surface energy fluxes are highly variable in space and time. For this investigation, we use a LiDAR-derived

elevation dataset to distribute highly resolved time series data described in Kormos *et al*. (2013) to force and validate the *i*mage SNOw energy and mass BALance model (iSNOBAL). Understanding how SWI is generated and delivered to mountain basins in the rain-snow transition zones, and how these processes impact soil moisture, groundwater recharge, and streamflow is critical to managing water and ecosystems in the western North America. In this paper, we undertake the challenge of applying an energy balance snow model over an ephemeral snow cover in the rain-snow transition zone to provide insight into 1) how mixed phase precipitation in this region controls the timing and distribution of SWI, 2) the interaction between terrain structure, wind, and precipitation distribution on snow cover development, and 3) ephemeral snowpack energetics during ROS and spring melt events.

Study Site

The Treeline experimental catchment (TL) is a 1.5 hectare sub basin of the Dry Creek Experimental Watershed (DCEW) established in 1999 to investigate hydrologic processes in the semi-arid foothills 13 km north of Boise, Idaho (Figure 3.1). DCEW elevation ranges from 1030 to 2130 masl and consists of higher elevation forests that are snow-dominated and lower elevation grasslands that are rain-dominated. TL is a relatively steep catchment with a mean slope angle of 21 degrees and an elevation range from 1600 to 1645 masl, which conveniently situates it at both the vegetation and precipitation phase transition zones. The catchment boundary is delineated from an airborne LiDAR elevation data set acquired in 2010 (Shallcross, 2012). Soils are thin (20 – 125 cm), sandy, and overlie biotite granodioritic bedrock (Williams et al., 2009). Vegetation on the northeast-facing (NE) slope is typified by an abundance of sagebrush

and *ceanothus*, *prunus ssp.*, forbs, and grasses, while vegetation on the southwest-facing (SW) slope is sparser and contains mostly grasses, forbs, and a few smaller shrubs. There are 8 conifer trees in the catchment that are assumed to have negligible influence on the snow energy balance for the purpose of this study.

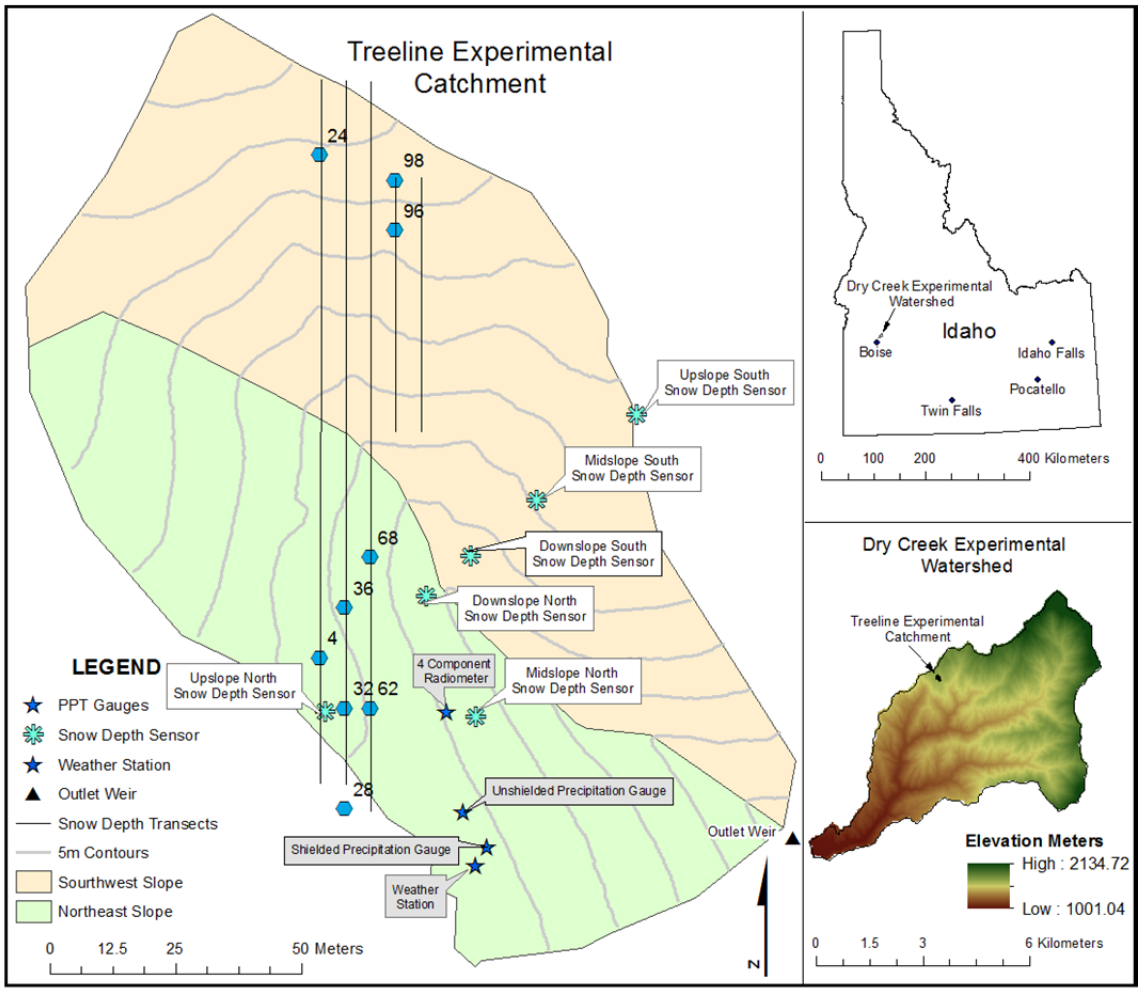

Figure 3.1 Location map of TL subcatchment of DCEW in Southwest Idaho showing instrument and measurement locations.

Precipitation falls during the fall, winter, and spring seasons while being largely absent from the summer months. TL received approximately half of the winter precipitation (October 1st - April 1st) as rain or mixed events during WY2011 (Figure

3.2). Most winter precipitation at TL falls when the dew point temperature is close to zero (Figure 3.3). The mix of precipitation phase and the dew point temperature distribution for the period of record (Figures 3.2 and 3.3b) at TL highlights the fact that it is situated within the rain-snow transition zone. Stream discharge from TL is intermittent, initiating in the early winter and ceasing in early summer. Snow cover on the SW slope tends to experience several full melt and accumulation cycles, while the NE slope tends to retain a seasonal snowpack.

The TL meteorological station and precipitation gauges are located on the southwest ridge above the NE slope (Figure 3.1). The model forcing and validation data from TL used in this study is described in Kormos *et al.* (2013). Air temperature, relative humidity, incoming solar radiation, average wind speed, ground temperature, and shielded and unshielded precipitation are recorded hourly. Incoming and outgoing solar and thermal radiation are measured at a four-component radiometer on the NE slope. Snow depth is recorded at six ultra sonic depth sensors that form a transect from the southwest ridge to the northeast ridge. Ten weekly snow surveys were conducted from January 21 to March 24, 2011. Between five and nine snow density samples were collected across aspects from each survey. Between 105 and 395 snow depths were recorded in five transects each week.

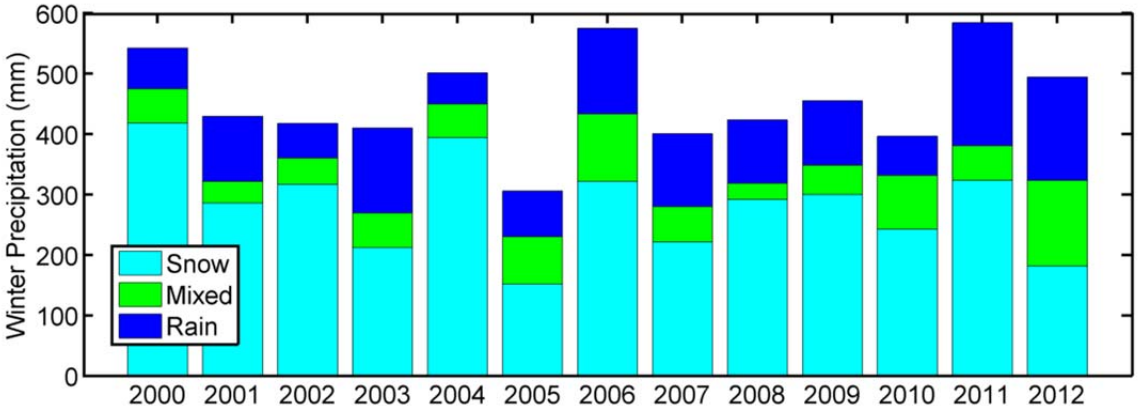

Figure 3.2 Precipitation phase during winter months (October 1st - April 1st) showing the amount of rain, snow, and mixed events for the period of record.

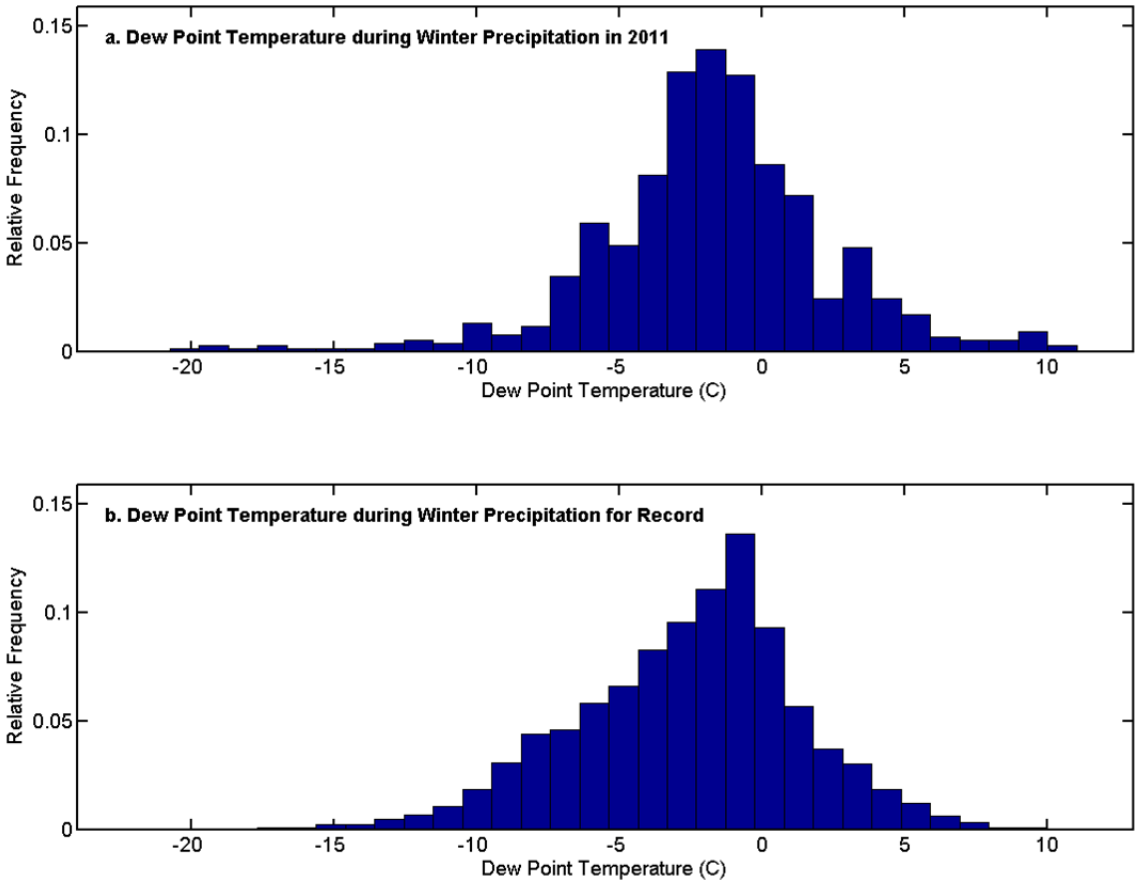

Figure 3.3 Dew point temperature distribution during precipitation for winter months (October 1st - April 1st) showing a) the WY2011 data compared to b) the period of record (1999-2012).

Methods

All software utilities used for this research, including the iSNOBAL snow simulation model are available from *Software tools for hydro-climatic modeling and analysis: Image Processing Workbench, ARS-NWRC Version 2.1,* developed by the Northwest Watershed Research Center, USDA Agricultural Research Service, in Boise, ID (see http://199.133.140.121/ nwrc/ipw/intro.html/)

Surface *water input* (SWI) is water that enters the soil as rain, rain that passes through the snow, or melt water draining from the base of the snow. We simulated the distribution of SWI over the catchment using the iSNOBAL physically based distributed energy balance model to simulate the snow cover from October 1st, 2010 to October 1st, 2011 (WY2011). iSNOBAL (Marks et al., 1999) is a two layer model that uses the catchment topography and distributed estimates of meteorological forcings to estimate the snow storage for a given time step. iSNOBAL has been extensively applied and validated to investigate snow physics, processes, and the distributed melt patterns over complex terrain as well as ROS events at many locations within the mountains of western North America (Marks et al., 1998; Marks et al., 2001; Marks et al., 2002; Winstral and Marks, 2002; Winstral et al., 2009). The model simulates both the development and ablation of the snow cover, estimating SWE, melt, liquid water content, and SWI from the base of the snowpack from input precipitation and available energy. The energy balance of the snowpack at each model pixel is expressed as:

$$\Delta Q = S_{net} + H + L_v E + G + M, \quad (1)$$

where ΔQ is change in snowpack energy, and S_{net}, H, L_vE, G, and M are net radiative, sensible, latent, conductive, and advective energy fluxes respectively (Marks and Dozier, 1992). The model represents the snow as a two-layer system, with a fixed-thickness surface layer, and a variable thickness lower layer representing the remainder of the snow cover. If ΔQ is negative, the snow will cool, increasing its "cold content" or the amount of energy required to bring the snow to 0˚C. If ΔQ is positive the snow will warm, reducing its cold content. Once the snow is at 0˚C, the cold content is zero, and any addition of energy will result in melt. The simulated snow cover retains a specified threshold of liquid water. If the addition of liquid water to the snow by either melt or rain exceeds this threshold, the excess is released to the soil as SWI. If the ground is bare, the model passes precipitation that falls as rain to the soil as SWI.

The model is run at an hourly time step over a 2.5 m^2 DEM grid (2575 pixels). A high-resolution areal LiDAR derived topographic data set provides detailed topographic information, which makes modeling at this fine spatial scale beneficial. The high spatial resolution also avoids more complicated methods of dealing with the ephemeral snow cover in the basin. Since snow cover differs with aspect, this study will focus on the spatial distribution of net radiation and precipitation. S_{net} is calculated from net solar radiation and incoming longwave radiation. Outgoing longwave radiation is calculated from modeled active layer snow temperature. H and L_vE are calculated from wind speed, air temperature, vapor pressure, and a uniformly distributed surface roughness parameter of 0.005 m. The roughness length was determined by manual calibration of a point version of the model (SNOBAL) at the mid-slope snow depth sensor on the NE slope. G is calculated from measured soil temperature and simulated snow temperature. Marks *et*

al. (2013) showed definitively that, in the mountain environment, dew point temperature is equivalent to precipitation temperature. M is therefore based upon dew point temperature and precipitation mass.

Net Solar Radiation

Clear sky incoming solar radiation is distributed over the DEM using the utility STOPORAD, which calculates separate incoming clear-sky visible and Near-Infrared (NIR) solar radiation for each model pixel based on slope, aspect, and location of the sun at each time step (Dozier, 1980; Dozier and Frew, 1981; Dubayah, 1994). The 2.5 m digital elevation (DEM) model extends a minimum of 80 m beyond the boundary of the catchment is used to account for shading effects of adjacent topography. Calculated solar radiation values are corrected to measured values from the weather station for each time step to account for cloud cover. Shading by vegetation canopy is considered negligible because of the low number of trees and the low-lying plant community that is quickly covered by snow accumulation. Spectral albedo is estimated from theoretical and empirical models for visible and NIR wavelengths based on grain size and sun angle (Marshall and Warren, 1987; Warren and Wiscombe, 1980; Wiscombe and Warren, 1980), using methods presented by Marks and Dozier (1992).

Calculated albedo is further degraded for litter and debris accumulation (Link and Marks, 1999) between maximum accumulation (March 30, 2011 at midnight) and snow melt out (noon, April 12, 2011). To do this, we use a LiDAR-derived raster of maximum vegetation height (Kormos *et al*., 2013) to divide TL into 4 albedo decay zones: conifer tree, *prunus ssp*., windblown litter influence, and open. The conifer tree and *prunus ssp*. classes were determined from the vegetation height map as greater than 10 m and

between 2 m and 10 m, respectively. The windblown litter zone was estimated by creating a 30 m buffer around trees. The open class contained all pixels less than 2 m height and outside of the 30 m buffer around the conifer trees. Albedo decay factors are created for each class by linearly interpolating from 0 at peak accumulation to the maximum decay factor for that cover type at meltout. A maximum decay factor of -0.36 for conifers, -0.30 for *prunus ssp*., -0.27 for windblown litter, and -0.25 for open classes are used based on work from Winstral *et al*. (2013) and Reba *et al*. (2011a, b) in an area with similar vegetation. These decay factors are then added to calculate visible and NIR albedo values. Outgoing visible and NIR solar radiation is then obtained by multiplying the incoming solar radiation by the degraded albedo values.

Incoming Thermal Radiation

Clear sky incoming thermal radiation is distributed using TOPOTHERM, which accounts for elevation, air temperature, and dew point temperature, and is then corrected for adjacent terrain (Marks and Dozier, 1979), and for canopy effects using methods presented by Link *et al*. (2004) and refined by Pomeroy et al. (2009). Calculated incoming thermal values are then corrected to measured values (Kormos, *et al.,* 2013) for each time step to account for cloud cover.

Temperature, Wind Speed, and Humidity

Air temperature, ground temperature, and wind speed are uniformly distributed since the size of the catchment is small. Vapor pressure and dew point temperature were calculated from measured air temperature and relative humidity and uniformly distributed

across the basin. The soil temperature from 5 cm soil depth from Profile 3 (Figure 3.1) on the NE slope was uniformly distributed across the catchment.

Precipitation

Wind corrected precipitation was distributed following a modified version of the methods presented by Winstral *et al.* (2013). Storms, which were defined as consecutive time steps with measured precipitation less than 3 hours apart, were distributed if the storm-averaged dew point temperature was less than -0.5 ˚C and the storm total was more than 7 mm. Twenty storms met these criteria for WY2011. A unique accumulation ratio (AR), or fraction of the measured wind-corrected precipitation, for each pixel is calculated for storms using the distributed maximum upwind slope (*Sx*) and slope break (*Sb*) parameters, both of which are functions of the topography and storm-averaged wind direction. *Sx* is calculated from a user-defined maximum search distance (*dmax*) and terrain obstruction height, referred to as *instrument height* by Winstral et al. (2009; 2013). *Sb* is a function of *Sx* and a specified separation distance parameter. Drift zones are delineated from the catchment parameters *dmax*, the *Sb* angle threshold, *instrument height*, and separation distance. A suggested separation distance of 60 m was held constant during this exercise because it produced realistic precipitation distributions. The AR outside drift zones was obtained for each pixel using the empirical equation developed in Winstral *et al.* (2013) and modified using:

$$(1 - AR) \times P1 + AR, \tag{3}$$

where *P1* is a parameter that effectively reduced the difference between the original AR parameter and 1 (no modification to wind-corrected, measured precipitation) by a factor of *P1* (see Winstral *et al.,* 2013). This method was used to make *AR* more applicable to

areas with less wind scour than the area where the equation was developed. Although we intended to use the empirical equation presented in Winstral *et al*. (2013) to calculate an *AR* for pixels within the drift zones, low storm wind speeds led to values less than one for all storms. We therefore imposed a minimum *AR* to areas within the drift zones. We objectively varied *dmax*, *Sb* angle threshold, *instrument height*, minimum *drift AR*, and *P1* to achieve the lowest Root Mean Square Error (RMSE) between measured and modeled SWE (Table 3.1). SWE was measured directly at 8 locations. Snow depths measured at the six ultra sonic depth sensors on survey days are converted to SWE using a basin-averaged snow density from surveys.

Results

Accounting for wind redistribution decreased the RMSE between measured and modeled SWE from 82.2 mm to approximately 35 mm (Table 3.1). However, the RMSE is relatively insensitive to the values used to parameterize the redistribution model. The wind redistributed precipitation storm totals range from 230 mm to 270 mm with an average of 253 mm. This is between 100 mm and 60 mm less than the 333 mm storm total from the wind corrected precipitation record. The NE slope receives between 264 mm and 313 mm while the SW slope receives between 203 mm and 241 mm of storm totaled precipitation. The aspect differences in precipitation input have a significant impact on the distributed hydrological processes occurring in the catchment as well as the catchment water balance.

Table 3.1 Wind redistribution parameters and resulting RMSE between measured and modeled SWE. Average storm distributed precipitation for the whole catchment, NE, and SW slopes are presented.

max	*1*	*instrument height*	*in. DAR*	*Sb angle threshold*	MSE	*precipitation total (mm)*	*P recip. north (mm)*	*P recip. south (mm)*
		-		-	2.2	333	33	33
50	.5	3	.1	10	2.9	230	64	03
00	.5	3	.1	10	5.1	232	64	07
00	.5	3	.1	5	2.4	251	94	17
000	.5	3	.1	5	2.6	255	01	19
00	.6	3	.1	5	7.1	270	05	41
00	.55	3	.1	5	4.2	260	00	29
00	.5	3	.2	5	6.5	263	13	23
50	.5	2	.1	5	6.7	260	01	28
00	.5	2	.1	5	6.6	259	97	28

For the purposes of this paper, we use the wind redistribution parameters that achieve the minimum RMSE of 32 mm between measured and modeled SWE at 14 locations in the catchment. The parameters used are a *dmax* of 500 m, AR scaling parameter (*P1*) of 0.5, *instrument height* of 3 m, *minimum drift AR* of 1.1, and a *Sb* angle threshold of 5° (Table 3.1)**.** The resulting precipitation input to the snow model provided a reasonable match to the SW slope ultrasonic depth sensors and at most NE locations (Figure 3.4). We wanted to minimize discrepancies between measured and modeled SWE because that directly impacts the timing and magnitude of simulated SWI. The

midslope NE depth sensor is adjacent to a ponderosa pine tree, which we assumed to have negligible influence on the basin SWE. However, decreased incoming solar radiation from shading may explain why the measured SWE was greater than modeled in January and February. The downslope NE depth sensor is very close to the valley bottom and the head of the channel. Both the aspect and the slope are transitional here and small errors in the DEM may have large impacts on the mass and energy balance. This

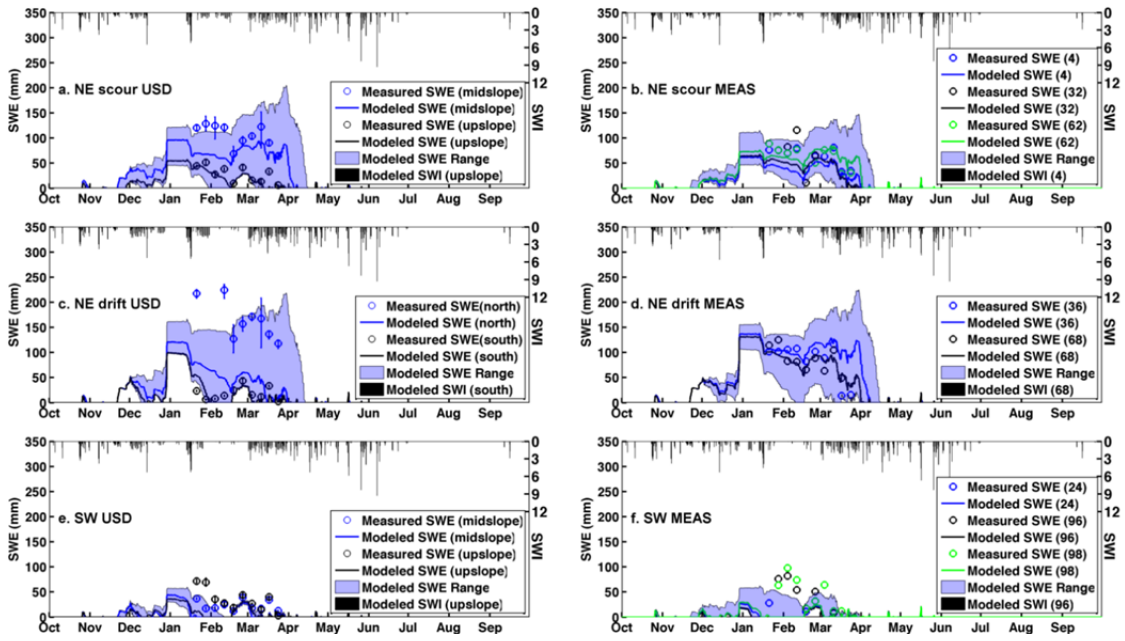

Figure 3.4 Measured and modeled SWE at the 6 ultrasonic depth sensors (USD)(a, c, & e) and 8 measurement locations (MEAS) (b, d, & f). Error bars on depth sensor SWE values are the interquartile range of the snow depth at the time of the survey multiplied by all density measurements from that day. Solid lines indicate the modeled SWE at the pixel where the SWE measurement is located. The shaded regions depict the SWE range from the closest 25 model pixels within 5˚ of the Sb parameter (similar topographic characteristics) of the measurement location. Modeled SWI from specified measurement locations are represented by black bars on the reverse ordinate. Panels a and b are labeled scour because we expect less snow to be deposited here during redistribution. Panels c and d are labeled drift because we expect more snow to be deposited here during redistribution. Panels e and f are points from the southwest facing slope.

site is also near to the bottom of the slope where the SE slope begins, and the "channel" or "notch" between the two is typically filled with wind-blown snow during storms. This

is a micro-scale process that may contribute to an increase in SWE at this location, but is not accounted for in the redistribution model. SW SWE measurements are often near 5 cm after February when the model calculates no snow. Errors in SWE measurements and depths from sensors are within expected spatial variability. The low thermal mass of this shallow snowpack is also very sensitive to small errors in energy balance terms. These small errors in snow cover are expected to have minimal influence on the slope averaged timing and magnitude of SWI to the basin.

There is more snow stored on the NE slope than the SW slope (Figure 3.4). Snow cover is also more continuous on the NE slope, although the modeled SWE range reveals partial snow cover near all measurement locations for much of the winter. The average number of snow covered days on the NE and SW slopes is 143 and 87 days, respectively (Figure 3.5). Snow covered days are calculated as the sum of the hourly time steps with SWE values greater than zero and divided by 24. Although this difference is statistically significant at the 5% level, topographic variations within slope categories that affect the radiation inputs and precipitation distribution lead to a broad spread of the snow covered day data.

The NE slope had an average of 70 mm more total SWI than the SW slope (Figure 3.6). The difference is due to wind redistribution depositing more snow on the NE slope. The wind redistribution procedure resulted in the NE slope getting a pixel

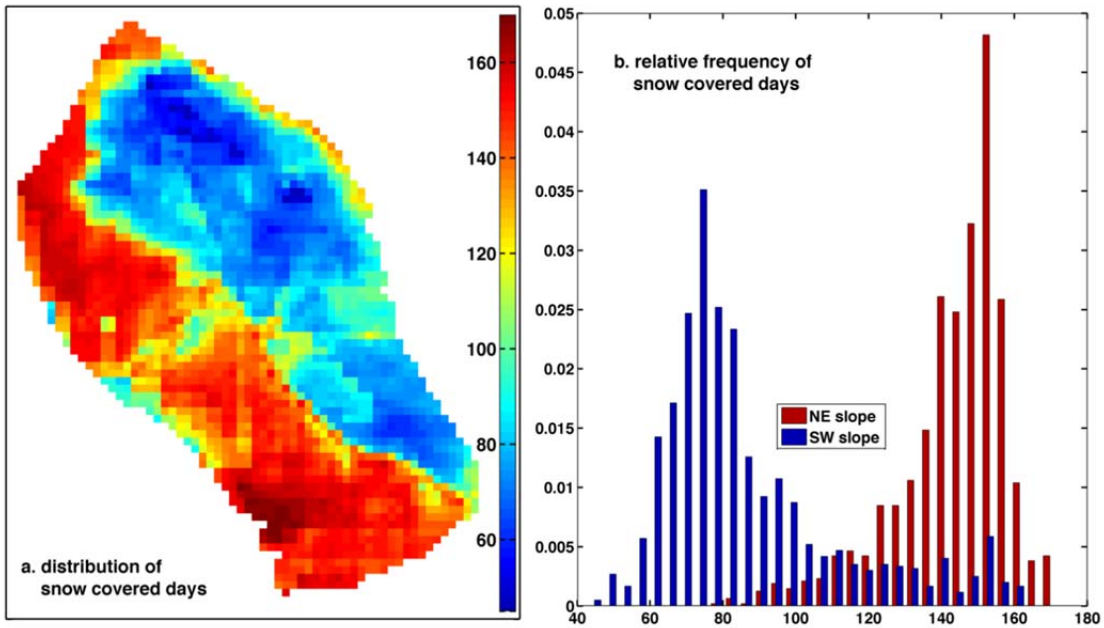

Figure 3.5 a. Model simulated snow covered days at TL for the WY2011. b. The distribution of simulated snow covered days by hill slope.

average of 77 mm more precipitation than the SW slope (Table 3.1). That difference is decreased by higher evaporation from the NE slope. There is a high variability of SWI from both slopes as shown by the inter quartile range and full range of values in Figure 3.6.

Time series of SWI at six locations across the catchment show that the timing of major melt events occur simultaneously (Figure 3.4). Snow melt events are smaller and more frequent on the SW slope from December to mid January, resulting in a higher cumulative SWI. Later melt events on the NE slope begin in February largely because there is more SWE in that location available for melt. The NE slope receives more cumulative SWI beginning in early April.

Five ROS events occur in WY2011 **(**Figure 3.6 and Table 3.2). ROS events produce similar SWI between the NE and SW slopes. The difference in ROS SWI between slopes is attributed primarily to differences in snow distributions. The magnitudes of energy fluxes depend on the time of year that the ROS event occurred. There is a switch from the dominant fluxes being turbulent in the winter to a mix of turbulent and net all-wave radiation in the spring. Advective heat fluxes were significant energy fluxes during the first two mid-winter ROS events. The NE slope has a minimum of 3.6 times more SWE and 1.7 times more snow cover than the SW slope at the onset of ROS events. A two-day spring melt event in which no measurable precipitation fell is included in Table 3.2 for comparison purposes. Radiation fluxes dominate this event.

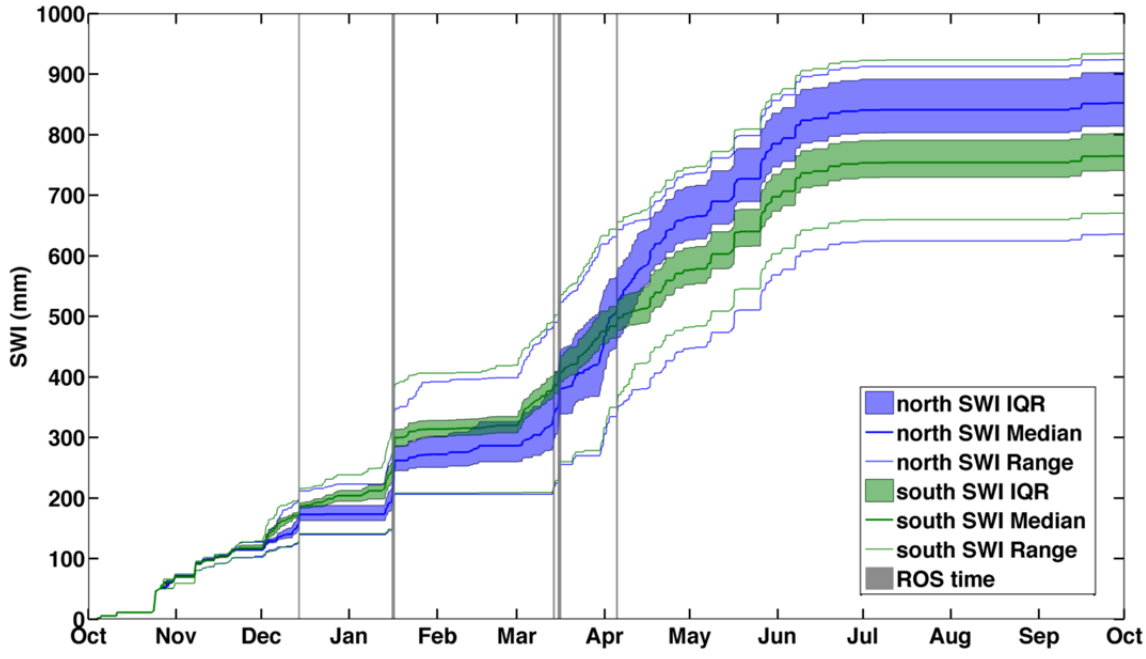

Figure 3.6 Cumulative SWI from NE and SW slopes at TL for WY2011. The timing of ROS events are shown as shaded grey regions.

SWI patterns in TL in WY2011 are controlled by the spatial distribution of snow and/or energy (Table 3.3). Because simulated energy fluxes are unstable over thin, ephemeral snow, we limit the pixels used for the energy summary shown in Table 3.3 to those with a deeper snow cover for the entire two-week period indicated. Only bi-weekly periods from December 26, 2010 to May 1, 2011 have enough snow for this evaluation.

Three SWI patterns occur at TL in WY2011: 1) uniform, 2) greater on SW slopes, and 3) greater on NE slopes (Figure 3.7 and Table 3.3). Although any of the three patterns can occur during a specific bi-weekly period, four emergent SWI periods progress through the snow melt season: 1) near uniform SWI, 2) SWI patterns dominated by the distribution of energy, 3) transitional, and 4) SWI patterns dominated by the distribution of precipitation (Figure 3.8). The total SWI to TL for WY2011 was 812 mm. The SWI total for the snow season (November 20 to April 25) was 499 mm. The SWI during ROS events was 101 mm or approximately 12.5% of the total SWI and 20% of snow season SWI.

Table 3.2 Summary of the snow cover and mass and energy fluxes from the five ROS events that occurred at TL during WY2011. Energetics are slope averages for only pixels with SWE greater than zero.

rain-on-snow time period	precipitation (mm)	total surface water input (mm)		average SWE (mm)		snow covered area		average net allwave radiation flux (W/m^2)		average turbulent flux (W/m^2)		average ground heat (W/m^2)		average advective heat (W/m^2)	
	Basin	North	South	North	South	North	South	North	South	North	South	North	South	North	South
Dec. 14 6:00 to 10:00	13	14	13	23	4	84%	16%	3.52	-7.04	9.62	9.63	1.63	1.66	5.10	5.10
Jan. 16 9:00 to Jan. 17 1:00	34	48	41	101	28	100%	58%	13.23	13.15	39.97	39.29	1.86	2.37	11.95	11.95
Mar. 13 17:00 to Mar. 14 7:00	8	12	8	106	17	83%	11%	-11.84	-24.25	45.72	45.80	1.23	1.19	0.74	0.74
Mar. 15 11:00 to Mar. 16 1:00	23	29	18	95	16	80%	10%	24.01	20.08	25.91	25.94	1.52	1.45	4.94	4.12
Apr. 5 0:00 to 11:00	12	13	12	68	12	59%	8%	18.91	3.81	6.58	6.82	1.54	1.45	1.19	1.19
spring melt event Mar.31 0:00 to Apr. 2 0:00	0	34	5	109	17	79%	9%	34.39	19.33	-6.83	0.67	7.89	10.08	-0.10	0.07
ROS SWI weighted energy fluxes	-	-	-	-	-	-	-	12.68	7.38	29.39	29.14	1.65	1.85	7.10	6.92

Table 3.3 Biweekly snow cover information, mass fluxes, and energy fluxes to the snow pack. Energetics are slope averages for only pixels with SWE greater than 10 cm.

panel	Bi-weekly time period start	Pre-cipita-tion (mm)	SWI NORTH (mm)	SWI SOUTH (mm)	SWE NORTH (mm)	SWE SOUTH (mm)	snow covered area NORTH	snow covered area SOUTH	net allwave radiation NORTH (W/m^2)	net allwave radiation SOUTH (W/m^2)	turbulent flux NORTH (W/m^2)	turbulent flux SOUTH (W/m^2)	ground heat NORTH (W/m^2)	ground heat SOUTH (W/m^2)	delta Q NORTH (W/m^2)	delta Q SOUTH (W/m^2)
e	26-Dec-2010	69.6	0.1	10.5	97.5	44.5	100%	97%	-11.17	-12.07	2.36	3.46	7.23	6.84	-1.46	-1.60
f	9-Jan-2011	77.5	95.7	99.3	102.2	33.7	100%	77%	-7.24	-11.73	6.81	8.89	7.00	6.65	7.35	4.59
g	23-Jan-2011	2.2	11.4	8.6	88.9	18.3	96%	23%	-18.05	-18.15	8.42	9.12	9.81	9.14	0.19	0.12
h	6-Feb-2011	25.3	11.5	5.8	80.6	17.5	91%	35%	-14.71	-15.31	8.20	9.61	8.88	8.58	2.34	2.86
i	20-Feb-2011	30.1	15.1	33.1	104.8	34.3	100%	88%	-6.31	-7.68	1.42	2.86	5.98	5.80	1.09	1.03
j	6-Mar-2011	79.4	85.1	70.8	106.3	19.2	93%	42%	0.90	-1.25	4.34	6.45	3.30	2.89	8.76	8.31
k	20-Mar-2011	74.3	107.0	69.0	103.5	18.1	89%	41%	16.04	15.56	8.32	10.88	2.51	2.14	26.78	28.52
l	3-Apr-2011	40.0	100.6	46.1	42.6	7.8	42%	10%	46.41	50.29	4.69	5.83	4.53	4.99	55.92	61.40
m	17-Apr-2011	48.7	61.0	52.3	2.6	0.9	22%	12%	62.35	116.91	2.15	11.24	7.29	1.49	71.93	130.72

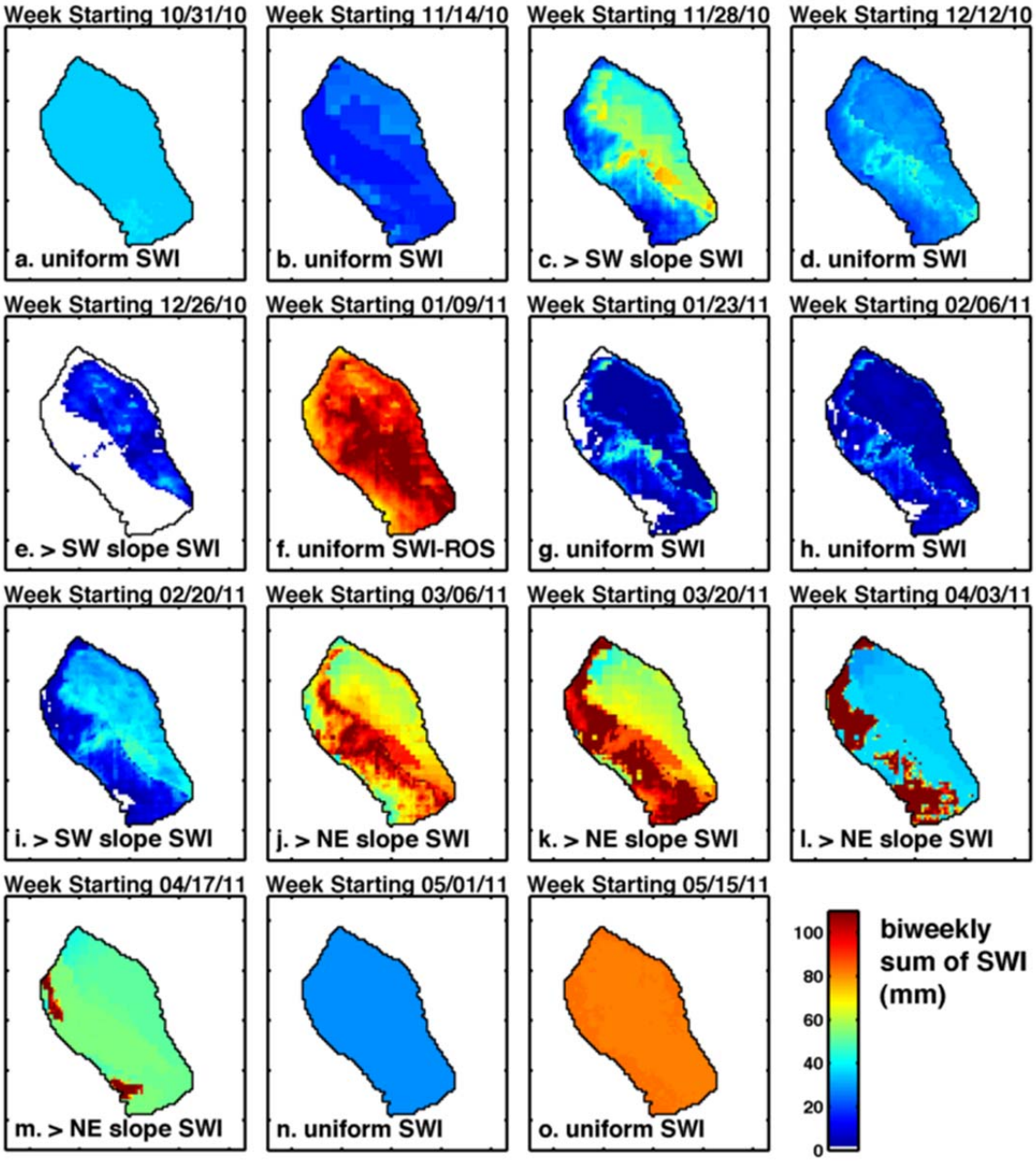

Figure 3.7 Distributed biweekly incremental SWI from October 31, 2010 to May 1, 2011.

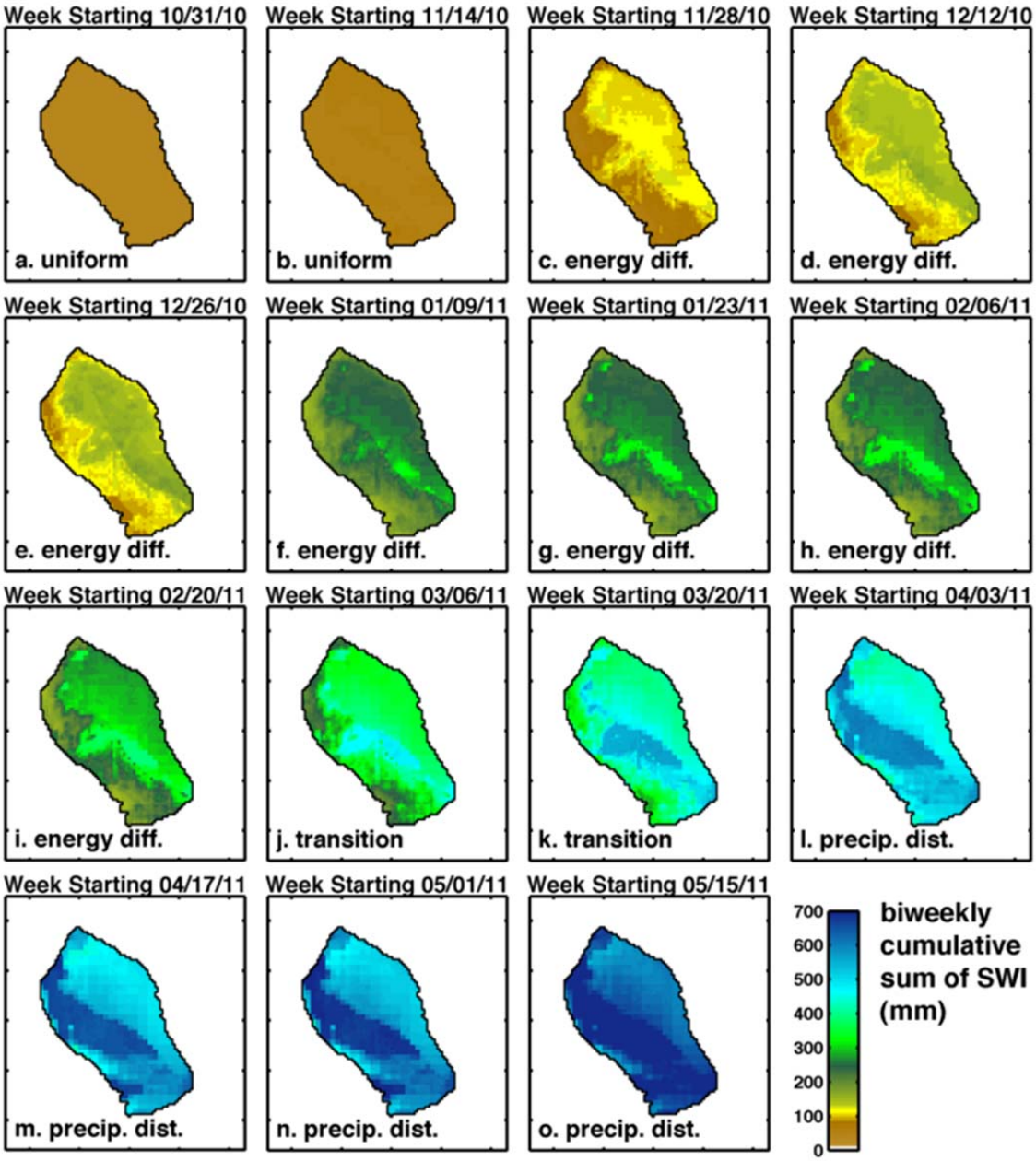

Figure 3.8 Distributed biweekly cumulative SWI from October 31, 2010 to May 1, 2011.

Discussion

Surface Water Input (SWI) Distribution

SWI at TL is highly heterogeneous in time and space as a result of the complex interaction between the heterogeneous and ephemeral snow cover, energy balance, and precipitation distributions, all of which vary systematically with aspect. SWI in the rain-snow transition zone occurs throughout the winter season (Figures 3.4 and 3.6). This is in contrast to higher elevation or colder catchments that have distinct accumulation and ablation periods, where the majority of SWI occurs during the spring melt. Although the timing of SWI from locations on NE and SW slopes appear to occur simultaneously the magnitude of SWI between slopes often varies. Contrasting SWI is likely to occur when there are differences in the amount of SCA on the two slopes. The differences in cumulative SWI between hill slopes highlight heterogeneous timing and magnitude of water availability for catchment processes beginning approximately December 1st (Figure 3.6). This has implications for many catchment processes, including transpiration, streamflow source areas, and the distribution of deep percolation.

The three emergent spatial SWI patterns are a result of distributed energy inputs and precipitation distribution (Figure 3.7 and Table 3.3). Many time periods have near equal (< 7.5 mm difference) SWI between slopes. These time periods are either characterized by having limited SCA on both slopes during precipitation events that include significant rain (panels 7a, 7b, 7n, and 7o), ROS events on ripe snow (panel 7f), or similar inputs of melt energy between slopes (ΔQ) (panels 7d, 7g, and 7h).

Time periods when SW slopes produce more SWI (panels 7c, 7e, and 7i) are controlled by the distribution of energy flux terms. The biweekly time period starting on

November 28, 2010 resulted in 20 mm more SWI to the SW slope, and is characterized by strong radiative cooling on the NE slope that is not overcome by small positive turbulent fluxes. The SW slope had positive net all-wave radiation and ground heat fluxes during this time. The time period beginning on December 26, 2010 has virtually no SWI to the NE slope and an average of 10 mm SWI to the SW slope. Melt on the SW slope is caused by shallow snow energy dynamics, where the ground heat flux to pixels with a very thin snowpack is amplified. These fluxes are not represented in Table 3.3 because those pixels have SWE magnitudes less than the 10 cm cutoff.

The biweekly period starting on February 20, 2011 resulted in 18 mm more SWI to the SW slope. This time period had higher turbulent fluxes on the SW slope (Table 3.3), but is also dominated by shallow snow energy fluxes described above. Most pixels within the shallow snowpack melted out completely, as is seen by the decrease of snow covered area (SCA) from 83% to 41% from the previous period.

Later in the season, preferential retention of snow and precipitation redistribution during storms produces more SWI on NE slopes (panels 7j, 7k, 7l, and 7m). Note that the majority of the snow late in the season is on the NE slope of the basin (Table 3.3). During this time, the SW slope has less snow remaining to contribute to SWI, while the NE slopes that receive more precipitation and less solar radiation retain more SWE.

Complex SWI patterns shown on panels 7f and 7j warrant further discussion. Panel 7g is the SWI from the biweekly time period starting January 9, 2011. This time period is dominated by the large January ROS event (Table 3.2). Snow redistribution was not conducted during this time period because of warm dew point temperatures and the small percentage of snow that fell during storms. The high magnitude of SWI during

this biweekly period is the result of 77 mm of precipitation that fell during this time, 58 mm of which fell as rain. The SWI pattern on the SW slope is controlled by the initial distribution of SWE, virtually all of which melted during the event. Patterns on the NE slope are controlled by both the distribution of SWE and the distribution of energy balance terms. In contrast, panel 7j shows SWI from the biweekly time period starting on March 6, 2011. The difference between these time periods is that three snow events, totaling over 60 mm of precipitation, were redistributed during this time. This distribution caused variability in SWI over the basin. The SW slope had little snow at the beginning of this time and virtually no snow at the end of this time. All snow that fell on this slope melted by the end of this period. Although both slopes have approximately the same ΔQ by the end of this period, the NE slope had more snow to melt, leading to a higher total SWI magnitude (Table 3.3).

Four characteristic SWI periods progress with time in the rain-snow transition zone (Figure 3.8). The first SWI pattern, shown in panels 8a and 8b, show a near uniform pattern of SWI into the catchment, which results from: 1) early rain events (uniformly distributed), 2) early warm snow events that melt and do not develop into a snowpack, and 3) early cold snow events that develop into a snowpack, but do not begin to melt until later.

The second SWI pattern, shown in panels 8c through 8i, is dominated by topographic differences in energy fluxes that occur dominantly during the biweekly time periods starting on November 28, 2010 and February 20, 2011. These differences arise from topography related differences in the energy balance as described in the discussion of Figure 3.7. Other time periods in this range have relatively uniform SWI between

slopes and merely sustain the pattern developed in Figure 3.7c. These aspect related differences are described in detail for the early ablation periods observed at sites with more continuous snow cover (Pomeroy et al., 2003).

The third SWI pattern, depicted in panels 8j through 8k, is transitional. This time period still shows aspect differences related to the energy balance, but also incorporates the distribution of snow cover resulting from differential melt and precipitation distribution.

The fourth SWI pattern, shown in panels 8l through 8o, is controlled by the interaction between the distribution of snow over the catchment, higher sun angles, and warming conditions of spring. The combination of higher melt energy and SWE stored on NE slopes leads to the melt of all of the remaining snow on the northern aspects. All precipitation input to the basin (minus evaporation) enters the catchment soil system during this at this time.

ROS events produced similar SWI between the NE and SW slopes in the mountain rain-snow transition (Table 3.2). ROS SWI values are largely related to the amount of precipitation (Singh et al., 1997) and presence of snow cover. The snowpack was ripe preceding all five significant WY2011 ROS events, so there was no preferential retention of rain between slopes. The NE slope often has a larger magnitude of SWI for time periods preceding and following the events largely because there is more snow to melt on NE slopes (Table 3.2). The larger snow cover and magnitude of SWE on the NE slope lead to the 11 mm modeled difference in SWI between slopes for the March 15th ROS event.

Turbulent fluxes are responsible for the most SWI into the catchment during WY2011 ROS events (Table 3.2). They are also the dominant source of energy input to the snowpack during the first four of the five WY2011 ROS events. These events included the three largest ROS events that were responsible for over 10% of catchment SWI. Advective fluxes contribute significant (at least 17%) energy fluxes during the first two mid winter ROS events. Higher net all-wave radiation values for the NE slope in Table 3.2 are an artifact of deeper snow, greater SCA, and less wind exposure. Energy fluxes summarized in Table 3.2 are calculated only for snow-covered pixels.

Net radiation fluxes during the spring melt event account for about 80% of the melt energy (Table 3.2). This is in contrast to early ROS events where turbulent fluxes dominate the energy balance.

Implications of Model Forcing Assumptions

Simplifications made during the distribution of model forcings for the WY2011 at TL will affect the accuracy of modeled results. Air temperature and relative humidity are uniformly distributed across this small catchment with little impact on model results because variation of these parameters over a small area and limited elevation range as shown by Reba et al. (2011b) is negligible. The ground temperature is expected to vary with topography when the snowpack is shallow due to the interaction of incoming solar radiation, aspect, and snow cover. Although the importance of the magnitude of G has been widely studied (Knox et al., 2012; Marks and Dozier, 1992; Marks et al., 1998; Mazurkiewicz et al., 2008; Pomeroy et al., 1998; Sensoy et al., 2006), there has been little research done on the spatial distribution of this term. Soil temperature, from which soil heat flux (G) is calculated, has been uniformly distributed (Garen and Marks, 2005;

Susong et al., 1999; Winstral and Marks, 2002), or linearly distributed with elevation on larger scales (Marks et al., 2001). It would not be unreasonable to set near surface soil temperature to 0˚ C, as that is consistent with the snow temperature, and the temperature of the melt water and SWI from the snow. However, for this study, we uniformly distribute the measured soil temperature from the single soil temperature measurement site within the catchment. We assume that the impact of soil temperature on G is small when there is a continuous, deep snow cover. However, when the snow cover is thin or ephemeral the magnitude of G based on this measured value can be substantial. We acknowledge and accept this limitation to the modeling study, recognizing that the impact on SWE storage and SWI are minor. If we had more detailed information on soil temperature we would expect, as indicated by LaMontagne (2009), improved results.

Uniform wind speed distribution is a significant assumption and may have adverse affects on model results (Winstral and Marks, 2002; Winstral et al., 2009). This assumption disregards differences in turbulent fluxes associated with wind speed differences in response to vegetation and topography. Measured wind speeds from the WY2011 are generally low with a median value of 1.6 m/s and a 0.75 quantile value of 2.8 m/s. We did not distribute wind speeds because they are relatively low in magnitude compared to areas where empirical distribution models were developed. However, we expect that the simulation accuracy would be improved with full wind distribution methods.

Neglecting the influence of vegetation on incoming shortwave and longwave radiation will affect modeled SWE results. Vegetation affects from trees on radiation terms are expected to have a minimal affect on the overall basin SWE and SWI.

Although it has been shown that grasses and shrubs in deeper snow packs are quickly covered by snow and compressed within a few centimeters of the ground surface (Menard et al., 2012), it is likely that the relatively shallow snowpack allows for both the penetration of incoming solar radiation to warm this vegetation and contribute to melting, and for vegetation to protrude from the snow. Prunus subspecies, although taller than typical snow depth at the TL catchment, have small diameter stems with no leaves during the snow season and are observed to have minimal effects on snow accumulation and melt. Although we expect the influence of vegetation to be small, we recognize that it will have an influence on the snow dynamics. We expect that the model results would be improved by fully accounting for vegetation effects on the energy balance.

The simulation methods used in this study rely on the efficacy of the iSNOBAL model physics, the assumption that model forcings are correct, and that the precipitation distribution can be approximated from measured wind, precipitation, and temperature. The parameters of the empirical snow redistribution procedure presented were varied to obtain a reasonable fit between measured and modeled SWE. We recognize that this method may affect model results beyond the influence of wind. However, parameters used vary only slightly from those suggested in the literature (Winstral and Marks, 2002; Winstral et al., 2009; Winstral et al., 2013) (Table 3.1), which lead us to believe that our distribution methods effectively account for wind effects on snow redistribution. Choosing to distribute precipitation from wind during snowstorms rather than uniformly distributing wind corrected precipitation decreased the RMSE by approximately 50 mm of SWE.

The wind redistribution parameter set has implications on both the magnitude and distribution of precipitation during storms, which has cascading consequences for SWI differences between slopes and catchment mass balance studies (Figure 3.6 and Table 3.1). Distributing precipitation using wind during snowstorms, rather than uniformly distributing wind-corrected precipitation from the gauge, decreased the precipitation inputs by as much as 100 mm. A difference of 40 mm of basin average precipitation is possible depending on the wind distribution parameters used. The small range from 32 to 37 mm in the RMSE associated with parameter set choice substantiates the robustness of the wind redistribution model (Table 3.1). We recognize that our measurement dataset may not be sufficient to say what parameter set produces a precipitation data set that is closest to the actual distribution. Although this error is significant in the shallow snowpack of the rain-snow transition zone, it is a significant accomplishment when compared to the SWE accuracy requirement placed on the CoreH2O mission of 30 mm SWE or 10% of SWE (Rott et al., 2009; Rott et al., 2010).

The wind redistribution of precipitation during snow events led to a maximum of 90 mm difference in slope-averaged precipitation for the NE and SW slopes. Quantifying the spatial precipitation inputs to a catchment is critical to distributed catchment modeling. This is highlighted in the 70 mm difference in cumulative SWI between slopes by the end of WY2011, which is primarily a result of the precipitation distribution (Figure 3.6).

Conclusions

This study shows that it is possible to simulate the distribution of snow, melt energetics, and SWI over the dynamic and ephemeral snow cover in the rain-snow

transition zone. The snow and resulting SWI distributions are complex in this region. We show that northern aspects store more snow and have a more continuous snow cover than southern aspects. Mid winter SWI at TL occur more frequently on the SE slopes, while SWI on NE slopes is increased during spring. Four characteristic SWI periods occur at TL: 1) near uniform, 2) controlled by topographic differences in energy fluxes, 3) transitional, and 4) controlled by snow distribution. ROS events produce similar magnitudes of SWI between NE and SW slopes in TL. 12.5% of the total and 20% of the snow season SWI at TL in WY2011 result from ROS events. Turbulent fluxes dominate the energy balance during all but one of the ROS events documented. Net all-wave radiation fluxes dominate the energy balance during spring melt. Advective fluxes were greater than 17% of the energy balance during the first 2 ROS events. Distributing precipitation results in large decreases in modeled SWE errors. Different combinations of precipitation distribution parameters at TL result in a change of as much as 100 mm of total precipitation and a 90 mm difference between NE and SW slopes at TL for WY2011.

Acknowledgements

We thank Mark Seyfried for assisting in the preparation of this manuscript, Erik Boe for snow depth data, Pam Aishlin for field data collection and processing, Justin Huntington for soil profile installation, and Molly Gribb for soil texture analysis. We thank the students, faculty, and scientist at the Northwest Watershed Research Center and Boise State University Department of Geosciences for intellectual support. We thank the Northwest Watershed Research Center and Boise State University Department of Geosciences, Student Research Initiative, and Graduate College for funding support,

travel support, and general support. NASA EPSCoR and INRA provided funding for this project. The collection and processing of the data presented in this paper were funded in part by NSF-CBET (0854553, 08522), USDA-ARS CRIS Snow and Hydrologic Processes in the Intermountain West (5362-13610-008-00D), USDA-NRCS Water and Climate Center-Portland, Oregon (5362-13610-008-03R), NSF-EPS (0919514), and NOAA (NA08NWS4620047). Any reference to specific equipment types or manufacturers is for information purposes and does not represent a product endorsement or recommendation. Boise State University and the USDA ARS are equal opportunity employers.

References

Anderton, S.P., White, S.M., Alvera, B., 2004. Evaluation of spatial variability in snow water equivalent for a high mountain catchment. Hydrological Processes, 18(3): 435-453. doi: 10.1002/hyp.1319.

Austin, A. et al., 2004. Water pulses and biogeochemical cycles in arid and semiarid ecosystems. Oecologia, 141(2): 221-235. doi: 10.1007/s00442-004-1519-1.

Berris, S.N., Harr, R.D., 1987. Comparative snow accumulation and melt during rainfall in forested and clear-cut plots in the western cascades of oregon. Water Resources Research, 23(1): 135-142. doi: 10.1029/WR023i001p00135.

Cayan, D.R., Kammerdiener, S.A., Dettinger, M.D., Caprio, J.M., Peterson, D.H., 2001. Changes in the onset of spring in the western United States. Bulletin of the American Meteorological Society, 82(3): 399-415. doi: 10.1175/1520-0477(2001)082 <0399:citoos>2.3.co;2.

Colbeck, S.C., 1975. Theory for water-flow through a layered snowpack. Water Resources Research, 11(2): 261-266. doi: 10.1029/WR011i002p00261.

Conway, H., Raymond, C.F., 1993. Snow stability during rain. Journal of Glaciology, 39(133): 635-642. URL: <Go to ISI>://WOS:A1993NA69200022.

Dozier, J., 1980. A clear-sky spectral solar-radiation model for snow-covered mountainous terrain. Water Resources Research, 16(4): 709-718. doi: 10.1029/WR016i004p00709.

Dozier, J., Frew, J., 1981. Atmospheric corrections to satellite radiometric data over rugged terrain. Remote Sensing of Environment, 11(3): 191-205. doi: 10.1016/0034-4257(81)90019-5.

Dubayah, R.C., 1994. Modeling a solar-radiation topoclimatology for the Rio-Grande River Basin. Journal of Vegetation Science, 5(5): 627-640. URL: http://www.jstor.org/stable/3235879.

Eiriksson, D. et al., 2013. An evaluation of the hydrologic relevance of lateral flow in snow at hillslope and catchment scales. Hydrological Processes, 27(5): 640-654. doi: 10.1002/hyp.9666.

Elder, K., Dozier, J., Michaelsen, J., 1991. Snow accumulation and distribution in an alpine watershed. Water Resources Research, 27(7): 1541-1552. doi: 10.1029/91wr00506.

Erxleben, J., Elder, K., Davis, R., 2002. Comparison of spatial interpolation methods for estimating snow distribution in the Colorado Rocky Mountains. Hydrological Processes, 16(18): 3627-3649. doi: 10.1002/hyp.1239.

Feiccabrino, J., Lundberg, A., Gustafsson, D., 2012. Improving surface-based precipitation phase determination through air mass boundary identification. Hydrology Research, 43(3): 179-191. doi: 10.2166/nh.2012.060.

Garen, D.C., Marks, D., 2005. Spatially distributed energy balance snowmelt modelling in a mountainous river basin: estimation of meteorological inputs and verification of model results. Journal of Hydrology, 315(1-4): 126-153. doi: 10.1016/j.jhydrol.2005.03.026.

Gee, G.W., Hillel, D., 1988. Groundwater recharge in arid regions – review and critique of estimation methods. Hydrological Processes, 2(3): 255-266. doi: 10.1002/hyp.3360020306.

Golding, D.L., Swanson, R.H., 1986. Snow distribution patterns in clearings and adjacent forest. Water Resources Research, 22(13): 1931-1940.

Gutierrez-Jurado, H.A., Vivoni, E.R., 2013. Ecogeomorphic expressions of an aspect-controlled semiarid basin: II. Topographic and vegetation controls on solar irradiance. Ecohydrology, 6(1): 24-37. doi: 10.1002/eco.1263. doi: 10.1029/WR022i013p01931.

Hanson, C.L., Pierson, F.B., Johnson, G.L., 2004. Dual-gauge system for measuring precipitation: Historical development and use. Journal of Hydrologic Engineering, 9(5): 350-359. doi: 10.1061/(ASCE)1084-0699(2004)9:5(350).

Harr, R.D., 1986. Effects of clearcutting on rain-on-snow runoff in Western Oregon – A new look at old studies. Water Resources Research, 22(7): 1095-1100. doi: 10.1029/WR022i007p01095.

Hiemstra, C.A., Liston, G.E., Reiners, W.A., 2002. Snow redistribution by wind and interactions with vegetation at upper treeline in the Medicine Bow Mountains,

Wyoming, USA. Arctic Antarctic and Alpine Research, 34(3): 262-273. doi: 10.2307/1552483.

Hinckley, E.-L.S. et al., 2012. Aspect control of water movement on hillslopes near the rain–snow transition of the Colorado Front Range. Hydrological Processes. doi: 10.1002/hyp.9549.

Hock, R., 1999. A distributed temperature-index ice- and snowmelt model including potential direct solar radiation. Journal of Glaciology, 45(149): 101-111. URL: <Go to ISI>://WOS:000080138700012.

Ivanov, V.Y., Bras, R.L., Vivoni, E.R., 2008. Vegetation-hydrology dynamics in complex terrain of semiarid areas: 1. A mechanistic approach to modeling dynamic feedbacks. Water Resources Research, 44(3): 34. doi: W03429 10.1029/2006wr005588.

Jost, G., Moore, R.D., Weiler, M., Gluns, D.R., Alila, Y., 2009. Use of distributed snow measurements to test and improve a snowmelt model for predicting the effect of forest clear-cutting. Journal of Hydrology, 376(1-2): 94-106. doi: 10.1016/j.jhydrol.2009.07.017.

Jost, G., Weiler, M., Gluns, D.R., Alila, Y., 2007. The influence of forest and topography on snow accumulation and melt at the watershed-scale. Journal of Hydrology, 347(1-2): 101-115. doi: 10.1016/j.jhydrot.2007.09.006.

Kattelmann, 1996. Flooding from rain-on-snow events in the Sierra Nevada. In: Leavesley, G.H.L., Harry F.Nobilis, FranzParker, Randolph S.Schneider, Verne R.van de Ven, Frans H. M. (Ed.), Destructive Water: Water-Caused Natural Disasters—Their Abatement and Control. Red Books. IAHS, Anaheim, California, pp. 59-65.

Knox, S.H., Carey, S.K., Humphreys, E.R., 2012. Snow surface energy exchanges and snowmelt in a shrub-covered bog in eastern Ontario, Canada. Hydrological Processes, 26(12): 1877-1891. doi: 10.1002/hyp.9289.

Kormos, P.R. et al., 2013. Soil, Snow, Weather, and Sub-surface Storage Data from a Mountain Catchment in the Rain-Snow Transition Zone. Earth System Science Data, in review.

Krajewski, W.F., Lakshmi, V., Georgakakos, K.P., Jain, S.C., 1991. A Monte Carlo Study of rainfall sampling effect on a distributed catchment model. Water Resources Research, 27(1): 119-128. doi: 10.1029/90WR01977.

Kumar, M., Marks, D., Dozier, J., Reba, M., Winstral, A., 2013. Evaluation of distributed hydrologic impacts of temperature-index and energy-based snow models. Advances in Water Resources, 56: 77-89. doi: 10.1016/j.advwatres.2013.03.006.

LaMontagne, A., 2009. Characterization and quantification of ground heat flux for late season shallow snow, Boise State University, Boise, ID, 69 pp. URL: http://scholarworks.boisestate.edu/td/48/.

Link, T.E., Marks, D., 1999. Point simulation of seasonal snow cover dynamics beneath boreal forest canopies. Journal of Geophysical Research-Atmospheres, 104(D22): 27841-27857. doi: 10.1029/1998JD200121.

Link, T.E., Marks, D., Hardy, J.P., 2004. A deterministic method to characterize canopy radiative transfer properties. Hydrological Processes, 18(18): 3583-3594. doi: 10.1002/hyp.5793.

Liston, G.E., 1995. Local advection of momentum, heat, and moisture during the melt of patchy snow covers. Journal of Applied Meteorology, 34(7): 1705-1715. doi: 10.1175/1520-0450-34.7.1705.

Liston, G.E., Elder, K., 2006. A distributed snow-evolution modeling system (SnowModel). Journal of Hydrometeorology, 7(6): 1259-1276. doi: 10.1175/jhm548.1.

Luce, C.H., Tarboton, D.G., Cooley, R.R., 1998. The influence of the spatial distribution of snow on basin-averaged snowmelt. Hydrological Processes, 12(10-11): 1671-1683. doi: 10.1002/(sici)1099-1085(199808/09)12:10/11<1671::aid-hyp688>3.0.co;2-n.

Marks, D., Domingo, J., Susong, D., Link, T., Garen, D., 1999. A spatially distributed energy balance snowmelt model for application in mountain basins. Hydrological Processes, 13(12-13): 1935-1959. doi: 10.1002/(SICI)1099-1085(199909)13:12/13<1935::AID-HYP868>3.0.CO;2-C.

Marks, D., Dozier, J., 1979. Clear-sky longwave radiation model for remote alpine areas. Archiv Fur Meteorologie Geophysik Und Bioklimatologie Serie B-Klimatologie Umweltmeteorologie Strahlungsforschung, 27(2-3): 159-187. ISSN: 0376-1622.

Marks, D., Dozier, J., 1992. Climate and energy exchange at the snow surface in the alpine region of the sierra-nevada .2. Snow cover energy-balance. Water Resources Research, 28(11): 3043-3054. doi: 10.1029/92wr01483.

Marks, D., Kimball, J., Tingey, D., Link, T., 1998. The sensitivity of snowmelt processes to climate conditions and forest cover during rain-on-snow: a case study of the 1996 Pacific Northwest flood. Hydrological Processes, 12(10-11): 1569-1587. URL: <Go to ISI>://000075740100006.

Marks, D., Link, T., Winstral, A., Garen, D., 2001. Simulating snowmelt processes during rain-on-snow over a semi-arid mountain basin. In: Hutter, K. (Ed.), Annals of Glaciology, Vol 32, 2001. Annals of Glaciology. Int Glaciological Soc, Cambridge, pp. 195-202. URL: <Go to ISI>://000171277900033.

Marks, D., Winstral, A., 2001. Comparison of snow deposition, the snow cover energy balance, and snowmelt at two sites in a semiarid mountain basin. Journal of Hydrometeorology, 2(3): 213-227. doi: 10.1175/1525-7541(2001)002<0213:cosdts>2.0.co;2.

Marks, D., Winstral, A., Reba, M., Pomeroy, J., Kumar, M., 2013. An evaluation of methods for determining during-storm precipitationphase and the rain/snow transition elevation at the surface in amountain basin. Advances in Water Resources, in press.

Marks, D., Winstral, A., Seyfried, M., 2002. Simulation of terrain and forest shelter effects on patterns of snow deposition, snowmelt and runoff over a semi-arid mountain catchment, pp. 3605-3626. doi: 10.1002/hyp.1237.

Marshall, S., Warren, S., 1987. Parameterization of snow albedo for climate models, large scale effects of seasonal snow cover. Proceedings of an International Symposium held August 9-22, 1987, Vancouver, British Columbia, Canada, pp. 43-50.

Mazurkiewicz, A.B., Callery, D.G., McDonnell, J.J., 2008. Assessing the controls of the snow energy balance and water available for runoff in a rain-on-snow environment. Journal of Hydrology, 354(1-4): 1-14. doi: 10.1016/j.jhydrol.2007.12.027.

McCabe, G.J., Clark, M.P., Hay, L.E., 2007. Rain-on-snow events in the western United States. Bulletin of the American Meteorological Society, 88(3): 319-328. doi: 10.1175/bams-88-3-319.

Menard, C.B.E., R.Pomeroy, J.Marsh, P.Clark, D. B., 2012. A shrub bending model to calculate the albedo of shrub-tundra. Hydrological Processes. doi: 10.1002/hyp.9582.

Molotch, N.P. et al., 2009. Ecohydrological controls on snowmelt partitioning in mixed-conifer sub-alpine forests. Ecohydrology, 2(2): 129-142. doi: 10.1002/eco.48.

Moore, I.D., Grayson, R.B., Ladson, A.R., 1991. Digital terrain modeling - a review of hydrological, geomophological, and biological applications. Hydrological Processes, 5(1): 3-30. doi: 10.1002/hyp.3360050103.

Nolin, A.W., Daly, C., 2006. Mapping "at risk" snow in the Pacific Northwest. Journal of Hydrometeorology, 7(5): 1164-1171. doi: 10.1175/jhm543.1.

Pellicciotti, F. et al., 2005. An enhanced temperature-index glacier melt model including the shortwave radiation balance: development and testing for Haut Glacier d'Arolla, Switzerland. Journal of Glaciology, 51(175): 573-587. doi: 10.3189/172756505781829124.

Pomeroy, J.W., Gray, D.M., Hedstrom, N.R., Janowicz, J.R., 2002. Prediction of seasonal snow accumulation in cold climate forests. Hydrological Processes, 16(18): 3543-3558. doi: 10.1002/hyp.1228.

Pomeroy, J.W. et al., 1998. An evaluation of snow accumulation and ablation processes for land surface modelling. Hydrological Processes, 12(15): 2339-2367. doi: 10.1002/(sici)1099-1085(199812)12:15<2339::aid-hyp800>3.0.co;2-l.

Pomeroy, J.W. et al., 2009. The impact of coniferous forest temperature on incoming longwave radiation to melting snow. Hydrological Processes, 23(17): 2513-2525. doi: 10.1002/hyp.7325.

Pomeroy, J.W., Toth, B., Granger, R.J., Hedstrom, N.R., Essery, R.L.H., 2003. Variation in surface energetics during snowmelt in a subarctic mountain catchment. Journal of Hydrometeorology, 4(4): 702-719. doi: 10.1175/1525-7541(2003) 004<0702:viseds>2.0.co;2.

Price, A.G., Dunne, T., 1976. Energy-balance computations of snowmelt in a subarctic area. Water Resources Research, 12(4): 686-694. doi: 10.1029/WR012i004p00686.

Reba, M.L. et al., 2011a. A long-term data set for hydrologic modeling in a snow-dominated mountain catchment. Water Resources Research, 47(7). doi: 10.1029/2010wr010030.

Reba, M.L., Marks, D., Winstral, A., Link, T.E., Kumar, M., 2011b. Sensitivity of the snowcover energetics in a mountain basin to variations in climate. Hydrological Processes, 25(21): 3312-3321. doi: 10.1002/hyp.8155.

Rott, H. et al., 2009. ESA SP-1313/3 candidate earth explorer core missions report for assessment: CoReH20—Cold regions hydrology high resolution observatory. In: Office, E.C.P. (Ed.), pp. 114.

Rott, H. et al., 2010. Cold regions hydrology high-resolution observatory for snow and cold landprocesses. Proceedings of the IEEE, 98(5): 752-765. URL: http://ieeexplore.ieee.org/xpls/abs_all.jsp?arnumber=5420000&tag=1,

Scanlon, B.R. et al., 2006. Global synthesis of groundwater recharge in semiarid and arid regions. Hydrological Processes, 20(15): 3335-3370. doi: 10.1002/hyp.6335.

Schmidt, S.K., Lipson, D.A., 2004. Microbial growth under the snow: Implications for nutrient and allelochemical availability in temperate soils. Plant and Soil, 259(1-2): 1-7. doi: 10.1023/B:PLSO.0000020933.32473.7e.

Sensoy, A., Sorman, A.A., Tekeli, A.E., Sorman, A.U., Garen, D.C., 2006. Point-scale energy and mass balance snowpack simulations in the upper Karasu basin, Turkey. Hydrological Processes, 20(4): 899-922. doi: 10.1002/hyp.6120.

Seyfried, M., Chandler, D., Marks, D., 2011. Long-term soil water trends across a 1000-m elevation gradient. Vadose Zone Journal, 10(4): 1276-1286. doi: 10.2136/vzj2011.0014.

Seyfried, M.S., Grant, L.E., Marks, D., Winstral, A., McNamara, J., 2009. Simulated soil water storage effects on streamflow generation in a mountainous snowmelt environment, Idaho, USA. Hydrological Processes, 23(6): 858-873. doi: 10.1002/hyp.7211.

Shallcross, A.T., 2012. LiDAR Investigations of snow distribution in mountainous terrain, Boise State University, Boise, ID, 62 pp. URL: http://scholarworks.boisestate.edu/td/349/.

Singh, P., Spitzbart, G., Hubl, H., Weinmeister, H.W., 1997. Hydrological response of snowpack under rain-on-snow events: a field study. Journal of Hydrology, 202(1-4): 1-20. doi: 10.1016/s0022-1694(97)00004-8.

Sui, J., Koehler, G., 2001. Rain-on-snow induced flood events in Southern Germany. Journal of Hydrology, 252(1-4): 205-220. doi: 10.1016/s0022-1694(01)00460-7.

Surfleet, C.G., Tullos, D., 2013. Variability in effect of climate change on rain-on-snow peak flow events in a temperate climate. Journal of Hydrology, 479(0): 24-34. doi: 10.1016/j.jhydrol.2012.11.021.

Susong, D., Marks, D., Garen, D., 1999. Methods for developing time-series climate surfaces to drive topographically distributed energy- and water-balance models. Hydrological Processes, 13(12-13): 2003-2021. doi: 10.1002/(SICI)1099-1085(199909)13:12/13<2003::AID-HYP884>3.0.CO;2-K.

Walter, M.T. et al., 2005. Process-based snowmelt modeling: does it require more input data than temperature-index modeling? Journal of Hydrology, 300(1-4): 65-75. doi: 10.1016/j.jhydro.2004.05.002.

Warren, S.G., Wiscombe, W.J., 1980. A model for the spectral albedo of snow .2. Snow containing atmospheric aerosols. Journal of the Atmospheric Sciences, 37(12): 2734-2745. ISSN: 0022-4928.

Wigmosta, M.S., Vail, L.W., Lettenmaier, D.P., 1994. A distributed hydrology-vegetation model for complex terrain. Water Resources Research, 30(6): 1665-1679. doi: 10.1029/94wr00436.

Williams, C.J., McNamara, J.P., Chandler, D.G., 2009. Controls on the temporal and spatial variability of soil moisture in a mountainous landscape: the signature of snow and complex terrain. Hydrology and Earth System Sciences, 13(7): 1325-1336. doi: 10.5194/hess-13-1325-2009.

Winstral, A., Marks, D., 2002. Simulating wind fields and snow redistribution using terrain-based parameters to model snow accumulation and melt over a semi-arid mountain catchment, pp. 3585-3603. doi: 10.1002/hyp.1238.

Winstral, A., Marks, D., Gurney, R., 2009. An efficient method for distributing wind speeds over heterogeneous terrain. Hydrological Processes, 23(17): 2526-2535. doi: 10.1002/hyp.7141.

Winstral, A., Marks, D., Gurney, R., 2013. Simulating wind-affected snow accumulations at catchment to basin scales. Advances in Water Resources, 55: 64-79. doi: 10.1016/j.advwatres.2012.08.011.

Wiscombe, W.J., Warren, S.G., 1980. A model for the spectral albedo of snow .1. Pure snow. Journal of the Atmospheric Sciences, 37(12): 2712-2733. ISSN: 0022-4928.

CHAPTER FOUR: DEEP PERCOLATION ESTIMATES FROM THE MOUNTAIN RAIN SNOW TRANSITION ZONE

Authors

Patrick R. Kormos[1]

James P. McNamara[1]

Mark Seyfried[2]

Hans Peter Marshall[1]

Alejandro Flores[1]

Danny Marks[2]

1. Department of Geosciences, Boise State University

2. Northwest Watershed Research Center, Agricultural Research Service

Abstract

The timing and magnitude of deep percolation is estimated from a catchment in the rain snow transition zone. A combination of measured stream discharge and modeled soil drainage are utilized to conduct a mass balance at the soil bedrock interface. Deep percolation is estimated to be 311 mm ± 48 mm for the 2011 water year, which is 36% ±6% of the precipitation (68% confidence). Soils on the southwest facing slope drain more often throughout the snow season, but the northeast facing slope contributes a greater total magnitude of soil drainage. Peaks in catchment soil drainage and deep percolation coincide with rain on snow events. We utilize modeling methods that focus on achieving a good fit between measured and modeled soil water storage. Estimates of deep percolation from mountain catchments in the western U.S. are essential to water resource managers because they estimate mountain block recharge to regional aquifers. On smaller scales, deep percolation is an important term in water mass balance studies, which attempt to estimate hydrologic states and fluxes in watersheds with fractured or transmissive bedrock.

Introduction

Deep percolation (DP) from mountain catchments, defined as water that leaves the catchment boundaries through subsurface drainage, can be an important component of the catchment water balance (Flerchinger and Cooley, 2000, Bayard et al., 2005, Kelleners et al., 2010, Makurira et al., 2010, Selle et al., 2011, and Han et al., 2012). However, catchment mass balance studies often consider DP negligible and could be improved by estimating DP magnitudes (Wilson and Guan, 2004, Tromp-van Meerveld et al., 2007, Graham et al., 2010a, Teuling et al., 2010, and Bales et al., 2011). DP is

important not only from the catchment perspective, but also from the groundwater perspective; catchment DP is a component of mountain block recharge (Thoma et al., 2011). Mountain catchments in the western U.S. are important sources of regional aquifer recharge (Hogan et al., 2004). For example, most of the groundwater recharge in the Great Basin region occurs in the mountainous divides between basins (Hevesi et al., 2003, Flint et al., 2004 and Scanlon et al., 2006).

DP is controlled by a combination of the water delivery to the soil bedrock interface and the transmissive properties of the bedrock. The amount and timing of soil water drainage to the bedrock is a function of the water delivery to the soil surface, soil water storage, physical properties of the soil, and evapotranspiration (ET). All of these properties and processes are complex and vary in time and/or space.

Methods to quantify DP (*see* Sammis et al., 1982) include estimates from detailed mass balance studies of water or conservative solutes (Aishlin and McNamara., 2011 and Graham et al., 2010a), numerical modeling at a lower soil boundary (Kelleners et al., 2009, Guan et al., 2010, Kelleners et al., 2010, Dijksma et al., 2011 and Wang et al., 2011), and direct measurements from caves (Taucer et al., 2008 and Sheffer et al., 2011). Direct measurements are valuable, but the diffuse and inaccessible location of DP occurrence makes them extremely difficult and rarely possible. Water and solute balance approaches can yield estimates of annual magnitudes of DP, but are not generally capable of assessing the timing of DP. Solute balance approaches also require multiple years of data to overcome inherent assumptions, and even then may only be correct when averaging over the period of record (Wood, 1999 and Aishlin and McNamara, 2011). Mass balance approaches calculate DP as a residual, which includes the additive errors of

all other mass balance components. It is essential that these approaches include an uncertainty analysis. Physically based hydrologic modeling of DP is hindered by a general lack of knowledge of the transmissive properties of underlying bedrock, which makes model parameterization challenging. At regional scales, global and standardized data sets are often used parameterize models to estimate DP so results from different models can be objectively compared (Nolan et al., 2007, Sutanudjaja et al., 2011, and Sorensen et al., 2013). These data sets make model parameterization convenient, but make it difficult to incorporate local knowledge to improve model results.

Storage-discharge relationships (*e.g.* Brutsaert and Nieber, 1977, and Kirchner, 2009) have also been used to assess mountain block recharge (Ajami et al., 2011). This approach recognizes that changes in groundwater storage are related to both streamflow and recharge. Therefore, recharge can be assessed by evaluating stream discharge. Inherent in this approach is the assumption that streamflow incorporates all drainage from catchment groundwater storage. In "leaky" catchments, however, streamflow does not represent all drainage. Rather, drainage is the sum of streamflow and DP. When DP is significant, traditional storage-discharge methods are not appropriate.

While many studies have estimated the magnitude of annual DP (Ragab et al., 1997, Simmers, 1997, Van Der Lee and Gehrels, 1997, Maxwell, 2010, and Jie et al., 2011), few studies have estimated the timing of DP on sub annual timescales. Knowledge of the timing and magnitude of DP in response to hydrologic events throughout a year is important to water resource managers, land managers, as well as catchment hydrologists. For example, if spring snowmelt events are known to contribute to large amounts of DP, we could receive less streamflow and more groundwater

recharge during those events. Or, if DP occurs at a steady rate throughout the year, there could be a threshold of melt water production that would be expected to produce streamflow in catchments with ephemeral streams.

Other hydrologic events of interest are rain on snow (ROS) events. Although ROS events are known to generate large amounts of snowmelt, there is a general lack of knowledge about how much *DP* they produce. It is also of interest to know how much ROS events contribute to annual *DP*. We define the beginning of a ROS event as the onset of atmospheric conditions associated with a rain event, which includes increased air temperatures, wind speeds, and humidity. The ROS event then extends through the hydrograph recession associated with that event.

The climatically sensitive rain-snow transition zones of the mountainous western US are inherently susceptible to ROS events because the phase of precipitation that falls here is transitional and varies throughout the winter. We define the mountain rain-snow transition zone as the elevation zone where the dominant winter precipitation phase changes from rain at lower elevations to snow at higher elevations. The elevation of this zone varies from sea level at high latitudes (Feiccabrino et al., 2012) to over 2000 m at lower latitudes (Cayan et al., 2001). This zone typically occurs between 1500 m and 1800 m in the interior Pacific Northwestern U.S. and covers approximately 9200 km^2 (Nolin and Daly, 2006).

The dominant phase of precipitation in the rain-snow transition zone is expected to change from snow to rain as climate warming trends continue (Cuo et al., 2011). The change in snow cover and air temperature will likely affect surface water input (SWI) timing and patterns, and the timing of spring green up. SWI is defined as the water

entering the soil surface resulting from rain or snow melt. Variations in plant activity can alter ET patterns. The dynamics of DP are therefore expected to change, since DP is a function of both SWI and ET.

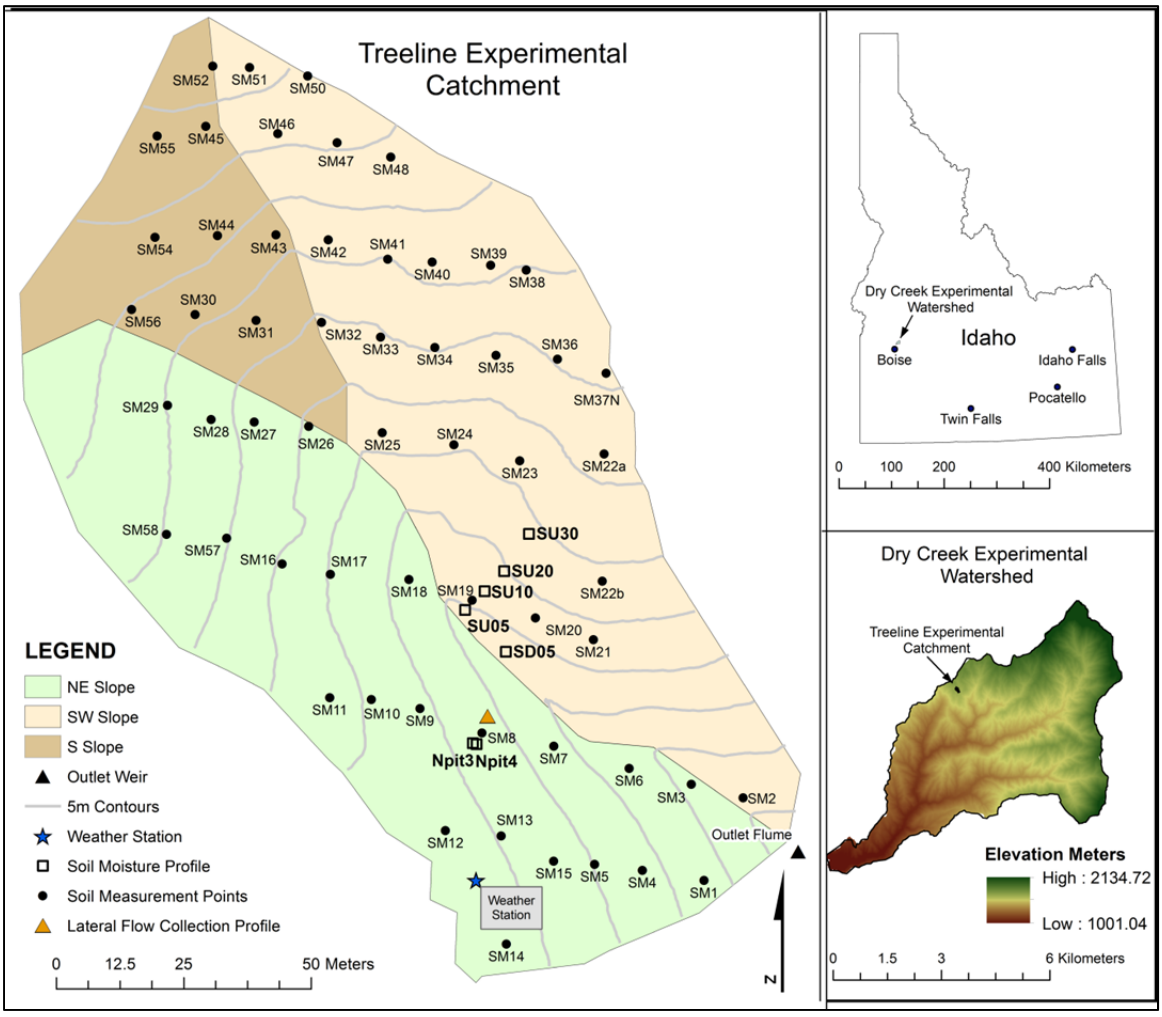

Figure 4.1 Location map of Tree Line catchment showing location of snow depth sensors, weather station, flume, and soil pits.

The goal of this study is to quantify the magnitude of DP in a semiarid mountain catchment in the rain-snow transition zone north of Boise, Idaho, USA (**Figure 4.1**). We investigate DP in a thin-soiled mountain catchment with an ephemeral stream, by employing a water balance approach at the soil bedrock interface. This method assumes that flow at the interface is partitioned laterally into streamflow and vertically into DP.

Estimating DP is then a matter of measuring streamflow and estimating flow to the soil bedrock interface. The latter requires hydrologic modeling to bypass the insurmountable difficulties of measuring basin wide soil drainage.

A modeling approach is employed where the most salient hydrologic processes and properties of the catchment are represented (Zhang et al., 2008, Bartolini et al., 2011, Papalexiou et al., 2011, and Zanardo et al., 2012). The choice of hydrologic models relies on site-specific knowledge of both the hydrologic processes that must be faithfully represented, as well as those that can be simplified. Previous work in the study site, the Dry Creek Experimental Watershed (DCEW), has demonstrated the following principles that have guided our model development: (1) snow accumulation and melt patterns are highly variable in time and space (Kormos et al., 2013a and Shalcross, 2012), (2) spatial variability of soil moisture is correlated with the spatial variability of snow cover and snow melt (Williams et al., 2009), (3) lateral flow in the unsaturated soil column is negligible (McNamara et al., 2005 and Abdelmasih, 2006), (4) spatial and temporal patterns in hillslope soil moisture are related to intermittent streamflow (McNamara et al., 2005), and (5) streamflow in upland ephemeral streams is disconnected from deep, regional groundwater (Miller et al., 2008). We also recognize that catchment storage is central to hydrological processes on all scales and is becoming increasingly recognized as an important control on water flux thresholds, slope connectivity, and residence times (Spence, 2007, Kirchner, 2009, Spence et al., 2010, and McNamara et al., 2011).

Distributed snow and soil water storage are, to some degree, easier to measure than distributed water fluxes (SWI and soil drainage to the bedrock surface). We therefore present a combined measurement and modeling study that focuses on catchment

water storage in snow and soil reservoirs within the study catchment. In doing so, we rely on the basic principal that if storage dynamics are modeled accurately, fluxes will likewise be accurate (McNamara et al., 2011). We use distributed point measurements of snow depth and density, and soil moisture to evaluate modeled snow and soil storage results. This eliminates the need for calibrating to streamflow, but suffers from the problem that the flux of interest, DP, cannot be used for calibration as coincident validation data for DP are not available. Fortunately, other studies have estimated DP in the highly instrumented Treeline catchment (TL) (previously referred to as Upper Dry Creek) of DCEW using a variety of methods. It has been estimated that TL looses between 17% and 44% of annual (wind-corrected) precipitation to DP using a chloride mass balance approach for 2005 through 2009 (Aishlin and McNamara, 2011). Kelleners et al. (2010) arrived at a similar conclusion (34-36% of measured shielded precipitation) by applying a physically based model of the catchment. In the latter study, DP was represented with a Darcian equation and a calibration objective function used a combination of soil moisture and streamflow to get an optimized vertical saturated hydraulic conductivity of the bedrock. The current study builds upon previous work in the catchment by accounting for wind redistribution of snow and better quantifying uncertainty in DP estimates. We also avoid the difficulties of parameterizing a complex, physically based watershed model. A time series of distributed SWI for the 2011 water year (WY2011) is obtained from Kormos et al. (2013a). This paper addresses the following questions: 1) How much *DP* occurs in a rain-snow transition zone catchment, 2) What are the relative contributions of ROS and spring melt events to total annual DP

compared to non-event contributions, and 3) What is the uncertainty in the DP estimate using this approach?

Study Site

TL is an intensively instrumented 1.5 hectare catchment within the DCEW in the semiarid foothills north of Boise, ID (**Figure 4.1**) (McNamara et al., 2005, Kelleners et al., 2009, Stratton et al., 2009, Williams et al., 2009, and Kelleners et al., 2010). The catchment is defined by the location of a v-notch weir. TL ranges in elevation from 1600 m to 1645 m, which situates it in the current rain snow transition zone. It is dominated by northeast (NE) and southwest (SW) facing slopes. The catchment is underlain by fractured granitic bedrock (Gribb et al., 2009). Thin sandy soils range in thickness from 20 cm to 125 cm and average 48 cm (Williams et al., 2009). Soils are underlain by up to 100 cm of saprolite. Wet season conductive anomalies identified from an electrical resistivity tomography survey suggest water percolation through bedrock fractures (Miller et al., 2008). That survey and the intermittent behavior of the stream suggest a lack of connection between the stream and the regional groundwater storage reservoir. Vegetation is typical of a transition between lower elevation grasslands and higher elevation forests. The NE slope is typified by sagebrush and *ceanothus* shrubs, *prunus* subspecies, forbs, and grasses. SW slopes are sparser and contain mostly grasses, forbs, and sagebrush. There are 8 mature conifer trees in the catchment that are assumed to have negligible influence on the hydrology for the purpose of this study.

The TL weather station has been operational since 1998. The average annual measured precipitation at the shielded gauge is approximately 670 mm with a mean annual temperature of 9˚C. This study focuses on WY2011, which received above

average precipitation totaling 855 mm measured at the shielded gauge, of which 43% of fell as snow, 49% fell as rain, and 8% fell as mixed events. The catchment experienced 2 major and 5 minor ROS events in WY2011. The 2011 snowpack was highly variable in time and space due predominantly to aspect differences in energy balance terms and wind redistribution of precipitation during snow storms (Kormos et al., 2013a and Kormos et al., 2013b). The mean WY2011 air temperature was cooler than average with a mean of 7.4˚C.

Methods

An annual water balance approach is taken to estimate deep percolation (DP) for WY2011 using:

$$DP_{tot} = SWI_{tot} - ET_{tot} - Q_{stot} \quad (1)$$

where DP_{tot}, SWI_{tot}, ET_{tot}, and Q_{stot} are the annual totals of DP, surface water input (SWI), evapotranspiration (ET), and streamflow (Q_s). Since we apply a hydrologic model that integrates SWI gains and calculates ET losses to yield soil drainage to the soil bedrock interface (Dr), we simplify Equation 1 using:

$$Dr_{tot} = SWI_{tot} - ET_{tot} \quad (2)$$

to result in:

$$DP_{tot} = Dr_{tot} - Q_{stot} \quad (3)$$

where Dr_{tot} is the annual total Dr. These equations assume that the change in soil water storage is negligible from the beginning to the end of the water year, which is commonly observed at this study site and similar environments (Seyfried and Wilcox,

2006, Seyfried et al. 2005, McNamara et al., 2005 and Campbell and Harris, 1977) (**Figure 4.2**). A daily water balance approach is performed at the bottom of the soil column to calculate the timing of DP for WY2011:

$$DP_t = Dr_t - Q_{st} \tag{4}$$

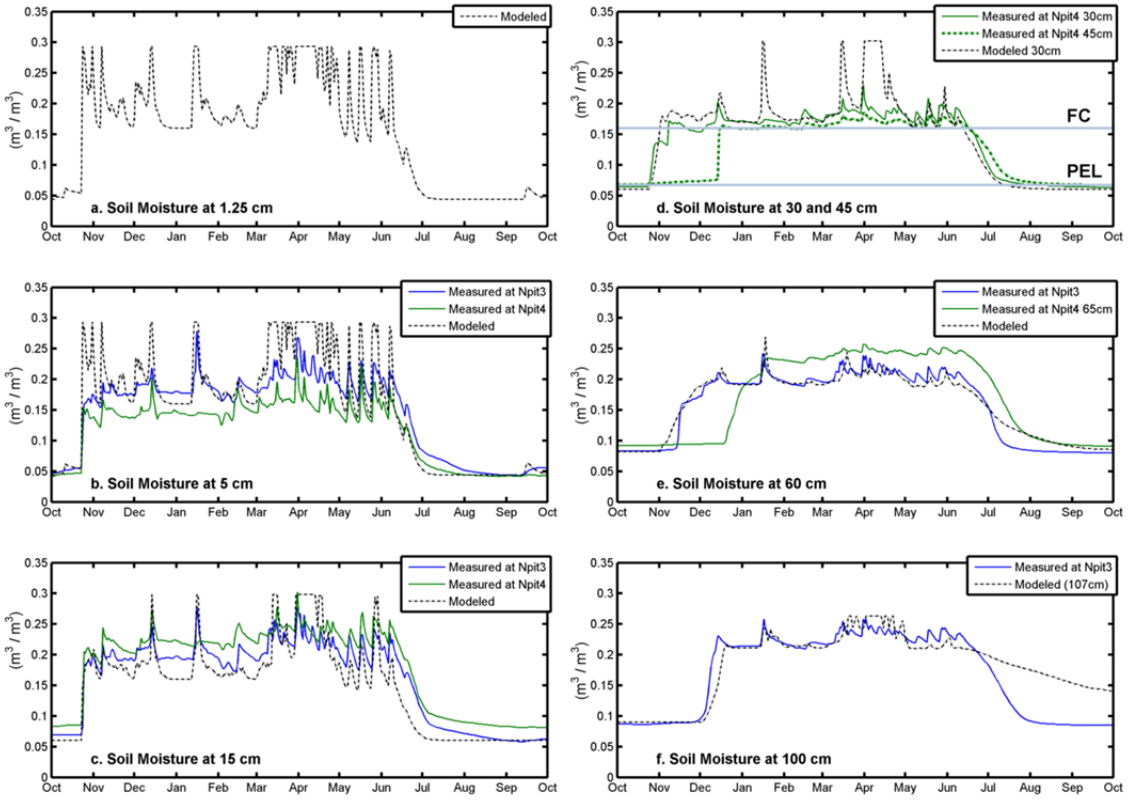

Figure 4.2 Measured soil moisture from the NE slope including modeled results SEM8. Horizontal lines show the empirical values of FC and PEL parameters.

where DP_t, Dr_t, and Q_{st} are the DP, Dr, and Q_s at each time step t. This approach assumes that Dr is quickly routed either laterally to the stream, or vertically to DP.

DP from an event is obtained by integrating Equation 4 over the event time period. Q_{stot} and Q_s are obtained by hourly stream discharge measurements at the catchment outlet weir. Dr_{tot} and Dr_t are modeled because of the aforementioned measurement difficulties.

Model Approach

We use a storage-centric modeling approach similar to Seyfried et al. (2009), which models SWI and soil drainage separately. Separating these two hydrologic fluxes allows for using different models with appropriate complexities.

Highly variable snow storage and SWI patterns at the study site require the use of a distributed, physically based energy balance snow model. We use the iSNOBAL model to calculate snow cover distribution and SWI estimates (Marks and Dozier, 1992 and Marks et al., 1999). Details of the iSNOBAL derived SWI time series used as the surface flux (Neumann boundary condition) to the soil surface layer can be found in Kormos et al. (2013a). This study accounted for wind redistribution of snow, albedo decay from late season litter accumulation, and partial snow cover.

Requirements for the watershed processing model were the need take calculated SWI as input and to calculate soil moisture storage, drainage, and losses to ET. We chose to distribute the Soil Ecohydraulic Model (SEM), a one-dimensional, soil capacitance based soil water model to estimate the catchment soil water storage, drainage, and losses to ET. SEM was an attractive model choice because it requires relatively few, tangible parameters, and daily values of commonly measured weather variables. This is in contrast to Richard's equation-based models that require a comprehensive knowledge of highly variable soil properties, such as hydraulic conductivity. Capacitance-based models rely on the concept that soils have a field capacity (*FC*), or a soil moisture content threshold where drainage due to gravity becomes negligible. The value of *FC* is subjective because soils continue to drain indefinitely, albeit with and ever-declining rate. This type of model is appropriate for our

study site because: 1) the coarse-textured soils initially drain rapidly and quickly slow due to the relatively steep decrease in hydraulic conductivity with increasing matric suction (Hillel, 1998 and Geroy et al., 2011), 2) water input events occur frequently enough throughout the late fall-winter-early spring season that soil water contents rarely drain to or below *FC* (**Figure 4.2**) (Kormos et al. 2013a and McNamara et al., 2005), and 3) continuous soil moisture measurements are available across representative aspects and soil depths to estimate *FC in situ*.

iSNOBAL was run at an hourly time step on a 2.5 m^2 grid. This resulted in the hourly, distributed SWI to the catchment required to run the SEM model across the catchment. SEM was run at a daily time step at 57 points across the watershed where soil depths and soil surface textures were measured. Modeled SWI output was therefore averaged spatially and accumulated temporally to be used to force SEM. To do this, the watershed was first divided into dominant slopes (**Figure 4.3**). The SW slope was divided into two dominant slopes so the differences in snow characteristics could be better translated to SEM polygons (**Figure 4.1**). This division is only used to create SEM domains and all results are grouped by NE and SW slopes. Thiessen polygons were then created within each slope to assign each of the 57 points a catchment area. All pixels within each polygon were then averaged for each hourly time step and accumulated by day as input to SEM.

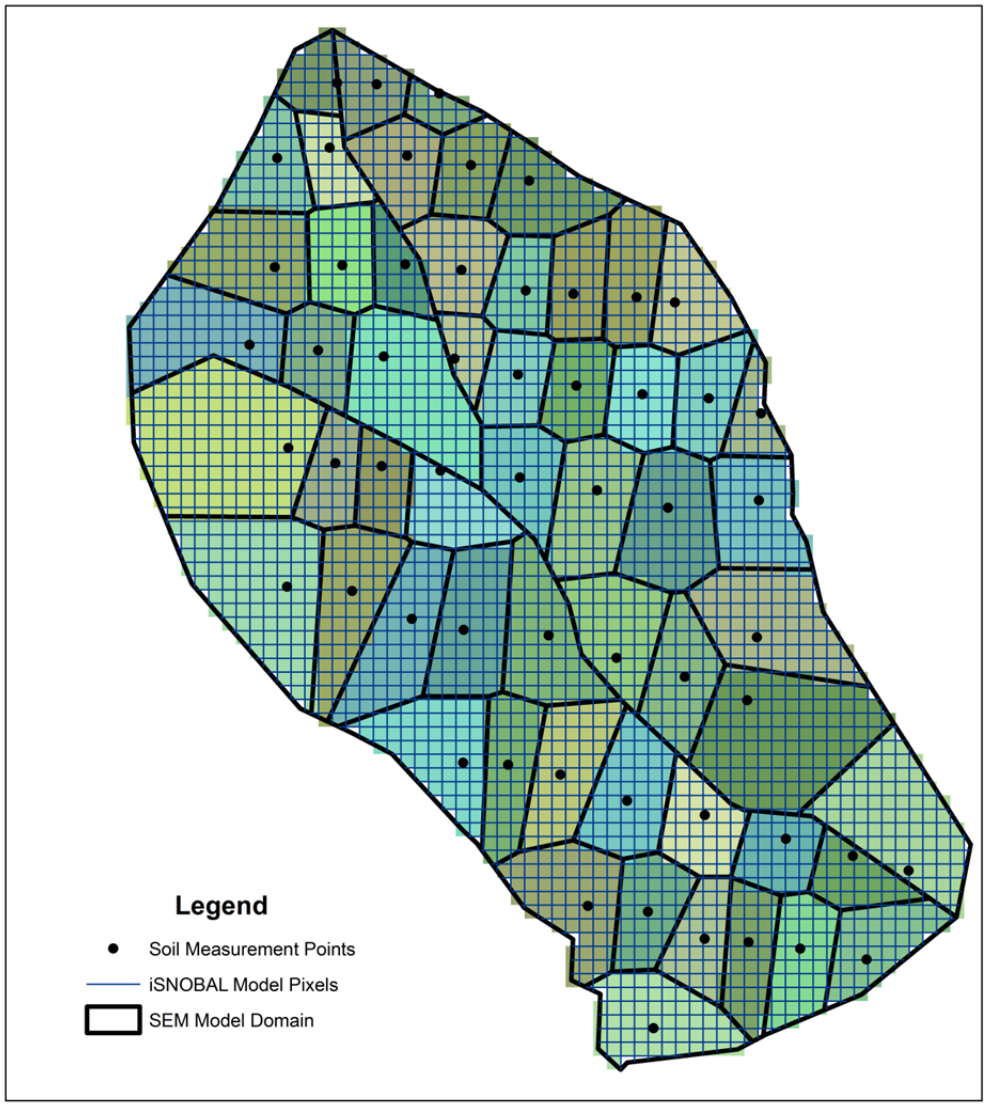

Figure 4.3 Schematic of the spatial distribution of iSNOBAL model pixels versus the Theissen polygons where SEM was run. SWI from iSNOBAL pixels are summed over the SEM daily time step and then averaged to get a daily snow water input to the 57 SEM polygons.

DP was then calculated on the basin scale as the difference between modeled whole-catchment Dr and measured catchment streamflow. Point model estimates of drainage to the soil bedrock interface therefore need to be upscaled to represent whole-catchment Dr. We multiplied the modeled output Dr from each model point by the respective area of the polygon to get a volume of Dr. The sum of all volumes from the 57 model runs, divided by the catchment area, is whole-catchment drainage depth.

The Soil Ecohydraulic Model (SEM)

SEM is a one-dimensional model that assumes water drains vertically downward through user-defined soil layers in accordance with parameters that describe the vegetation dynamics and soil properties (Seyfried, 2003 and Seyfried et al., 2009). SEM requires time series of SWI, air temperature, and incoming solar radiation as boundary conditions.

SEM assumes that there is no overland flow and all water infiltrates into the soil at each timestep. If SWI is greater than the soil saturation water content (*SAT*) of the top layer, the top layer is assigned *SAT*, and additional water is routed to successively deeper layers. This process is repeated until all of the SWI is accounted for in the soil layers. If all layers are saturated, additional SWI routes directly to Dr.

Soil water drainage from each soil layer is a combination of infiltration passing through the layer and soil water between *SAT* and field capacity (*FC*) draining according to:

$$Dr_i = (\theta_i - FC_i) \times \exp(RDK \times \Delta t) \tag{5}$$

where the subscript i denotes the soil layer, θ is the soil layer volumetric water content, Δt is the model timestep, and *RDK* is the redistribution constant calculated as:

$$RDK = \frac{\log(0.05)}{RDT} \tag{6}$$

The exponential drainage assumption is based on the widespread observation that the rate of soil drainage is proportional to the amount of water stored in the profile. In

the absence of ET and SWI, and as consecutive time steps reach *RDT*, θ_i will approach FC_i within a distance of the argument of the logarithm.

RDT is a model parameter that defines the time it takes for a soil layer to be 95% drained or within 5% of *FC*. Seyfried et al. (2009) used a *RDT* value of 7.5 days. This value is retained based on an extensive analysis of measured soil moisture responses to melt-drain events, where the soil wets quickly then drains in the absence of *SWI* or *ET* (**Figure 4.4**). *RDK* accounts for both Darcian and preferred flow soil drainage processes. Dr (soil drainage to the soil bedrock interface) is simply the modeled Dr_i from the bottom soil layer.

Soil water storage capacity influences both the amount of water that is available for drainage to the soil bedrock interface and the amount of water available to plants after the spring rains cease in the early summer. Soil water storage capacity (S_c) at a point is defined by:

$$S_c = S_d \times (PEL - FC) \tag{7}$$

where S_d is soil depth. An S_c estimate of an entire catchment can be made by accounting for spatial variability in S_d, *PEL*, and *FC*. Catchment estimates of S_c are important for the catchment mass balance study because this is the volume of water that needs to be overcome in the fall to initiate catchment drainage, and it is also the volume of water available to be lost to ET after the cessation of spring rains.

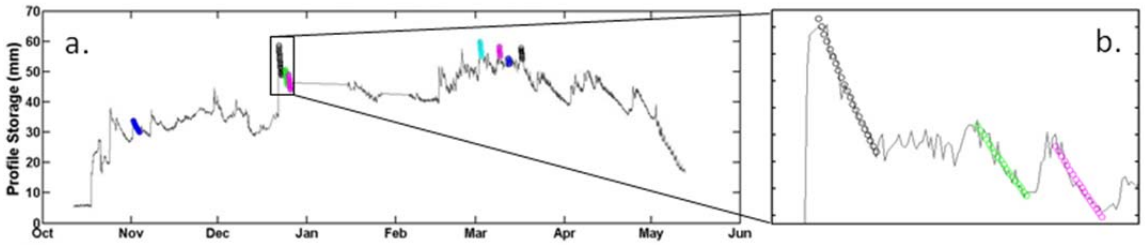

Figure 4.4 An example of a measured storage time series in 3a used to validate the 7.5 day redistribution time built into SEM. 3b shows a close up of the exponential decay curves fit to the data.

ET is modeled using a modified Preistly-Taylor approach (Priestley and Taylor, 1972) when snow cover is gone from the surface. Daily potential evapotranspiration (*PET*) is calculated by:

$$PET = \frac{1.26 \times \Delta \times \dfrac{R_n}{\lambda_v - (0.51 \times T_a)}}{\Delta + \gamma} \tag{8}$$

where Δ is the slope of the saturated vapor pressure versus air temperature line, R_n is the average daily net radiation (in langleys), λ_v is the latent heat of vaporization, T_a is the average daily air temperature, and γ is the psychrometric constant. R_n is calculated from average incoming solar radiation and a snow-free surface albedo, both of which are provided to the model by the user.

Actual evaporation (E) is calculated as a decreasing function of time from the last water input event (t_{swi}):

$$E = E_{el} \times \left(\sqrt{t_{swi}} - \sqrt{t_{swi} - 1}\right) \tag{9}$$

where E_{el} is the energy limited soil evaporation:

$$E_{el} = PET \times \exp(-0.4 \times LAI) \tag{10}$$

The leaf area index (LAI) time series is represented by two shape factors (*C* and *D*), the time of peak LAI (LAI_{pk}), minimum LAI (LAI_{min}), growing season start time (GS_{st}), and maximum LAI (LAI_{max}) parameters as:

$$LAI_t = LAI_{\max} \times \left[\frac{t - GS_{st}}{GS_{pk} - GS_{st}} \right]^C \times \exp\left(\frac{C}{D} \times 1 - \left[\frac{DOY - GS_{st}}{GS_{pk} - GS_{st}} \right]^D \right) \tag{11}$$

If θ is less than or equal to *PEL*, *E* is calculated as:

$$E = 0.05 \times E_{el} \tag{12}$$

E is bounded to have a maximum value of 2 mm on a day where SWI occurs. *E* is also limited so that the surface θ has a minimum value of 0.02.

Potential transpiration (*PTran*) is calculated after *E* is accounted for by:

$$PTran = \frac{PET \times LAI}{3} \tag{13}$$

PTran is set to *PET* if *LAI* is greater than or equal to 3.0. Actual transpiration from the soil profile (*T*) is then limited by the wettest soil layer by:

$$T = Ptran \times maxratio\,, \tag{14}$$

where *maxratio* is a measure of the water availability of wettest soil layer:

$$maxratio = \max\left(\frac{\theta_i - PEL_i}{FC_i - PEL_i} \right) \tag{15}$$

T is distributed across soil layers based on a combined weighting function that accounts for the proportion of a layer of the total profile thickness, available soil

moisture, and root distribution. The root distribution is assumed have an exponential decline with depth based on a user-defined maximum rooting depth (Jackson, 1996). A constraint is imposed so that the sum of *P* and *E* cannot exceed *PET*.

Modeled and measured soil water storage (*S*) is calculated from modeled and measured soil moisture contents (θ) remaining after Dr_i, *E*, and *T* are accounted for in all layers as:

$$S = \sum_{i=1}^{\#\text{soil layers}} \theta_i z_i \tag{16}$$

where z_i is the soil layer thickness of layer *i*. Both field measurements and model outputs are expressed in θ_i and converted to storage to get a magnitude of water storage.

Measurements

Air temperature and incoming solar radiation are recorded hourly at the TL weather station (**Figure 4.1**) and are summarized in Kormos et al. (2013b). **Figure 4.5** shows daily values of model input data. A pressure transducer in a v-notch weir records stream stage every hour, which is converted to discharge with a well-established rating curve. Soil depth was measured at 57 points distributed across TL by pounding a steel rod through the soil profile to refusal (Williams et al., 2009). Soil particle size analyses were performed on the top 30 cm at each of the 57 points. Soil moisture is recorded at 2 depths at 5 SW soil moisture profiles and at 5 depths at 2 NE soil profiles.

A three meter wide lateral flow collection profile was installed at an existing surface runoff plot on the NE slope to evaluate the use of a one dimensional soil model, which does not account for lateral flow (**Figure 4.1**). Lateral flow was collected at the

soil surface (overland flow), soil horizons at 40 cm and 125 cm, and at the soil bedrock interface. Two steel troughs installed at soil horizons were plumbed directly to tipping buckets. Pumps installed in two bedrock surface depressions routed water through a tipping bucket. A wicking material attached to an impermeable plastic sheet was installed on the trench face between collection horizons to ensure all lateral flow across the pit face was transferred to a collection point. The trench was backfilled.

Parameterizing the Soil Ecohydraulic Model

Soil layers were defined for each of the 57 model points based on the following criteria. Each point consists of a 2.5 cm soil surface layer that is underlain by a 7.5 cm layer. The thickness of deeper soil layers is dependent on measured soil depth at that location. If a pit is less than 30 cm, the rest of the soil depth is taken up with a third layer. If the pit is deeper than 30 cm, a third layer is assigned 12.5 cm. If a soil pit is less than 60 cm, the fourth soil layer takes up the rest of the soil depth to bedrock. If the soil pit is greater than 60 cm, the fourth layer is 22.5 cm thick, and a fifth layer will take up the rest of the soil depth until a pit reaches 100 cm. If a point has a depth over 100 cm, a 30 cm fifth layer is created and the rest of the soil depth is attributed to a sixth layer. Six layers was the maximum number of soil layers.

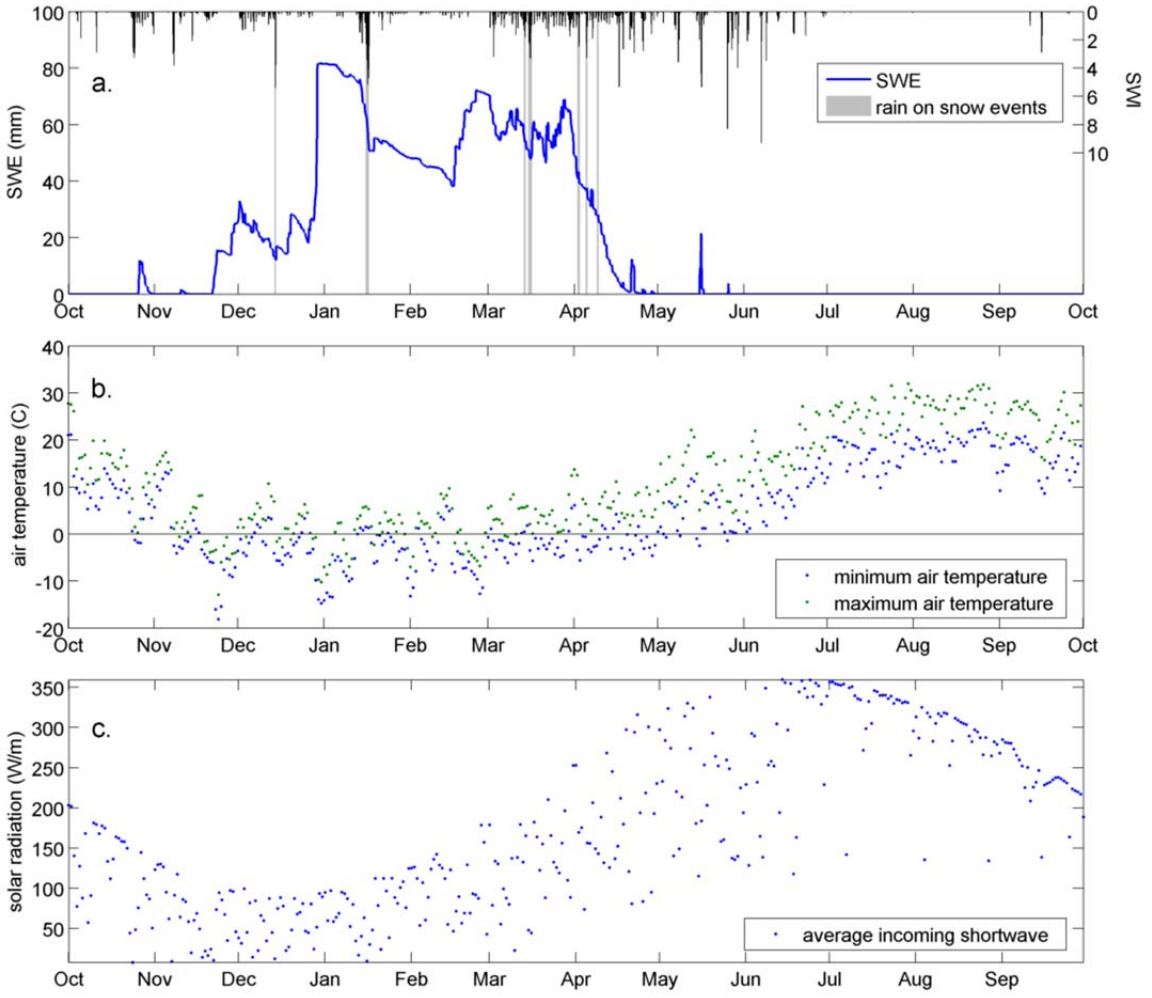

Figure 4.5 SWI (a), air temperature (b), and incoming solar radiation (c) data used to drive SEM. Rain on snow events are shown with corresponding SWI and snow depth responses (a).

Model parameters required by SEM that were not directly measured are listed in **Table 4.1** with a brief description of the method used to obtain values. Values of *SAT*, *FC*, and *PEL* need to be provided for each soil layer. *FC* and *PEL* are empirically derived from measured soil moisture time series following the methods of Smith et al. (2011) (**Figure 4.2**). A separate linear relationship between soil depth and *FC* was developed for the NE and SW slopes (**Figure 4.6**). A minimum *FC* value of 0.16 was imposed based on the work of Geroy et al. (2011) and Smith et al. (2011). Separate step

models between soil depth and *PEL* values were developed for the NE and SW slopes. A minimum value of 0.040 was used for both slopes for soil depths between 0 cm and 5 cm. Soil layers on the NE slope with a midpoint deeper than 5 cm were assigned a *PEL* value of 0.093, while soil layers on the SW slope with a midpoint deeper than 5 cm were assigned a *PEL* value of 0.072. *SAT* was defined for all soil layers using an empirical relationship between soil texture and *SAT* (Saxton et al., 1986, Flerchinger et al., 1996 and Flerchinger and Pierson, 1991). Measured surface soil texture data (0-30 cm) was used to calculate *SAT* for appropriate soil layers. Deeper soil texture values were obtained from sparse measurements on the north aspect (Yenko, 2003). A snow-free surface albedo of 0.15 was used based on 4-component radiometer data from the site, which agrees with albedo values used by Flerchinger et al. (1996) for a similar site. Rooting depth was assumed to be the measured soil depth, which assumes that plants root to the bedrock surface. Previous studies (Spence, 1937) and field investigations on the NE slope confirm the presence of roots at the bedrock surface.

Table 4.1 List of model parameters with a brief description of the methods used to obtain parameter values.

Parameter	Method
field capacity (FC)	Empirical from Measured Annual SM Data (Figure 4.5)
plant extraction limit (PEL)	Empirical from Measured Annual SM Data (Figure 4.5)
soil saturation (SAT)	Empirical from Measured Texture Data (Saxton, 1986)
redistribution time (RDT)	Literature value, (Seyfried et al. 2009) and empirical validation
leaf area index time series (LAI)	Combination of optimization and knowledge of field site

Separate LAI time series are constructed for SEM points on NE and SW slopes because of observed differences in vegetation. Three of the six parameters that define the

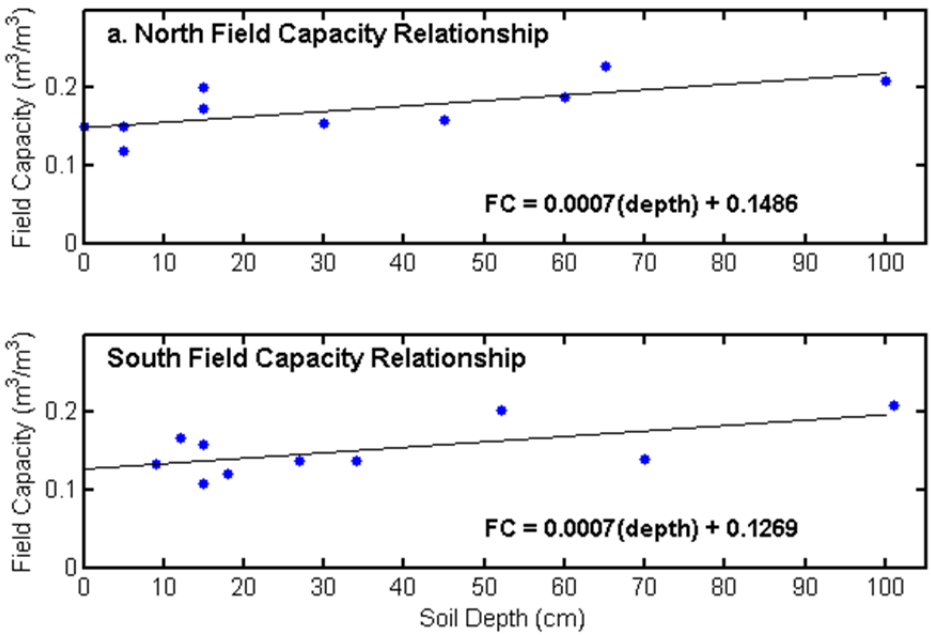

Figure 4.6 Field capacity vs. soil depth relationship

LAI time series (Equation 11) were optimized to each slope using measured soil moisture between plant green up and soil dry down (April 5th, 2011 to July 20st, 2011). Prior knowledge of soil dynamics at TL leads us to use the snow melt out dates for the GS_{st}. Slope average melt out dates are obtained from iSNOBAL modeled pixels. The C and D shape factors are selected to insure that the LAI time series rises quickly and returns to minimum value by mid August, as is observed at TL. GS_{pk}, LAI_{min}, and LAI_{max} parameters are optimized to each slope using an unconstrained nonlinear search function (simplex gradient) to minimize the root mean square error (RMSE) between modeled and measured soil moisture. Measured soil moisture from all depths from Npit3 and Npit4 on the NE slope and profiles SU10, SU5, and SU20 on the SW slope were used. Profiles

SD5 and SU30 were emitted from the LAI parameter optimization because of suspected upslope contributions to deep soil moisture values, which are not accounted for in SEM.

Results

Surface Water Inputs (SWI)

SWI was modeled for TL for WY2011 using the fully-distributed physically based iSNOBAL model to account for the complicated accumulation and melt dynamics typical of the rain-snow transition zone (Kormos et al., 2013a). SWI values accounted for precipitation corrections and sublimation from the snowpack. Measured precipitation (779 mm unshielded, 855 mm shielded) was corrected for wind effects (935 mm), and redistributed over the catchment (859 mm basin average). Modeled sublimation totaled 47 mm resulting in a basin average of 812 mm of SWI_{tot} for WY2011. We estimate an uncertainty of 32 mm based on the averaged RMSE between measured and modeled SWE during 10 snow surveys. Uncertainty in the total precipitation amount due to wind redistribution alone was approximately +/-20 mm. We conservatively use the higher magnitude of 32 mm as our uncertainty in the SWI, knowing some of the error in snow water equivalent comes from accumulation dynamics as well as differential melt dynamics. Our best estimate of SWI uncertainty that combines these errors comes from direct comparison between measured and modeled snow water equivalent.

Streamflow (Q_s)

Q_s at TL typically initiates in the winter and ceases in the late spring to early summer (**Figure 4.7b**). Peaks in January, December, and March are associated with ROS events (**Figure 4.5a and 4.7c**). The total Q_s at the outlet weir for WY2011 is 303 mm

(**Figure 4.8**). We estimate the uncertainty in Q_s at 10% based on having a stable control structure with 8 to 12 stage-discharge measurements per year (Harmel et al., 2006).

Soil Moisture Observations and Simulations

The soil moisture time series for WY2011 illustrates the commonly observed soil moisture conditions described by McNamara et al. (2005), with relatively stable wet and dry periods bounded by sharp increases and decreases (**Figure 4.2**). Soil moisture begins at the *PEL* in October and increases in response to fall rains and early snow-melt cycles. Deep soils on the NE slope generally reach *FC* in December in response to snow melt and a ROS event. The soil moisture values remain at or above *FC* until early May, when ET begins to dry the soil below *FC*. Spring rains extend the time that soil moisture is elevated above the *PEL*, which is reached between early July and mid August.

Lateral flow occurs predominantly at the soil bedrock interface as deep soil moisture increases above approximately 0.23 during the December ROS event (**Figure 4.9)**. This example time period is chosen because of expected tipping bucket failure following this event. Overland flow data is not included because expected errors due to the area of the collection trough are an order of magnitude larger than the overland flow recorded. No lateral flow was collected at the trough approximately 125 cm below the soil surface.

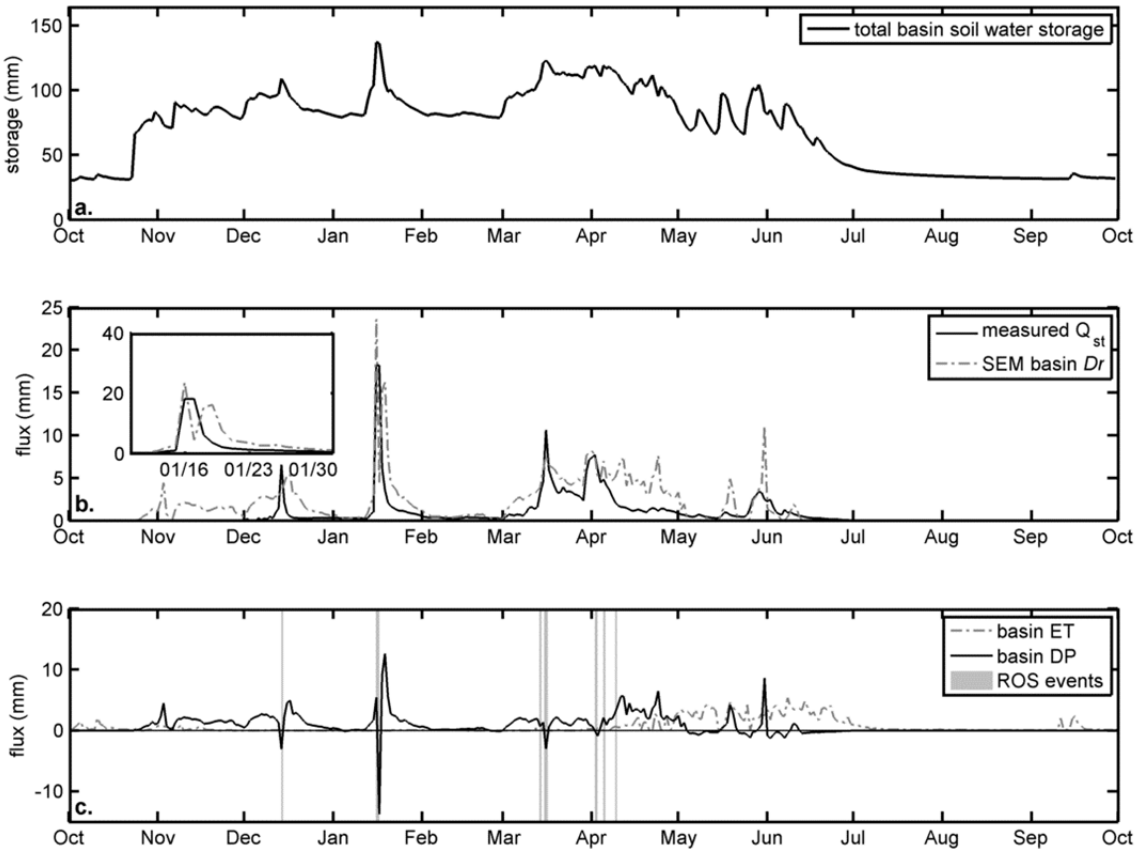

Figure 4.7 Catchment soil storage (a), measured stream discharge (Q_{st}) and modeled soil drainage (Dr) (b), and calculated DP compared to modeled evapotranspiration (ET) showing that early rain-on-snow events do not coincide with significant ET fluxes (c). The inset plot in b. show the discrepancy between measured and modeled peak for the January ROS event.

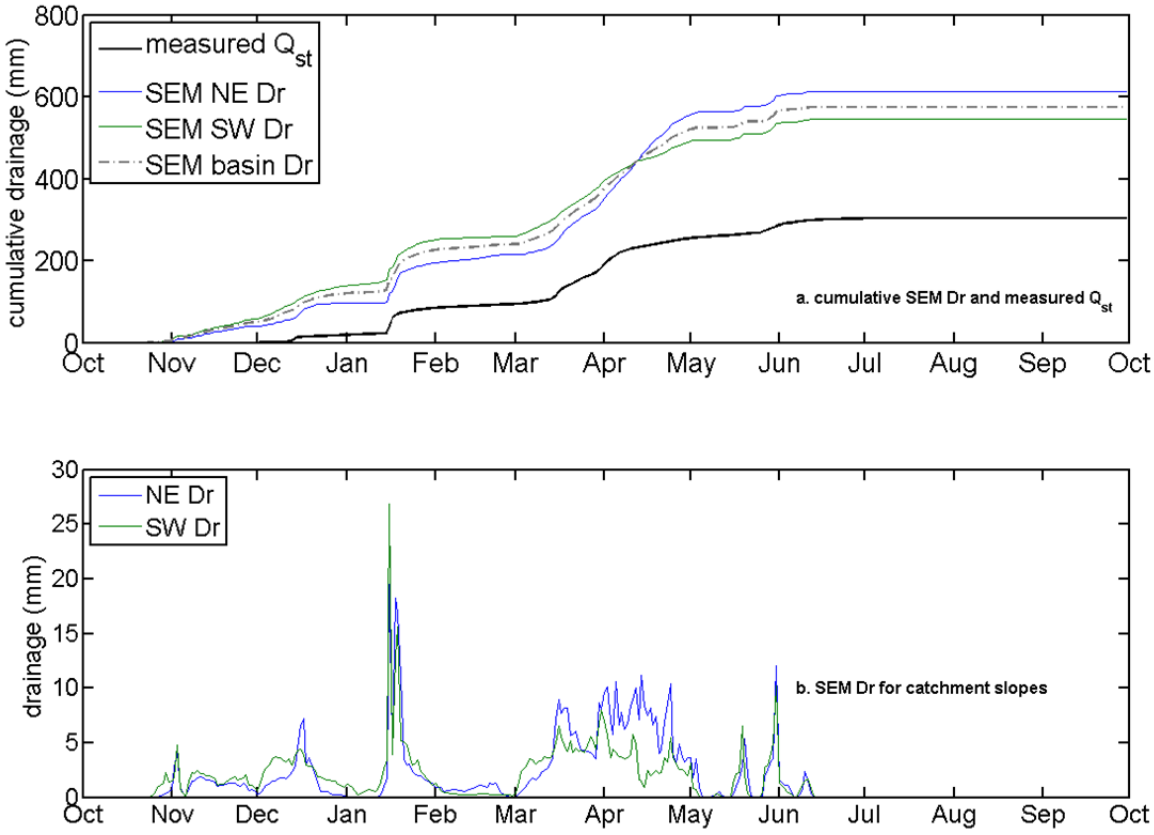

Figure 4.8 Cumulative Dr_{bas}, Q_{st}, and Dr from the NE and SW slopes showing the timing and magnitude of total slope Dr contributions (a). Slope-averaged Dr time series (b).

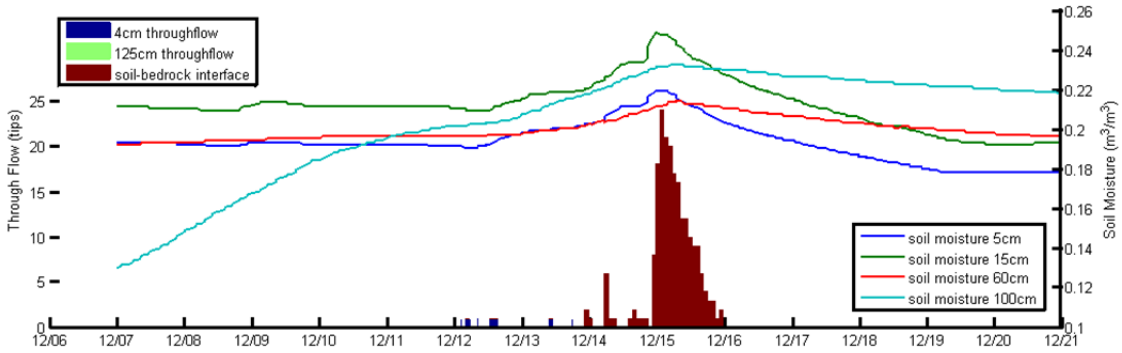

Figure 4.9 Measured lateral fluxes from the lateral flow collection profile showing the timing of soil moisture increases compared to lateral flow production.

Modeled shallow soil moisture commonly peaks higher and flatter than measured data on the NE slope. Modeled soil moisture at 15 cm repeatedly drops below measured data (**Figure 4.2**). Discrepancies between measured and modeled soil moisture may result from errors in the timing and magnitude of modeled SWI or mischaracterizing the soil parameters in SEM. High and flat modeled peak values may be an artifact of the daily time step used in SEM.

Modeled point SEM19 is closer to 3 different measurement sites than any other modeled point. The modeled storage from SEM19 fits measured data from SU5, SU10, and SU20 relatively well (**Figure 4.10**). Modeled storage from SEM8 performs well

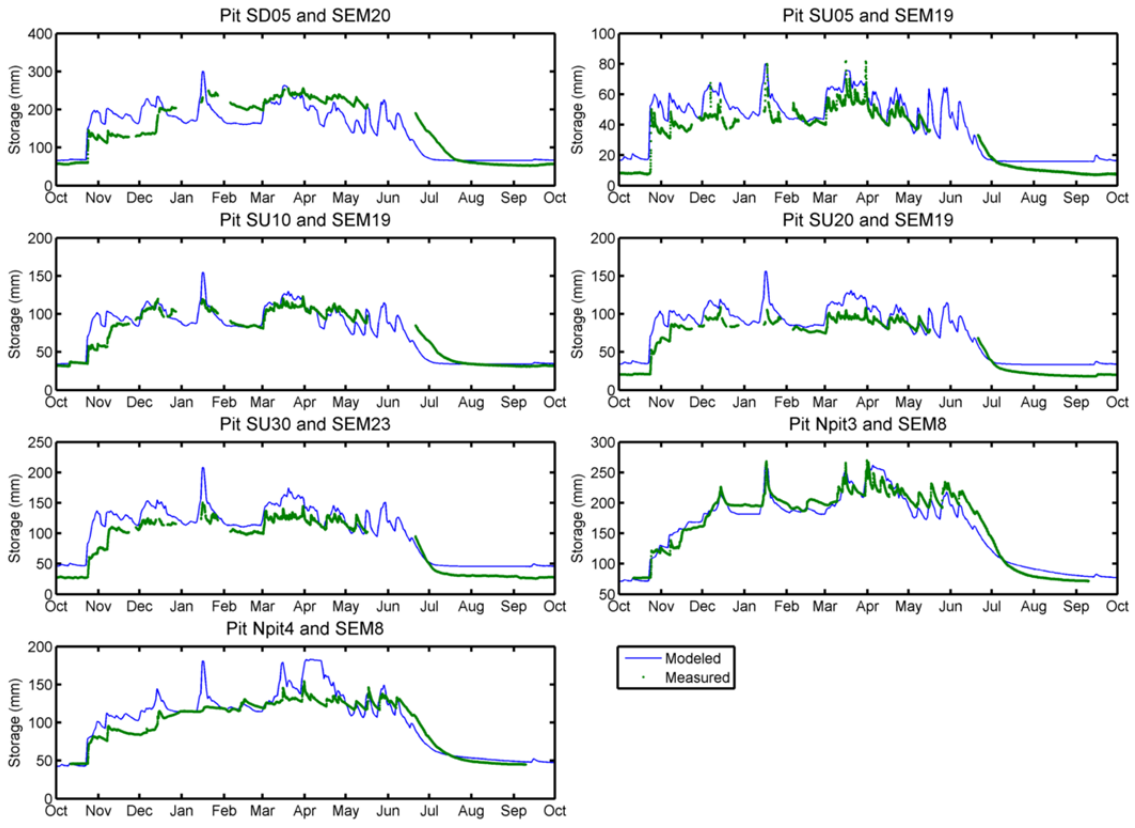

Figure 4.10 Measured and modeled soil water storage for each of the soil pits in TL. Modeled results are from the closest modeled point and modeled depths are modified to match the measured soil depth at the soil pits for comparison.

during wet-up when compared to measurements at both pits N3 and N4, but underestimates the storage from Npit3. These discrepancies demonstrate the high variability in soil moisture values measured over a relatively short distance. For comparison purposes only, the soil layer depths used to calculate modeled storage are modified to match the measured layer soil depths at the soil pits. This allows us to use the modeled soil moisture to calculate storage for thicknesses of soil at the measurement profiles for direct comparisons. Systematic deviations between measured and modeled soil water storage are attributed to uncertainty in the LAI time series, the distribution of *PEL* and *FC* soil parameters, or preferential flow, which allows deeper soils to wet up quickly. Slope area weighted RMSE between measured and modeled soil water storage is 19 mm.

The total modeled Dr_{cat} from WY2011 from Equation 2 is 614 mm (**Figure 4.8**).

Modeled Evapotranspiration

Modeled ET from SEM is 196 mm (**Figure 4.7c**). Since ET is not directly measured, it is difficult to estimate the modeled ET error. However, we attempt to estimate the uncertainty in ET using a suite of model parameter sets that define the LAI time series. LAI time series parameter sets are obtained by calibrating to each soil moisture measurement profile (2 on the NE slope and 4 on the SW slope) during the time period when ET was active (April 5th to July 20th). Profile SD5 was excluded from the ET error analysis because of suspected upslope contributions to deep soil moisture, which is not accounted for in SEM. We then ran a Monte Carlo simulation, where every possible combination of parameters sets for the 2 slopes were used to run SEM

distributed across TL. The standard deviation in the total modeled ET from these runs was 6 mm.

Deep Percolation in the Annual Water Balance

DP is estimated from **Equation 3** as 311 mm, which is 36% of the basin-averaged distributed precipitation during that time. The uncertainty associated with this DP estimate cannot be obtained by comparing it to direct measurements. We can, however, obtain a combined error in ET_{tot} and DP_{tot} from errors obtained by comparing modeled results to direct measurements of SWE (for SWI), soil water storage, and Q_s. We assume that the errors in modeled $SWI_{tot,}$ soil water storage, and measured Q_{stot} are normally distributed and uncorrelated and use a simplified error propagation equation (resulting error is the square root of the sum of the squares) to estimate the error in ET_{tot} and DP_{tot} for the WY2011 as 48 mm. We can further constrain this using our error estimate of ET_{tot} (6 mm) and assuming that these errors are also normally distributed and uncorrelated to errors in $SWI_{tot,}$ soil water storage, and measured Q_{stot}. Since our error in ET_{tot} is very small, the error in DP_{tot} for the WY2011 is still 48 mm. This coincides with 36% ±12% of the distributed precipitation at 95% confidence and 36%±6% at 68% confidence using the standard deviation of the simulations. This is similar to estimates for TL from chloride mass balance methods for the same year (18% of wind corrected precipitation with a range of 3% to 37%, unpublished data following Aishlin and McNamara, 2011). Our estimate may be in the upper range of the chloride mass balance estimate because of chloride flushing caused by midwinter ROS events. These events may have sufficient soil water fluxes to flush chloride ions from previous years through the soil profile (Aishlin and McNamara, 2011).

Timing and Spatial Distribution of Soil Drainage and Deep Percolation

Distributed SEM modeling allows us to comment on the timing and spatial distribution of Dr. SW slopes contribute to catchment Dr more often than NE slopes from November to mid January and also in late February due to combination higher SWI and shallower soils (**Figures 4.8, 4.11d, e, f, and j, and 4.12d-j**) (Kormos et al., 2013a, and Kormos et al., 2013b). The magnitude of Dr is also often higher on the SW slope until mid March, after which the NE slope contributes more Dr until early May. The SW slope Dr increases more rapidly in response to precipitation and melt events from the onset of streamflow in early December to mid March (**Figure 4.8 b, and 4.11d and f**). This is a result of a more limited storage capacity (shallower soil depth) on SW slopes (Smith et al., 2011). NE slope Dr peaks higher and remains elevated longer staring mid March (**Figure 4.11k-n**). The SW slope contributes more cumulative Dr to TL until the

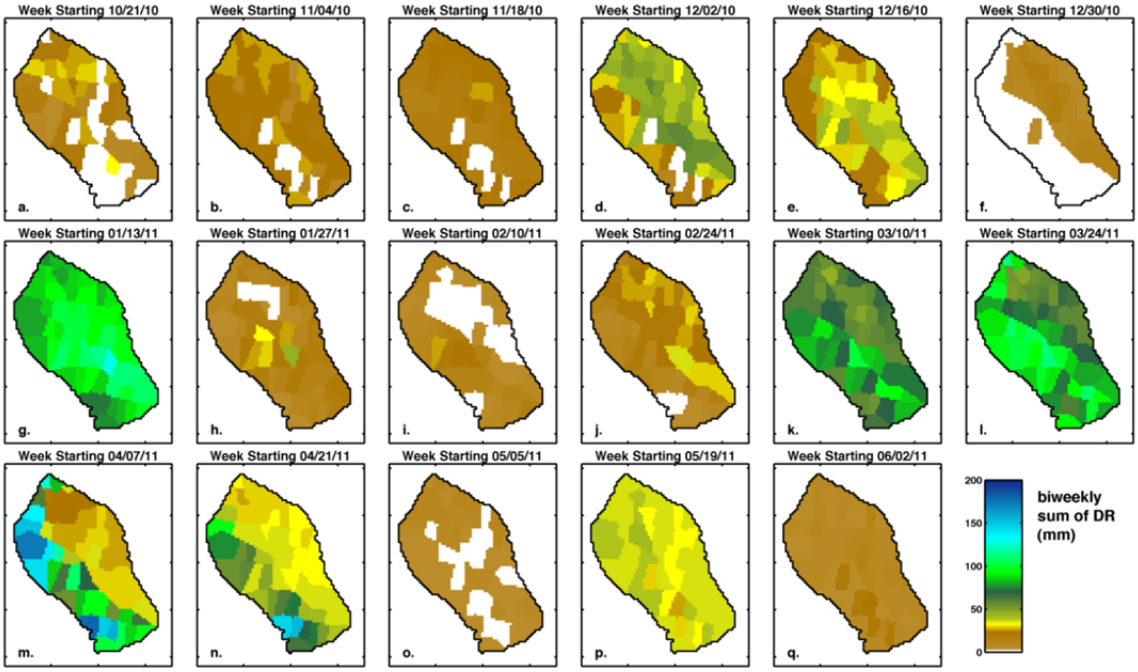

Figure 4.11 Biweekly distributed incremental Dr at TL.

beginning of April, just after the final spring melt commences (**Figures 4.8 and 4.12**). The NE slope contributes more Dr per area by the end of WY2011, mainly as a result of the distribution of precipitation (**Figures 4.8a and 4.12**) (Kormos et al., 2013a).

Although we can comment on the spatial distribution of Dr, it is difficult to translate that knowledge to the distribution of DP because of lateral flow at the soil bedrock interface and the unknown transmissive properties of that interface. This lateral flow from the area of Dr origin to the stream takes some amount of time. If this time lag is greater than the model time step (1 day), it will lead to errors in **Equation 2** when creating a DP time series (**Figure 4.7c).**

The timing of DP coincides with peaks in modeled whole catchment soil storage as well as peaks in measured Q_s (**Figure 4.7**). Negative DP calculations are a result of

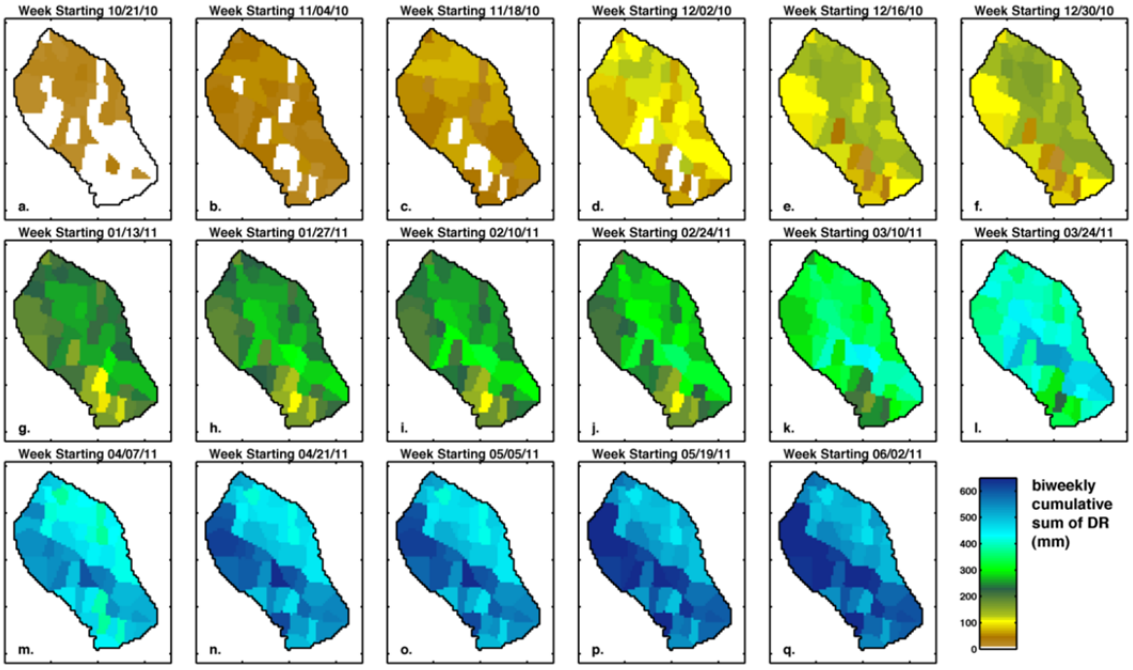

Figure 4.12 Biweekly cumulative distributed Dr at TL.

measured Q_s being greater than modeled Dr. Several sharp negative spikes in the DP time series (December 14th, and March 16th and 29th) are a result of measured discharge increasing before modeled drainage. This may be a result of 1) quick flow paths that are active in TL but not accounted for in the model, such as lateral flow within the snowpack, overland flow, or macropore flow, 2) faster soil water redistribution in TL compared to the modeled soil water redistribution, or 3) errors in the timing of SWI calculations from iSNOBAL. The negative DP values in February and after May 1st are a result of the Q_s recession being measured while the modeled soil drainage is zero. Modeled Dr tends to reach a zero value quickly after SWI events, while measured Q_s recessions are slower. The prolonged measured Q_s recession is evidence that there is certainly a time lag associated with lateral flow in TL. This is a result of lateral flow taking some time to get water from SEM polygons to the stream outlet. We assume negative DP values do not affect qualitative conclusions about the timing of DP events.

Discussion

Soil Drainage and Deep Percolation

Dr at TL occurs from late October to June (**Figures 4.7b and 4.8**). This is in contrast to higher elevation sites where Dr is expected to occur only during the spring ablation season (Murray and Buttle, 2005, and Seyfried et al., 2009). This mid elevation zone also receives greater amounts of precipitation than rain-dominated, lower elevations because of well-known orographic relationships. The timing and magnitude of Dr from the rain snow transition zone make it an important source of down slope, cold season streamflow (Knowles and Cayan, 2004). These contributions to down slope ecosystems

may play an important role in sustaining minimum in-stream low flows during the cold season that support resident fish populations in the Pacific Northwest and Great Basin regions.

Differences in the timing of catchment Dr between slopes may have implications for stream chemistry and spatial DP distributions. We expect streamflow chemistry to reflect the timing of water delivery from catchment soils. We know, for example in DCEW, that northern aspects contain higher soil carbon and nitrogen contents than southern aspects (Kunkel et al., 2011). We would therefore expect that winter season stream carbon and nitrogen concentrations to be lower than spring time concentrations. The spatial distribution of DP is a function the distribution of bedrock transmissive properties. More DP is expected from times when drainage occurs on slopes with higher bedrock transmissivity, opposed to more lateral flow on slopes with lower bedrock transmissivity. Situations where bedrock transmissivity varies with aspect include prevailing inclined fracture orientation parallel to a catchment slope, or differences in bedrock geology, as is common along faults.

The timing of DP lines up with peaks in both measured and modeled point and whole catchment soil storage, as well as peaks in measured Q_s (**Figures 4.7 and 4.10**). Large DP events coincide with ROS events in mid December, mid January, and mid March (**Figure 4.7c**). The December ROS event began on December 11th and extended to December 19th. Estimated streamflow for this period rises earlier than modeled Dr, which causes a negative spike in DP. This may be a result of the Q_s gap filling methods used to estimate early Q_s (Kormos et al., 2013b). The January ROS event begins on January 12th and extends through January 20th. It also contains a large negative dip in the

DP record on January 17th resulting from measured streamflow being greater than modeled Dr. This is primarily a result of modeled Dr peaks not matching measured Q_s (**Figure 4.7b inset**), which may result from errors in modeled SWI or SEM model parameters. A ROS event occurring between March 12th and March 20th also includes a large negative dip because the Dr and measured streamflow peaks are offset. Although 3 ROS events occur in April, they coincide with the spring snow melt event on the NE slope (March 29th to May 1st). It is difficult to separate DP related to ROS events versus ongoing snow melt.

Negative estimates of daily DP values from May 2nd to July 1st result from Q_s perpetuating into the summer while calculated Dr is zero. We attribute this to lateral flow occurring in the basin, which is not accounted for in the model. Q_s measured after May 1st could have entered the basin at anytime previous to May 2nd. The discussion of the timing of DP is therefore based on the assumption that this error is distributed evenly across the water year. We can then quantify the relative importance of events to DP. ROS events from December, January, and March contribute 17% of DP, while the spring melt event on the NE slope contributed 31%.

Performance of Storage-Based Modeling

Throughflow at TL occurs primarily at the soil bedrock interface with little to no flow collected at the soil surface or soil horizons (**Figure 4.9**). This data agrees with previous studies by Graham et al. (2010b). We feel that this data is sufficient to qualitatively validate the use of simplified modeling methods, including the use of a one dimensional model with vertical flow assumptions through the soil profile. The SEM model assumes that lateral moisture redistribution, such as overland flow or lateral flow

in the soil column, is negligible. The existence of streamflow, however, implies that lateral redistribution does indeed occur. Implicit in our approach is the assumption that both DP_t and Q_{st} result from partitioning of vertical infiltration at the soil bedrock interface. While lateral redistribution of water likely occurs throughout the snow-soil bedrock profile, close agreement of measured and modeled soil storage suggest that the magnitudes of lateral fluxes are small (**Figure 4.10**). Further, if such lateral fluxes reach the stream, they are incorporated into our total estimation of DP_{tot} via **Equation 3**.

We can directly compare our results to a chloride mass balance DP estimate made at TL for WY2011 using the same basin averaged distributed precipitation record used in this paper (unpublished data following Aishlin and McNamara, 2011). This approach estimates DP was 18% of precipitation of with a range from 3% to 37%, which agrees with our estimate of 36%±8%. We cannot directly compare the DP estimate obtained in this paper to previous published estimates because previous estimates did not distribute snow storms based on wind (Aishlin and McNamara, 2011, and Kelleners et al., 2010). There was a difference of 76 mm between the wind-corrected and basin averaged redistributed precipitation for WY2011 at TL (**Table 4.2**). However, if we assume that the fraction of precipitation that DP accounts for is similar our estimate of 36% ±8% of basin- averaged, distributed precipitation is within the estimates of 1% to 35% of wind-corrected precipitation and 34% to 36% of measured shielded precipitation.

The similarity between our results and results obtained using other methods suggest that the storage-centric approach presented in this paper is a useful tool when streamflow is an unreliable calibration target due to leakage. By focusing on simulating distributed soil moisture dynamics, we are able to estimate Dr_t, which includes DP_t and

Q_{st}. However, the method has several assumptions and drawbacks outlined in the following paragraphs that must be addressed.

The dominant storage reservoirs must be known and well characterized. TL is small and previous work demonstrated that snow and soil moisture storage dominate catchment response (Williams et al., 2009), while deep saturated groundwater flow is not important. As catchment size increases, storage mechanisms will likely become more complex. Distributed SWI must be well characterized because this approach relies on estimates of distributed soil moisture storage and drainage. This is challenging in snow dominated catchments, necessitating complicated physically based models driven by distributed inputs. The distribution of inputs is often difficult to obtain. In this study, precipitation was distributed according to empirical methods following Winstral et al. (2013) as described in Kormos et al. (2013a). The total amount of precipitation received by the catchment is sensitive to the parameters used in the wind redistribution procedure. An extensive dataset, including 10 repeat snow surveys and 6 ultrasonic depth sensors, was used to optimize these parameters. A minimum RMSE of 32 mm between measured and modeled snow water equivalent was obtained.

Characterizing the soil and plant properties of a basin from point measurements is difficult given the high spatial variability involved. *FC* and *PEL* parameters are empirically obtained from 20 soil moisture probes and at various locations and depths in a 0.015 km^2 catchment. *SAT* parameter values were calculated from soil texture data obtained from the 57 model point locations. Even though this is a high density of measured data, we recognize that soil properties and soil moisture magnitudes are highly variable over short distances (Brocca et al., 2012 and Fiener et al., 2012). Also, the

placement of soil moisture probes on the SW slope is not ideal for calculating measured soil moisture storage. Shallow probes placed in the top 15 cm of the soil profile may be influenced by evaporation from the soil surface when the snow disappears, causing lower soil moisture contents in late March, even though *PET* is low. Deep probes were placed at the soil-saprolite interface and may measure soil moisture increased due to the collection of water at that interface instead of a lower value if the soil column was allowed to drain freely. Deep probes may also record prolonged elevated moisture because of the influence of lateral flow from upslope contributing areas. The location of the deep probes and the fact that there are only two probes in each pit (the deep probe mathematically represents slightly less than 50% of the calculated storage value) may explain differences in measured and modeled soil water contents.

Aspect differences in soil and vegetation are considered a fundamental control on the hydrology of the study area (Tesfa et al., 2009, Geroy et al., 2011, Kunkel et al., 2011, and Smith et al., 2011). Vegetation differences are accounted for in SEM by separate LAI time series for NE and SW slopes. SW slopes have shallower soil and abundant shrubs that are able to root well below the measured soil depth. Calibrated LAI time series for the NE and SW slopes generally agree with vegetation studies in similar areas (Flerchinger et al., 1996, Groeneveld, 1997, Clark and Seyfried, 2001, Flanagan et al., 2002, Ivans et al., 2006, Steinwand et al., 2006, and Griffith et al., 2010). The peak LAI values are somewhat high for both the NE and SW slopes compared values reported in the literature. The high LAI value may be a result of a tree adjacent to the north soil pits and the fact that some south soil pits are close to the valley bottom where vegetation has access to water from the drainage network. Regardless of the high peak LAI values,

the modeled soil dry down agrees fairly well with measured dry down where measured (**Figures 4.2 and 4.10**). Aspect associated soil differences are accounted for in this study by having separate *FC* and *PEL* relationships with soil depth for each aspect, and varying

Table 4.2 Annual water balance terms and uncertainties from WY2011 at TL.

	WI	T	r		P
estimate (mm)	10	235	75	303	72
uncertainty (mm)	5	1	6	0	6

SAT with texture data obtained from each aspect. One of the main drawbacks of utilizing the SEM calculated Dr to estimate DP is that errors in modeled ET are inherited to DP (Essery and Wilcock, 1990, Simmers, 1997, and Scanlon et al., 2002). ET can be an especially large term in semi-arid environments. SEM uses a modified Priestly-Taylor (1972) equation that incorporates time-varying LAI (Equation 11) (Rose, 1984; Seyfried, 2003) and available soil moisture (Shuttleworth, 1992). Potential errors are assumed to be low in the winter, when temperatures are low and snow cover inhibits significant ET. Errors are expected to increase for much of April, when the soil moisture content is above *FC* (**Figures 4.2 and 4.10**), snow cover is absent (**Figure 4.6**), and modeled ET is increasing (**Figure 4.7c**) (Krestovskiy et al., 1979, Willmott et al., 1985, and Blankinship and Hart, 2012). These circumstances lead to a competition between ET and Dr for soil moisture until soil moisture drops to *FC*. This complicated interaction between ET and Dr is poorly understood and warrants further study.

Conclusions

DP from TL for the WY2011 is 311 mm ±48 mm or 36% ±6% of wind-corrected precipitation at the weather station. Both ROS and the spring melt contribute significantly to the total DP for WY2011. Large DP events coincide with ROS events in mid December, mid January, and mid March. The SW slope drains more often throughout WY2011, but the NE slope contributes a greater total magnitude of Dr. Modeling efforts that focus on high degrees of similarity between measured and modeled soil water storage work well in TL and are expected to perform well in catchments where the majority of lateral flow occurs at the soil bedrock interface. Complex snow accumulation and melt dynamics warrant the use of a distributed physically based snow model, while relatively simple catchment soil properties allow us to use a capacitance based soil model to represent catchment soil dynamics. The agreement between the timing of measured discharge peaks and modeled soil outflow peaks is verification that the model performs well. The benefits of using SEM include a limited number of conceptually-tangible parameters leading to a relatively quick setup time and limited computational expense. Methods that neglect the time lag from soil drainage to streamflow are expected to lead to degraded performance with increasing catchment size. However, the simplified approach described here may provide a good estimate of the timing and magnitude of recharge events at larger scales. Recharge estimates for larger basins with regional groundwater influences should consider a more complex model that represents the important hydrologic processes of that basin.

Acknowledgements

We thank Jason Williams for assisting in the preparation of this manuscript and Pam Aishlin for field data collection and processing. We thank the students, faculty, and scientist at the Northwest Watershed Research Center and Boise State University Department of Geosciences for intellectual support. We thank the Northwest Watershed Research Center and Boise State University Department of Geosciences, Student Research Initiative, and Graduate College for funding support, travel support, and general support. NASA EPSCoR and INRA provided funding for this project. The collection and processing of the data presented in this paper were funded in part by NSF-CBET (0854553, 08522), USDA-ARS CRIS Snow and Hydrologic Processes in the Intermountain West (5362-13610-008-00D), USDA-NRCS Water and Climate Center-Portland, Oregon (5362-13610-008-03R), NSF-EPS (0919514), and NOAA (NA08NWS4620047). Any reference to specific equipment types or manufacturers is for information purposes and does not represent a product endorsement or recommendation. Boise State University and the USDA ARS are equal opportunity employers.

References

Abdelmasih DMM. 2006. Influence of Saturated Wedge Hydrodynamics on Hillslope-Stream Connectivity. In: Department of Geosciences, Boise State University, pp: 127.

Aishlin P, McNamara JP. 2011. Bedrock infiltration and mountain block recharge accounting using chloride mass balance. Hydrological Processes, 25: 1934-1948. DOI: 10.1002/hyp.7950.

Ajami H, Troch PA, Maddock T, Meixner T, Eastoe C. 2011. Quantifying mountain block recharge by means of catchment-scale storage-discharge relationships. Water Resources Research, 47. DOI: W04504 10.1029/2010wr009598.

Bales RC, Hopmans JW, O'Geen AT, Meadows M, Hartsough PC, Kirchner P, Hunsaker CT, Beaudette D. 2011. Soil Moisture Response to Snowmelt and Rainfall in a Sierra Nevada Mixed-Conifer Forest. Vadose Zone Journal, 10: 786-799. DOI: 10.2136/vzj2011.0001.

Bartolini E, Allamano P, Laio F, Claps P. 2011. Runoff regime estimation at high-elevation sites: a parsimonious water balance approach. Hydrology and Earth System Sciences, 15: 1661-1673. DOI: 10.5194/hess-15-1661-2011.

Bayard D, Stahli M, Parriaux A, Fluhler H. 2005. The influence of seasonally frozen soil on the snowmelt runoff at two Alpine sites in southern Switzerland. Journal of Hydrology, 309: 66-84. DOI: 10.1016/j.jhydrol.2004.11.012.

Blankinship JC, Hart SC. 2012. Consequences of manipulated snow cover on soil gaseous emission and N retention in the growing season: a meta-analysis. Ecosphere, 3: art1. DOI: 10.1890/es11-00225.1.

Brocca L, Tullo T, Melone F, Moramarco T, Morbidelli R. 2012. Catchment scale soil moisture spatial-temporal variability. Journal of Hydrology, 422: 63-75. DOI: 10.1016/j.jhydrol.2011.12.039.

Brutsaert W, Nieber JL. 1977. Regionalized drought flow hydrographs from a mature glaciated plateau. Water Resources Research, 13: 637-644. DOI: 10.1029/WR013i003p00637.

Campbell GS, Harris GA. 1977. Water relations and water-use patterns for Artemisia-Tridentata-Nutt in wet and dry years. Ecology, 58: 652-659. DOI: 10.2307/1939015.

Cayan DR, Kammerdiener SA, Dettinger MD, Caprio JM, Peterson DH. 2001. Changes in the onset of spring in the western United States. Bulletin of the American Meteorological Society, 82: 399-415. DOI: 10.1175/1520-0477(2001)082<0399:citoos>2.3.co;2.

Clark PE, Seyfried MS. 2001. Point sampling for leaf area index in sagebrush steppe communities. Journal of Range Management, 54: 589-594. DOI: 10.2307/4003589.

Cuo L, Beyene TK, Voisin N, Su FG, Lettenmaier DP, Alberti M, Richey JE. 2011. Effects of mid-twenty-first century climate and land cover change on the hydrology of the Puget Sound basin, Washington. Hydrological Processes, 25: 1729-1753. DOI: 10.1002/hyp.7932.

Dijksma R, Brooks ES, Boll J. 2011. Groundwater recharge in Pleistocene sediments overlying basalt aquifers in the Palouse Basin, USA: modeling of distributed recharge potential and identification of water pathways. Hydrogeology Journal, 19: 489-500. DOI: 10.1007/s10040-010-0695-9.

Essery CI, Wilcock DN. 1990. Checks on the measurement of potential evapotranspiration using water-balance data and independent measures of groundwater recharge. Journal of Hydrology, 120: 51-64. DOI: 10.1016/0022-1694(90)90141-j.

Feiccabrino J, Lundberg A, Gustafsson D. 2012. Improving surface-based precipitation phase determination through air mass boundary identification. Hydrology Research, 43: 179-191. DOI: 10.2166/nh.2012.060.

Fiener P, Dlugoss V, Korres W, Schneider K. 2012. Spatial variability of soil respiration in a small agricultural watershed - Are patterns of soil redistribution important? Catena, 94: 3-16. DOI: 10.1016/j.catena.2011.05.014.

Flanagan LB, Wever LA, Carlson PJ. 2002. Seasonal and interannual variation in carbon dioxide exchange and carbon balance in a northern temperate grassland. Global Change Biology, 8: 599-615. DOI: 10.1046/j.1365-2486.2002.00491.x.

Flerchinger GN, Cooley KR. 2000. A ten-year water balance of a mountainous semi-arid watershed. Journal of Hydrology, 237: 86-99. DOI: 10.1016/s0022-1694(00)00299-7.

Flerchinger GN, Hanson CL, Wight JR. 1996. Modeling evapotranspiration and surface energy budgets across a watershed. Water Resources Research, 32: 2539-2548. DOI: 10.1029/96wr01240.

Flerchinger GN, Pierson FB. 1991. Modeling plant canopy effects on variability of soil-temperature and water. Agricultural and Forest Meteorology, 56: 227-246. DOI: 10.1016/0168-1923(91)90093-6.

Flint AL, Flint LE, Hevesi JA, Blainey JB. 2004. Fundamental concepts of recharge in the Desert Southwest: a regional modeling perspective. In: Groundwater Recharge in a Desert Environment: The Southwestern United States, Hogan JF, Phillips FM, Scanlon BR (eds.) AGU, pp: 159-184.

Geroy IJ, Gribb MM, Marshall HP, Chandler DG, Benner SG, McNamara JP. 2011. Aspect influences on soil water retention and storage. Hydrological Processes, 25: 3836-3842. DOI: 10.1002/hyp.8281.

Graham C, van Verseveld W, Barnard H, McDonnell J. 2010a. Estimating the deep seepage component of the hillslope and catchment water balance within a measurement uncertainty framework. Hydrological Processes, 24: 3631-3647. DOI: 10.1002/hyp.7788|10.1002/hyp.7788.

Graham CB, Woods RA, McDonnell JJ. 2010b. Hillslope threshold response to rainfall: (1) A field based forensic approach. Journal of Hydrology, DOI: 10.1016/j.jhydrol.2009.12.015.

Gribb MM, Forkutsa I, Hansen A, Chandler DG, McNamara JP. 2009. The Effect of Various Soil Hydraulic Property Estimates on Soil Moisture Simulations. Vadose Zone Journal, 8: 321-331. DOI: 10.2136/vzj2008.0088.

Griffith AB, Alpert H, Loik ME. 2010. Predicting shrub ecophysiology in the Great Basin Desert using spectral indices. Journal of Arid Environments, 74: 315-326. DOI: 10.1016/j.jaridenv.2009.09.002.

Groeneveld DP. 1997. Vertical point quadrat sampling and an extinction factor to calculate leaf area index. Journal of Arid Environments, 36: 475-485. DOI: 10.1006/jare.1996.0213.

Guan H, Simunek J, Newman BD, Wilson JL. 2010. Modelling investigation of water partitioning at a semiarid ponderosa pine hillslope. Hydrological Processes, 24: 1095-1105. DOI: 10.1002/hyp.7571.

Han SM, Yang YH, Fan T, Xiao DP, Moiwo JP. 2012. Precipitation-runoff processes in Shimen hillslope micro-catchment of Taihang Mountain, north China. Hydrological Processes, 26: 1332-1341. DOI: 10.1002/hyp.8233.

Harmel RD, Cooper RJ, Slade RM, Haney RL, Arnold JG. 2006. Cumulative uncertainty in measured streamflow and water quality data for small watersheds. Transactions of the Asabe, 49: 689-701.

Hevesi JA, Flint AL, Flint LE. 2003. Simulation of net infiltration and potential recharge using a distributed-parameter watershed model of thedeath valley region, Nevada and California. In: Water-Resources Investigations Report, US Geological Survey, pp: 171.

Hillel D. 1998. Environmental soil physics: fundamentals, applications, and environmental considerations. Academic press.

Hogan JF, Phillips FM, Scanlon BR. 2004. Preface to Groundwater Recharge in a Desert Environment: The Southwestern United States. In: Groundwater Recharge in a Desert Environment: The Southwestern United States, Hogan JF, Phillips FM, Scanlon BR (eds.) American Geophysical Union, pp: vii.

Ivans S, Hipps L, Leffler AJ, Ivans CY. 2006. Response of water vapor and CO2 fluxes in semiarid lands to seasonal and intermittent precipitation pulses. Journal of Hydrometeorology, 7: 995-1010. DOI: 10.1175/jhm545.1.

Jackson RB, Canadell J, Ehleringer JR, Mooney HA, Sala OE, Schulze ED. 1996. A global analysis of root distributions for terrestrial biomes. Oecologia, 108: 389-411. DOI: 10.1007/BF00333714.

Jie Z, van Heyden J, Bendel D, Barthel R. 2011. Combination of soil-water balance models and water-table fluctuation methods for evaluation and improvement of groundwater recharge calculations. Hydrogeology Journal, 19: 1487-1502. DOI: 10.1007/s10040-011-0772-8.

Kelleners TJ, Chandler DG, McNamara JP, Gribb MM, Seyfried MS. 2009. Modeling the Water and Energy Balance of Vegetated Areas with Snow Accumulation. Vadose Zone Journal, 8: 1013-1030. DOI: 10.2136/vzj2008.0183.

Kelleners TJ, Chandler DG, McNamara JP, Gribb MM, Seyfried MS. 2010. Modeling Runoff Generation on in a Small Snow-Dominated Mountainous Catchment. Vadose Zone Journal, 9: 517-527. DOI: 10.2136/vzj2009.0033.

Kirchner JW. 2009. Catchments as simple dynamical systems: Catchment characterization, rainfall-runoff modeling, and doing hydrology backward. Water Resources Research, 45. DOI: W02429 10.1029/2008wr006912.

Knowles N, Cayan DR. 2004. Elevational dependence of projected hydrologic changes in the San Francisco Estuary and watershed. Climatic Change, 62: 319-336. DOI: 10.1023/B:CLIM.0000013696.14308.b9.

Kormos, PR, Marks, D, McNamara, JP, Marshall, HP, Winstral, A, Flores, AN. 2013a, Snow distribution, melt and surface water inputs to the soil in the mountain rain-snow transition zone. Journal of Hydrology, in review.

Kormos, PR, Marks, D, McNamara, JP, Williams, CJ, Marshall, HP, Aishlin P, Chandler, DG, 2013b. Soil, Snow, Weather, and Sub-surface Storage Data from a Mountain Catchment in the Rain-Snow Transition Zone. Earth System Science Data, in review.

Krestovskiy, Postnikov A, Sergeyeva A. 1979. Estimation of evaporation from the forest in early spring. Soviet Hydrology, 18: 181—186.

Kunkel ML, Flores AN, Smith TJ, McNamara JP, Benner SG. 2011. A simplified approach for estimating soil carbon and nitrogen stocks in semi-arid complex terrain. Geoderma, 165: 1-11. DOI: 10.1016/j.geoderma.2011.06.011.

Makurira H, Savenije HHG, Uhlenbrook S. 2010. Modelling field scale water partitioning using on-site observations in sub-Saharan rainfed agriculture. Hydrology and Earth System Sciences, 14: 627-638. DOI: 10.5194/hess-14-627-2010.

Marks, D., Domingo, J., Susong, D., Link, T., Garen, D., 1999. A spatially distributed energy balance snowmelt model for application in mountain basins. Hydrological Processes, 13(12-13): 1935-1959. doi: 10.1002/(SICI)1099-1085(199909)13:12/13<1935::AID-HYP868>3.0.CO;2-C.

Marks D, Dozier J. 1992. Climate and energy exchange at the snow surface in the alpine region of the Sierra-Nevada .2. Snow cover energy-balance. Water Resources Research, 28: 3043-3054. DOI: 10.1029/92wr01483.

Maxwell RM. 2010. Infiltration in Arid Environments: Spatial Patterns between Subsurface Heterogeneity and Water-Energy Balances. Vadose Zone Journal, 9: 970-983. DOI: 10.2136/vzj2010.0014.

McNamara JP, Chandler D, Seyfried M, Achet S. 2005. Soil moisture states, lateral flow, and streamflow generation in a semi-arid, snowmelt-driven catchment. Hydrological Processes, 19: 4023-4038. DOI: 10.1002/hyp.5869.

McNamara JP, Tetzlaff D, Bishop K, Soulsby C, Seyfried M, Peters NE, Aulenbach BT, Hooper R. 2011. Storage as a Metric of Catchment Comparison. Hydrological Processes: n/a-n/a. DOI: 10.1002/hyp.8113.

Miller CR, Routh PS, Brosten TR, McNamara JP. 2008. Application of time-lapse ERT imaging to watershed characterization. Geophysics, 73: G7-G17. DOI: 10.1190/1.2907156.

Murray CD, Buttle JM. 2005. Infiltration and soil water mixing on forested and harvested slopes during spring snowmelt, Turkey Lakes Watershed, central Ontario. Journal of Hydrology, 306: 1-20. DOI: 10.1016/j.jhydrol.2004.08.032.

Nolan BT, Healy RW, Taber PE, Perkins K, Hitt KJ, Wolock DM. 2007. Factors influencing ground-water recharge in the eastern United States. Journal of Hydrology, 332: 187-205. DOI: 10.1016/j.jhydrol.2006.06.029.

Nolin AW, Daly C. 2006. Mapping "at risk" snow in the Pacific Northwest. Journal of Hydrometeorology, 7: 1164-1171. DOI: 10.1175/jhm543.1.

Papalexiou SM, Koutsoyiannis D, Montanari A. 2011. Can a simple stochastic model generate rich patterns of rainfall events? Journal of Hydrology, 411: 279-289. DOI: 10.1016/j.jhydrol.2011.10.008.

Priestley CHB, Taylor RJ. 1972. On the Assessment of Surface Heat Flux and Evaporation Using Large-Scale Parameters. Monthly Weather Review, 100: 81-92. DOI: 10.1175/1520-0493(1972)100<0081:otaosh>2.3.co;2.

Ragab R, Finch J, Harding R. 1997. Estimation of groundwater recharge to chalk and sandstone aquifers using simple soil models. Journal of Hydrology, 190: 19-41. DOI: 10.1016/s0022-1694(96)03067-3.

Rose CW. 1984. Modeling evapotranspiration - an approach to heterogeneous communities. Agricultural Water Management, 8: 203-221. DOI: 10.1016/0378-3774(84)90054-4.

Sammis TW, Evans DD, Warrick AW. 1982. COMPARISON OF METHODS TO ESTIMATE DEEP-PERCOLATION RATES. Water Resources Bulletin, 18: 465-470.

Saxton KE, Rawls WJ, Romberger JS, Papendick RI. 1986. Estimating generalized soil-water characteristics from texture. Soil Science Society of America Journal, 50: 1031-1036. DOI: 10.2136/sssaj1986.03615995005000040039x.

Scanlon BR, Healy RW, Cook PG. 2002. Choosing appropriate techniques for quantifying groundwater recharge. Hydrogeology Journal, 10: 18-39. DOI: 10.1007/210040-00101762-2.

Scanlon BR, Keese KE, Flint AL, Flint LE, Gaye CB, Edmunds WM, Simmers I. 2006. Global synthesis of groundwater recharge in semiarid and arid regions. Hydrological Processes, 20: 3335-3370. DOI: 10.1002/hyp.6335.

Selle B, Minasny B, Bethune M, Thayalakumaran T, Chandra S. 2011. Applicability of Richards' equation models to predict deep percolation under surface irrigation. Geoderma, 160: 569-578. DOI: 10.1016/j.geoderma.2010.11.005.

Seyfried MS. 2003. Incorporation of remote sensing data in an upscaled soil water model. In: Scaling Methods in Soil Physics, Pachepsky Y. Radcliffe D. E. SHS (ed.) CRC Press, pp: 309-346.

Seyfried MS, Grant LE, Marks D, Winstral A, McNamara J. 2009. Simulated soil water storage effects on streamflow generation in a mountainous snowmelt environment, Idaho, USA. Hydrological Processes, 23: 858-873. DOI: 10.1002/hyp.7211.

Seyfried MS, Schwinning S, Walvoord MA, Pockman WT, Newman BD, Jackson RB, Phillips EM. 2005. Ecohydrological control of deep drainage in arid and semiarid regions. Ecology, 86: 277-287. DOI: 10.1890/03-0568.

Seyfried MS, Wilcox BP. 2006. Soil water storage and rooting depth: key factors controlling recharge on rangelands. Hydrological Processes, **20**: 3261-3275. DOI: 10.1002/hyp.6331.

Shallcross, A.T., 2012. LiDAR Investigations of snow distribution in mountainous terrain, Boise State University, Boise, ID, 62 pp. URL: http://scholarworks.boisestate.edu/td/349/.

Sheffer NA, Cohen M, Morin E, Grodek T, Gimburg A, Magal E, Gvirtzman H, Nied M, Isele D, Frumkin A. 2011. Integrated cave drip monitoring for epikarst recharge estimation in a dry Mediterranean area, Sif Cave, Israel. Hydrological Processes, 25: 2837-2845. DOI: 10.1002/hyp.8046.

Shuttleworth WJ. 1992. Evaporation. In: Handbook of Hydrology, Maidment DR (ed.) McGraw-Hill, Inc., pp: 4.1-4.53.

Simmers I. 1997. Groundwater recharge principles, problems and developments. In: Recharge of Phreatic Aquifers in (Semi) Arid Areas, Simmers I (ed.) A.A. Balkema, pp: 1-18.

Smith TJ, McNamara JP, Flores AN, Gribb MM, Aishlin PS, Benner SG. 2011. Small soil storage capacity limits benefit of winter snowpack to upland vegetation. Hydrological Processes, 25: 3858-3865. DOI: 10.1002/hyp.8340.

Sorensen JPR, Finch JW, Ireson AM, Jackson CR. 2013. Comparison of varied complexity models simulating recharge at the field scale. Hydrological Processes: n/a-n/a. DOI: 10.1002/hyp.9752.

Spence C. 2007. On the relation between dynamic storage and runoff: A discussion on thresholds, efficiency, and function. Water Resources Research, 43. DOI: W12416 10.1029/2006wr005645.

Spence C, Guan XJ, Phillips R, Hedstrom N, Granger R, Reid B. 2010. Storage dynamics and streamflow in a catchment with a variable contributing area. Hydrological Processes, 24: 2209-2221. DOI: 10.1002/hyp.7492.

Spence LE. 1937. Root Studies of Important Range Plants of the Boise River Watershed. Journal of Forestry, 35: 747-754.

Steinwand AL, Harrington RF, Or D. 2006. Water balance for Great Basin phreatophytes derived from eddy covariance, soil water, and water table measurements. Journal of Hydrology, 329: 595-605. DOI: 10.1016/j.jhydrol.2006.03.013.

Stratton BT, Sridhar V, Gribb MM, McNamara JP, Narasimhan B. 2009. Modeling the Spatially Varying Water Balance Processes in a Semiarid Mountainous Watershed of Idaho1. Journal of the American Water Resources Association, 45: 1390-1408. DOI: 10.1111/j.1752-1688.2009.00371.x.

Sutanudjaja EH, van Beek LPH, de Jong SM, van Geer FC, Bierkens MFP. 2011. Large-scale groundwater modeling using global datasets: a test case for the Rhine-Meuse basin. Hydrology and Earth System Sciences, 15: 2913-2935. DOI: 10.5194/hess-15-2913-2011.

Taucer PI, Munster CL, Wilcox BP, Owens MK, Mohanty BP. 2008. Large-scale rainfall simulation experiments on juniper rangelands. Transactions of the ASABE, 51: 1951-1961.

Tesfa TK, Tarboton DG, Chandler DG, McNamara JP. 2009. Modeling soil depth from topographic and land cover attributes. Water Resources Research, 45. DOI: W10438 10.1029/2008wr007474.

Teuling AJ, Lehner I, Kirchner JW, Seneviratne SI. 2010. Catchments as simple dynamical systems: Experience from a Swiss prealpine catchment. Water Resources Research, 46. DOI: W10502 10.1029/2009wr008777.

Thoma MJ, McNamara JP, Gribb MM, Benner SG. 2011. Seasonal recharge components in an urban/agricultural mountain front aquifer system using noble gas thermometry. Journal of Hydrology, 409: 118-127. DOI: 10.1016/j.jhydrol.2011.08.003.

Tromp-van Meerveld HJ, Peters NE, McDonnell JJ. 2007. Effect of bedrock permeability on subsurface stormflow and the water balance of a trenched hillslope at the Panola Mountain Research Watershed, Georgia, USA. Hydrological Processes, 21: 750-769. DOI: 10.1002/hyp.6265.

Van Der Lee J, Gehrels JC. 1997. Modelling of groundwater recharge for a fractured dolomite aquifer under semi-arid conditions. In: Simmers, Ian, A.A. Balkema, pp: 129-144.

Wang L, Wei SP, Horton R, Shao MA. 2011. Effects of vegetation and slope aspect on water budget in the hill and gully region of the Loess Plateau of China. Catena, 87: 90-100. DOI: 10.1016/j.catena.2011.05.010.

Williams CJ, McNamara JP, Chandler DG. 2009. Controls on the temporal and spatial variability of soil moisture in a mountainous landscape: the signature of snow and complex terrain. Hydrology and Earth System Sciences, 13: 1325-1336. DOI: 10.5194/hess-13-1325-2009.

Willmott CJ, Rowe CM, Mintz Y. 1985. Climatology of the terrestrial seasonal water cycle. Journal of Climatology, 5: 589-606. DOI: 10.1002/joc.3370050602.

Wilson JL, Guan H. 2004. Mountain-Block Hydrology and Mountain-Front Recharge. In: Groundwater Recharge in a Desert Environment: The Southwestern United States, Hogan JF, Phillips FM, Scanlon BR (eds.) American Geophysical Union, pp: 113-137.

Winstral A, Marks D, Gurney R. 2013. Simulating wind-affected snow accumulations at catchment to basin scales. Advances in Water Resources, 55: 64-79. DOI: 10.1016/j.advwatres.2012.08.011.

Wood WW. 1999. Use and misuse of the chloride-mass balance method in estimating ground water recharge. Ground Water, 37: 2-3. DOI: 10.1111/j.1745-6584.1999.tb00949.x.

Yenko, M. (2003), Hydrometric and Geochemical Evidence of Streamflow Sources in the Upper Dry Creek Experimental Watershed, Southwestern Idaho, M.S. thesis, 116 pp., Dep. of Geosci., Boise State University, http://earth.boisestate.edu/drycreek/publications/.

Zanardo S, Basu NB, Botter G, Rinaldo A, Rao PSC. 2012. Dominant controls on pesticide transport from tile to catchment scale: Lessons from a minimalist model. Water Resources Research, 48: 17. DOI: 10.1029/2010wr010088.

Zhang L, Potter N, Hickel K, Zhang YQ, Shao QX. 2008. Water balance modeling over variable time scales based on the Budyko framework - Model development and testing. Journal of Hydrology, 360: 117-131. DOI: 10.1016/j.jhydrol.2008.07.021.